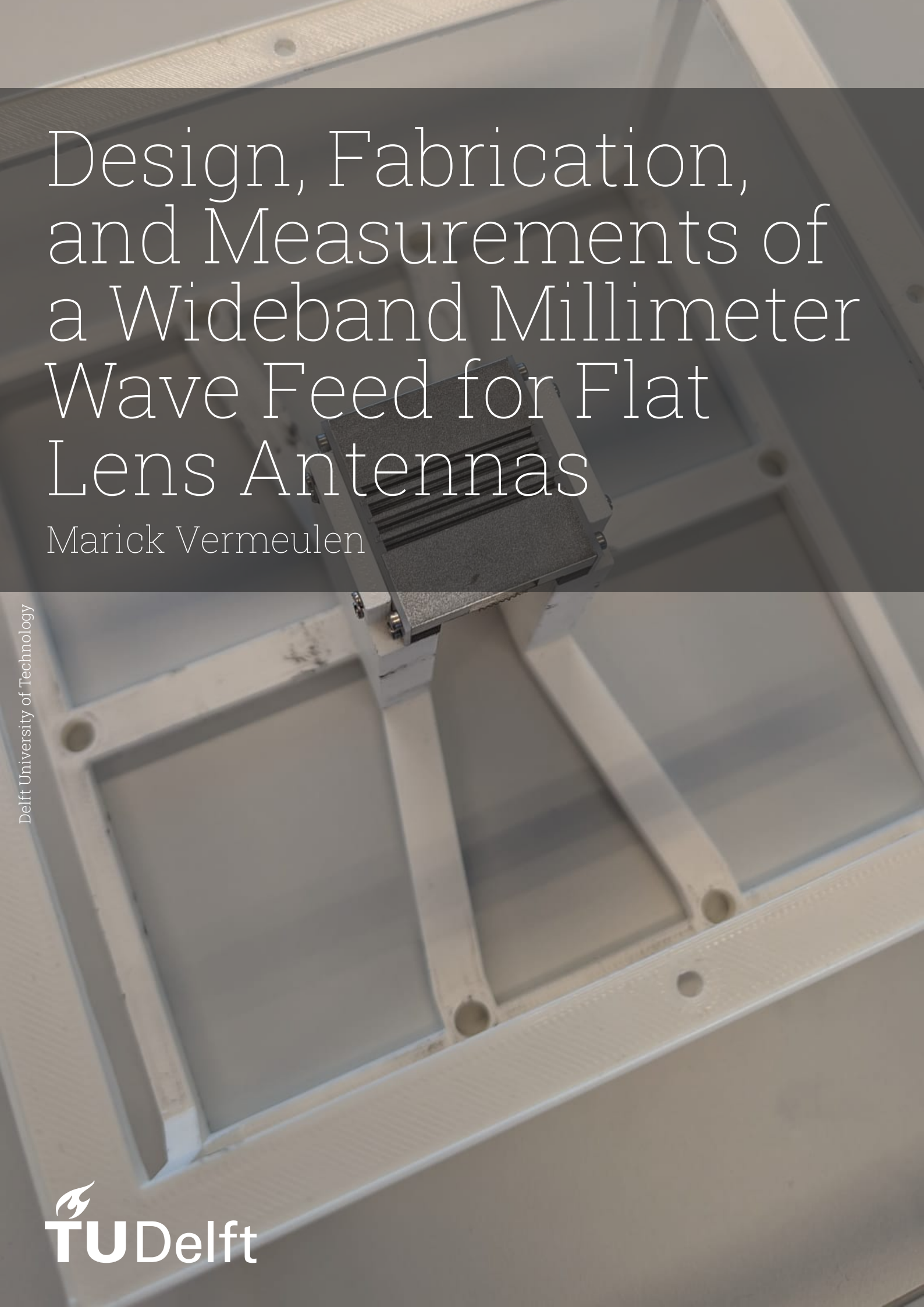

Design, Fabrication, and Measurements of a Wideband Millimeter Wave Feed for Flat Lens Antennas

Marick Vermeulen

Delft University of Technology

TU Delft

Design, Fabrication, and Measurements of a Wideband mm-Wave Feed for Flat Lens Antennas

by

Marick Vermeulen

Supervised by: dr. Daniele Cavallo
Caspar Coco Martin

to obtain the degree of
Master of Science
at the Delft University of Technology,
to be defended publicly on
Wednesday October 1, 2025 at 4:15 PM

Student number: 5003652
Project duration: September 2, 2024 October 1, 2025

Thesis Committee:

dr. Daniele Cavallo	(Chair)
Prof. dr. Andrea Neto	(Member)
Prof. dr. O. Yarovyi	(Member)

TU Delft

Abstract

Recent advances in millimeter-wave (mmWave) and terahertz (THz) technology for high-speed wireless communication and high-resolution radars have increased the popularity of lens antennas due to their large gain and multi-beam capability. Wideband flat lenses offer a practical alternative to bulky curved dielectric lenses at millimeter-wave (mmWave) frequencies, thanks to their low profile and compatibility with planar fabrication.

A key challenge in implementing quasi-optical systems with wideband flat lens antennas is the design of a suitable feed. The feed should provide efficient illumination of the lens in the large bandwidth of operation to maximize aperture efficiency. Furthermore, the feed should be suitable for integration with the electronics at millimeter waves. Existing wideband lens of reflector feeds are based on conical horn with corrugated or optimized profiles, small elliptical lenses, and near-field focusing arrays. However, horns and small lenses do not reach high aperture efficiency over a band exceeding an octave, while near-field focusing arrays are characterized by high losses due to the feeding network.

In this work, different compact feeding solutions for wideband flat lenses are proposed and investigated. A comparative analysis between a connected array and a continuous transverse stub array implementation shows that the continuous transverse stub offers the best performance.

The design of a dedicated feeding network for the continuous transverse stub array is then presented. This consists of two feeding microstrips, a tapered power combiner, and a transition to a coaxial connector. The fabrication of the assembly components for the continuous transverse stub array is discussed, along with the printed circuit board (PCB) implementation of the feeding network. Through-Reflect-Line (TRL) calibration structures are used to de-embed the coaxial-to-microstrip transition.

Finally, the feed is measured in combination with a previously developed flat lens prototype. The experimental results confirm the wideband properties of the feed, which can operate across the entire bandwidth from 30 to 60 GHz.

Acknowledgements

I would like to take this opportunity to thank the many people who helped me during this thesis. I would like to start by thanking Daniele for always being thorough with design implementations and text. I really appreciated the amount of feedback and guidance I received throughout this thesis. Furthermore, your passion for this project and your dedication to research and supervising others was truly inspiring to me, and I would like to thank you for that as well.

Additionally, I would like to thank my daily supervisor, Caspar, for helping me with questions about concepts, coding, fabrication details, providing feedback on my writing, showing me how to perform measurements, and demonstrating how complicated projects can be tackled efficiently.

On a more practical note, I would like to thank Leon from Dienst Elektronische en Mechanische Ontwikkeling for fabricating the continuous transverse stub feed, and Juan for all the assistance in examining fabricated components under the microscope.

Beyond acknowledgements related to this project, I would like to thank the other professors of the Terahertz Sensing group for providing us with, in my opinion, quite unique knowledge on antenna analysis methods that can be used for design. Additionally, it was a pleasure to be part of this group over the past year, from laughing at the coffee corner to organizing a delightful Christmas dinner in collaboration with Tom and Pieter.

I would also like to thank my two close friends and colleagues during the masters program, Marti and Tom. Your friendship has been invaluable during this period, and it made doing the thesis with the group even more enjoyable.

I would also like to thank my other friends in Delft and The Hague. Spending time with you brought me joy, inspiration, and balance, which kept me energized to work on my thesis over the past year.

Last but certainly not least, I would like to thank my family. First of all, for all their unconditional love, and, on a more scientific note, my mom and dad for providing me with an upbringing that valued learning while also giving me the space to explore my own interests, make mistakes, and learn from them. I would also like to thank my brother and sister for the many passionate discussions about their work and mine; these conversations were a great inspiration. Even though there will be a large distance between us, I am certain that their support and love will always remain.

Contents

List of Figures

List of Tables

List of Acronyms

ADL Artificial Dielectric Layer. iii, 12, 13, 17

CNC Computer Numerical Control. 42, 45
CTS continuous transverse stub. iii–vi, 5–7, 15, 17–20, 22–27, 31–36, 38, 42–44, 46–48, 57, 58

EBG Electromagnetic Band Gap. 46, 48

FW Full-wave. 7, 22

GCPW Grounded Coplanar Waveguide. iii, v, 22, 27–31, 33, 35, 40–43, 45
GRIN gradient index. iii, v, 7, 17–20, 31, 48, 49

mmWave millimeter-wave. 13, 14, 48, 49
MoM Method of Moments. 14

PCB Printed Circuit Board. iv, vi, 6, 19, 22, 33–36, 38, 39, 41–43, 45–47, 57
PPW parallel plate waveguide. 15, 21–23, 31, 57, 58
PTFE Polytetrafluoroethylene. iv, 32–34, 36, 37

QO quasi-optical. iv–vi, 5–7, 22, 32, 33, 38, 44–48
QPT Quadratic Phase Taper. iii, 11–13

RAM Random Access Memory. 18

TRL Trough Reflect Line. iv, 6, 33–36, 38–41, 46

1

Introduction and Project Background

The main objective of this thesis project is to design, manufacture and test an antenna feed for efficient illumination of a wideband planar artificial dielectric lens. The target frequency band is 30 to 60 GHz, which is of interest for wideband millimeter-wave (mmWave) applications, such as high-speed data transmission and high-resolution radars. This chapter introduces the topic and the motivation for the study and describes the context of the project in relation to earlier work carried out at the Terahertz sensing group.

1.1 Introduction

Dielectric lenses are widely used quasi-optical components in imaging and antenna systems. For decades, they have been applied in fields such as radio astronomy, radar, and satellite communications. Lens antennas offer high-gain radiation properties and can enable beam scanning through lateral feed displacement. In addition, multiple beams can be generated simultaneously in a lens antenna system by positioning several feeds in the focal plane. With recent advances in mmWave and terahertz (THz) technologies for high-speed wireless communication and high-resolution radar, dielectric lenses have gained increased popularity for multibeam, directive antennas [1], [2].

Conventional homogeneous dielectric lenses offer good performance, but are often bulky and electrically thick. In contrast, flat lenses are low-profile and easier to fabricate than curved lenses, making them particularly attractive at mmWave frequencies. Planar thin lens antennas can be implemented using Fresnel lenses [3], transmitarrays [4], or metasurfaces [5]. However, a key drawback of these solutions is their limited frequency bandwidth. This limitation arises from phase wrapping along the aperture, leading to abrupt, discontinuous shifts in the phase distribution. Additionally, for designs based on periodic structures, the bandwidth is often constrained by the resonant characteristics of the unit cell.

To address bandwidth constraints, true-time-delay (TTD) lenses can be utilized, which avoid the issue of phase wrapping. One such example is a gradient index (GRIN) lens consisting of a dielectric cylinder with a refractive index that varies radially. Although this design achieves a broad bandwidth, it comes at the expense of an increased lens thickness [6]. A potential strategy to minimize the thickness of wideband TTD lenses involves using materials with high permittivity [7]. However, to mitigate the reflection losses introduced by the high permittivity, matching layers are necessary to enhance transmission at the airlens boundary [8]. To achieve high-permittivity materials with refractive indices significantly higher than those of conventional dielectrics, artificial dielectric layers (ADLs) can be used [9]. These consist of cascaded periodic arrays made up of subwavelength patches (capacitive gratings) that enhance the effective refractive index by introducing greater phase delay for plane waves propagating through the artificial medium. TTD lens designs that use such periodic subwavelength structures have been demonstrated in [10] and [11].

In this thesis, we consider a specific flat lens design presented in [12], operating from 30 to 60 GHz, with a focal ratio of 0.67 and a diameter of six wavelengths at the highest frequency of operation. Based on

this design, a prototype was manufactured and tested with an open-ended waveguide feed [13]. However, the waveguide feed introduces high spillover losses. In addition, two different feeds covering separate frequency bands were used to collectively cover the large operational bandwidth. The objective of this project is to design a more suitable antenna feed for such a lens with improved performance. This feed should provide efficient illumination of the lens over the large bandwidth of operation at millimeter waves, to maximize aperture efficiency.

Before describing the feed design for the fabricated dielectric lens, it is essential to provide a comprehensive overview of the lens itself, which constitutes the background for this project. We assume that the wideband feed designed here will be used in combination with the existing lens design from [12].

1.2 Flat GRIN Lenses

In general, a lens antenna can be used to focus electromagnetic waves. This can be done by employing either a specific geometric shape or by altering the refractive index across the structure. Lenses in which the refractive index changes over the aperture are typically called gradient-index (GRIN) lenses. This work will primarily focus on flat lenses where the relative permittivity varies across the structure to obtain the desired phase profile.

Furthermore, GRIN lenses can be split into true time-delay lenses and Fresnel zone lenses. True time-delay lenses have wideband properties but are typically electrically thick. Fresnel zone lenses employ phase wrapping to reduce the maximum phase shift required, at the cost of reduced bandwidth. A good trade-off between bandwidth and efficiency was achieved in [12], by realizing TTD with high effective permittivity within the core of the lens. The high permittivity is achieved by means of artificial dielectric layers (ADLs) that are periodic arrays of sub-wavelength patches embedded in a dielectric medium.

1.2.1 Prior Work at the THz Sensing Group

The flat lens design in [12] was obtained with the approach described in Figure 1.1a. The idea is to consider the highest possible effective permittivity realizable with the chosen manufacturing technology for the core of the lens, to minimize the thickness. The maximum effective permittivity depends on the smallest track and gap width and the minimum dielectric thickness realizable in a given printed circuit board technology, and on the frequency, since the ADL period must be smaller than $\lambda/4$ to reduce dispersion.

For a multilayer PCB made of ROGERS 4003 and for the 30-60 GHz frequency band, the highest effective permittivity is around 22, thus this value is considered for the core at the center of the lens. Each unit cell of the lens also includes two matching layers above and below the core to implement wideband matching to free space.

The high refractive index of the lens core can be achieved using ADLs [14]. Thus, the practical realization of the lens unit cells is based on the stackup shown in Figure 1.1b, where the high permittivity core is made of ADLs with larger patches, the first matching layers are obtained with ADLs with smaller patches, and the outer matching layers (with effective relative permittivity of 2) consist of perforated dielectrics.

A prototype based on this design was realized and tested in [13]. The photo of the lens is illustrated in Figure 1.2, together with some measured radiation patterns at two frequencies. The lens was designed to work from 30 to 60 GHz, has a diameter of 30mm and the $F/D = 0.67$. This corresponds to a theoretical maximum directivity of 20 dBi at 30 GHz and 26 dBi at 60 GHz. However, the aperture efficiency of this lens was limited by the spillover losses of the adopted feed. Hence, the scope of this work is to identify and design a more suitable feed for the lens prototype.

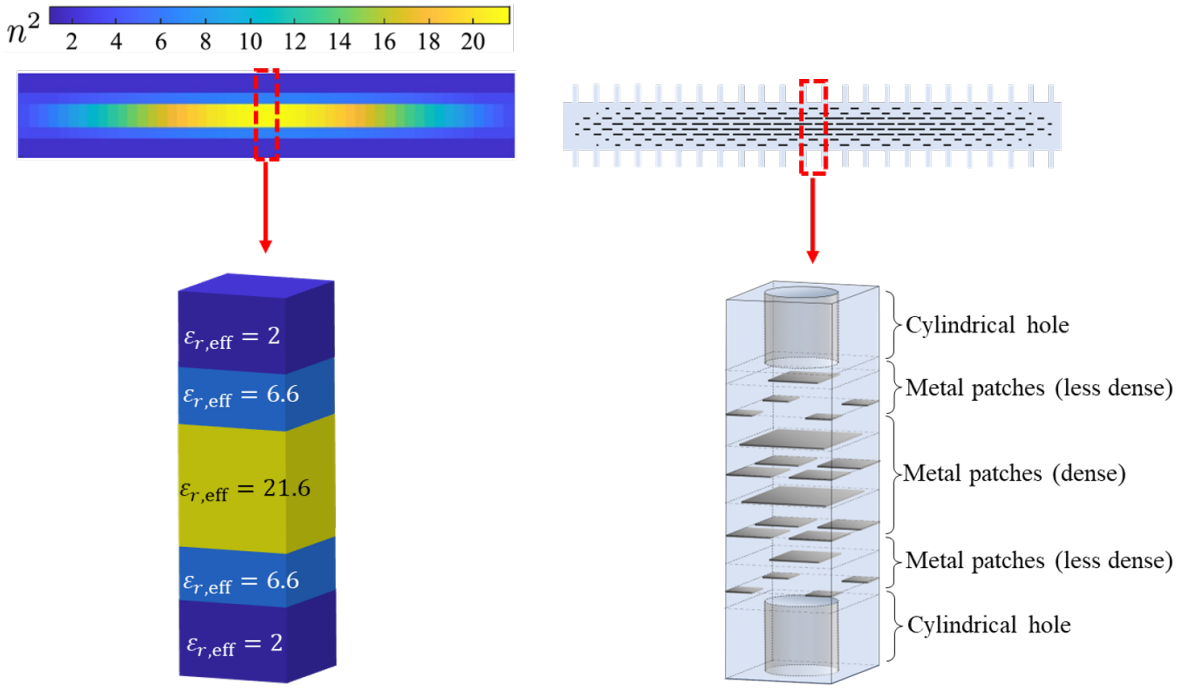

(a) Effective permittivity profile of the unit cell.

(b) Semi-detailed stack-up in terms of ADLs.

Figure 1.1: Implementation of the unit cell in the design.

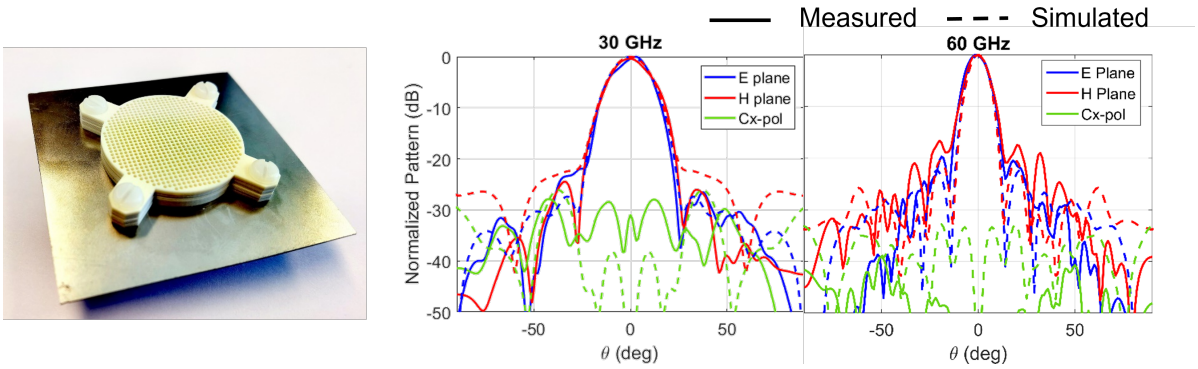

Figure 1.2: GRIN lens prototype and some measured patterns.

1.2.2 Measured Performance

To test the lens design, a simple feed is considered in [12], consisting of an open-ended waveguide. Two standard waveguides are used for different sub-bands: a WR28 waveguide with cross section 7.11 Œ 3.56 (mm^2), which operates in the 26.540-GHz band, and a WR-15 waveguide with cross section 3.76 Œ 1.88 (mm^2), which operates in the 5075-GHz band.
The simulated efficiency of the lens with the open-ended waveguide feeds, split in different contributions [15], is reported in Fig. 1.4a, for the 3040, 40-50, and 5060-GHz bands. It can be noted that the main cause of losses is the spillover, due to the wide radiation patterns of the feed, as illustrated in Figure 1.3. Similar losses were also observed in the measured results in Figure 1.4b, where the gain is about 5 dB lower than directivity, largely due to spillover.

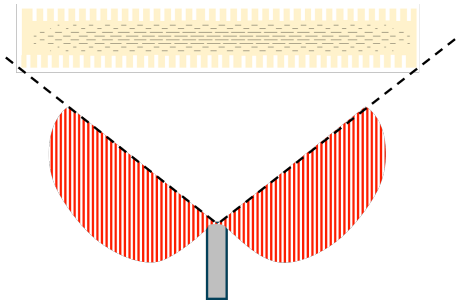

Figure 1.3: WG feed with wide beam and high spillover losses.

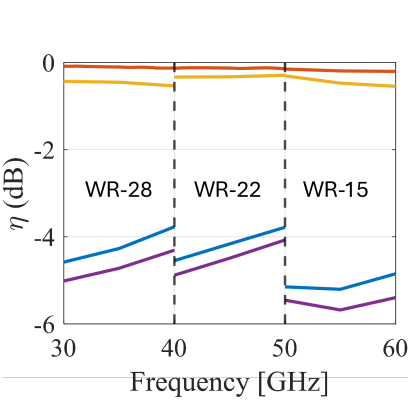

(a) Simulated efficiency of the lens with the described WG feeds

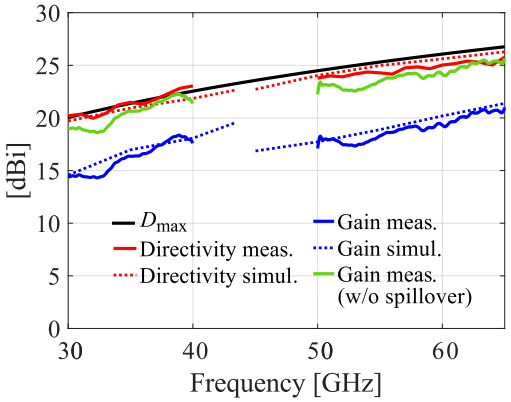

(b) Measured and simulated directivity and gain

Figure 1.4: Performance of the lens with the open-ended waveguide feed.

1.3 State of the Art Wideband Lens Feeds

An ideal wideband lens feed consists on an antenna that illuminates the lens efficiently through non-dispersive frequency-independent radiation patterns. Possible solutions to realize wideband reflector or lens feeds include conical (corrugated or profiled) horn antennas [16], [17] (see Fig. 1.5a). The main complication with this solution is the fact that although horns that achieve good illumination over a 2:1 bandwidth have been realized at microwave frequencies, they are not readily available at mmWave frequencies. Moreover, commercial mmWave horns are not optimized for frequency-independent patterns.

Another possible solution for wideband lens feeds is an array with quadratic phase excitation [18] (see Fig. 1.5b). Such a phase distribution creates a field distribution that is focused in the near-field, which results in a radiation pattern more stable with frequency in the far-field. The reflector feed presented in [18] was shown to operate in a 2:1 bandwidth; however, due to the large size of this array, the improved reflector illumination efficiency comes at the cost of losses inside the feeding network.

Other wideband feeds based on small lenses could be used, such as the hyper-hemispherical lens fed by a connected array introduced in [19], which achieved stable patterns for a 3:1 band (see Fig. 1.5c). Potential complications with such designs can be high-reflection losses at the lens interface with air, since this concept requires high-permittivity material for the lens. In addition, a feeding network is still needed, causing additional losses.

Another solution consists of the hemispherical lens fed by a corrugated waveguide feed proposed in [20], as shown in Fig.1.5d. This concept achieves low losses but can operate over a 50% bandwidth, which is narrower than the target bandwidth, exceeding one octave.

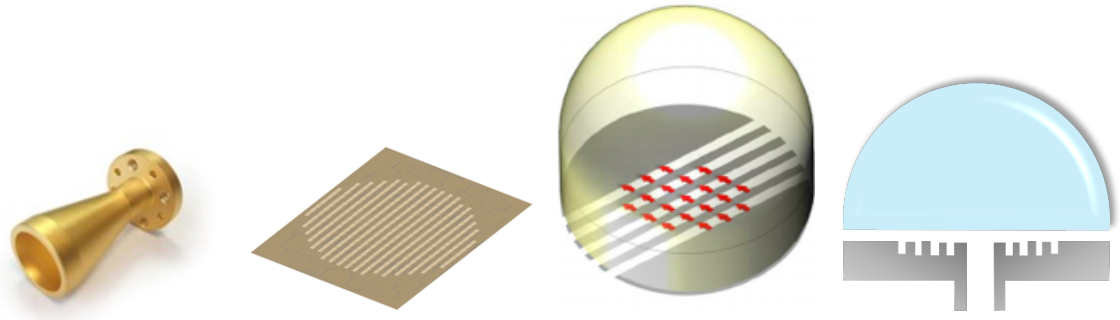

(a) Horn antenna

(b) Near-field focused connected array

(c) Connected-array-fed hyper-hemispherical lens

(d) Hemispherical-lens-fed corrugated waveguide

Figure 1.5: State of the art lens feeds.

1.4 Preliminary Investigation on Horn and 4×4 Connected Array

From the measured performance with waveguide feeds, it can be seen that, although the taper efficiency is high, the aperture efficiency is relatively low due to the very wide primary patterns. Therefore, the performance of the system can be improved with a better feed design. This feed is supposed to have most of its power intercepted by the lens and have frequency independent patterns in the band 30-60 GHz. While the design of an optimized feed were not the focus of the work done in [12], a basic study of different feeds was carried out. Two feeds were considered: a conical horn (see Fig. 1.6a) and a 4 by 4 connected slot array (see Fig. 1.6b). The array is excited with an amplitude taper and a quadratic phase distribution, in order to realize low-dispersive radiation pattern from 30 to 60 GHz. The simulated efficiency resulting from these feeds can be found in figure 1.7 and, since the connected array in general showed a higher and more stable aperture efficiency, this concept is selected for further investigation during this project.

(a) Circular horn

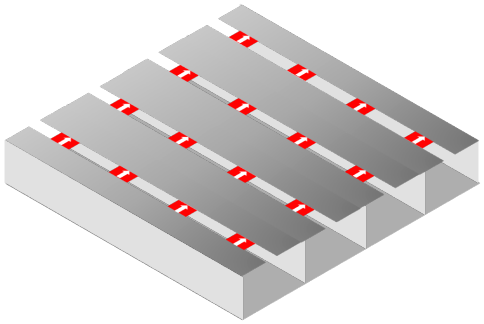

(b) 4 by 4 connected array

Figure 1.6: Alternative feed concepts.

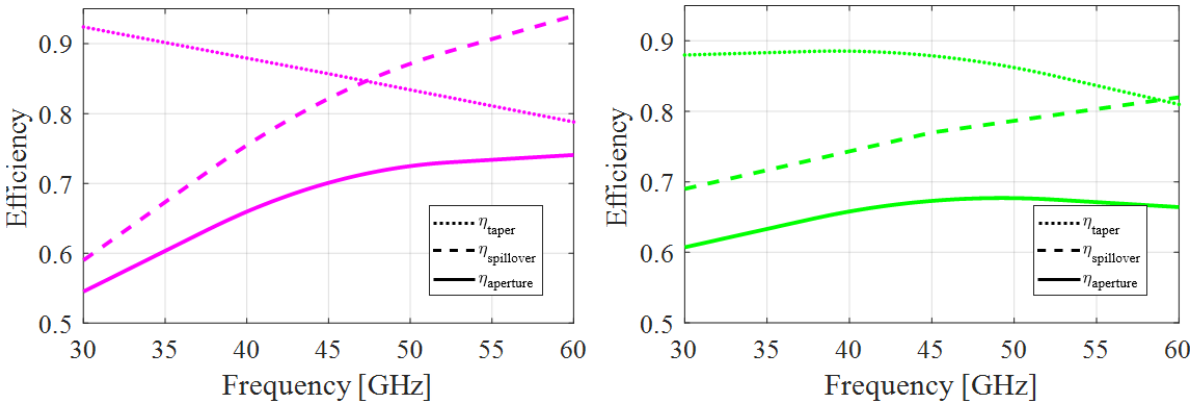

Figure 1.7: Simulated efficiency for the feeds in Figure 1.6. Left: circular horn, right: 4×4 connected array.

Several possible designs are proposed, based on connected arrays with hybrid dielectric / metal superstrates and continuous transverse stub (CTSs) arrays. The concept that seems to achieve the best performance is a full-metal parallel plate waveguide array. The design is analyzed in terms of the total efficiency of the quasi-optical (QO) system and is manufactured and tested for experimental validation.

1.5 Thesis Outline

This work consists of the following chapters:

- In Chapter 2, a number of possible designs are proposed, based on connected arrays with hybrid dielectric/metal superstrates and CTS arrays. The concept that appears to achieve the best performance is a CTS waveguide array. The design is analyzed in terms of the total efficiency of the QO system.
- In Chapter 3, the design of a compact, efficient, and simple feeding structure is presented. Furthermore, the feeding design is validated, a calibration procedure is applied to de-embed the effects of the coaxial connector, and the entire QO system is again analyzed in terms of total efficiency.

- Chapter 4 provides a detailed explanation of the fabrication process for all previously developed components: the CTS feed, a PCB panel with a through-reflect-line (TRL) calibration structure and feeding PCBs, as well as the design and fabrication of a holder for the entire QO system.
- In Chapter 5, the measurement setups and results for the TRL calibration, the feed, and the entire QO system are reported and discussed.
- Chapter 6 provides concluding remarks on the measurements of the designed feed and the performance of the QO system. In addition, a discussion of important future developments and possible improvements is presented.

2

Analysis and Design of the Feed

2.1 Proposed Approach

Existing wideband feeds for lenses or reflectors are based on conical horns with corrugated or optimized profiles, small elliptical lenses, and near-field focusing arrays. However, horns and small lenses do not reach high aperture efficiency over a band exceeding an octave, while near-field focusing arrays are characterized by high losses due to the presence of feeding networks. In this project, we investigate the use of a small wideband array as a lens feed. The array is excited with an amplitude taper and a quadratic phase distribution. This concept can potentially result in a good trade-off between frequency bandwidth and efficiency.

A number of possible designs are proposed, based on connected arrays with hybrid dielectric / metal superstrates and continuous transverse stub (CTS) arrays. The concept that seems to achieve the best performance is a full-metal CTS array. This array is fed by a low-loss parallel plate waveguide feeding network. The design is analyzed in terms of total efficiency of the quasi-optical (QO) system.

2.1.1 Structure of This Chapter

This chapter is structured as follows:

- Section 2.2 contains a discussion of design trade-offs and considerations. A finite 4×4 connected array is analyzed in terms of matching efficiency and radiation patterns. An amplitude taper and quadratic phase profile are proposed as methods to reduce the frequency dependence of the radiation patterns. A hybrid superstrate made of a dielectric slab and a capacitive grid is also investigated to improve the impedance matching of the array.
- In Section 2.3, two detailed designs are proposed. The first is a single-polarized 4×4 connected array loaded with a superstrate and backed by a reflector. The slots are terminated with open circuits to improve the impedance matching of the edge elements. The second design is based on parallel plate waveguides with a corporate feeding network, similar to the CTS concept in [21], [22]. The corporate feeding network implements the desired amplitude and phase distribution at the array aperture.
- Section 2.4 describes the performance of the proposed feed together with the flat lens. Full-wave (FW) simulations with CST Microwave Studio are performed to assess the total efficiency of the feed/lens system. To speed up the computation time of the electrically large lens, the patches of the artificial dielectrics are replaced by a homogenized gradient index (GRIN) permittivity, which allows for faster simulations.
- In Section 2.5 the FW simulations are used to make a performance comparison between the two designs in terms of their overall efficiency of the entire QO system.
- In Section 2.6 conclusive remarks are provided and an outlook for the next chapter is presented.

2.2 Design Trade-off

This section presents a discussion on design trade-offs and considerations. A finite 4×4 connected array is analyzed in terms of matching efficiency, spillover efficiency and radiation patterns. To minimize the frequency dependence of the radiation patterns, an amplitude taper and quadratic phase profile are proposed. Additionally, a hybrid superstrate composed of a dielectric slab and a capacitive grid is explored to enhance the impedance matching of the array.

The method of analysis from [23] is used to evaluate the active input impedance and radiation patterns of the finite connected-array feed. It allows efficient modeling of the finiteness effects of connected slot arrays in a stratified medium. In Appendix A, some remarks on implementation strategies and a summary of the model are given.

2.2.1 Feed Pattern

The existing lens for which a feed is designed, has an F/D ratio of 0.67 [13]. It is clear that the subtended angle of the lens is

$$\theta_{sub} = \tan^{-1}\left(\frac{D}{2F}\right) = 37^{\circ}.$$

If the feed pattern is 0 for $\theta > 37^{\circ}$, the spillover efficiency would be 100%. However, the amplitude taper efficiency is typically low in such cases. If the feed pattern is constant, i.e. an isotropic radiator, the amplitude taper efficiency is 100%. This comes at the cost of the spillover efficiency. Since the aperture efficiency is composed of the product of the taper- and spillover efficiency, there is a clear trade-off between the two.

For parabolic reflectors, it is well established that the optimal pattern requires an edge taper of -11 dB to achieve the highest possible aperture efficiency [24] (see Fig. 2.1). Therefore, if we assume a similar trade-off applies for the flat lens, ideally the desired taper should be -11 dB over the entire band. However, because of the frequency dispersion, a more realistic requirement would be an edge taper that varies as little as possible around -11 dB within the frequency band of operation.

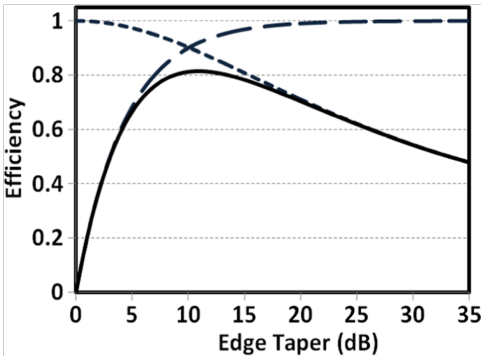

Figure 2.1: The spillover (dashed line), taper (dotted line), and aperture (solid line) efficiency for a space wave far field pattern [24].

2.2.2 Array Size

The array should preferably consist of a power-of-two number of elements to keep the feeding network simple. In addition, to determine the array size, the following considerations apply:

- The feed should be smaller than the lens to justify the need for the lens to increase the total gain.
- It is convenient for the design to ensure that the lens is in the far field of the feed since near-field coupling effects are difficult to model.
- To avoid guided waves, an element spacing at of $0.45\lambda_{@60GHz}$ must be used.
- A trade-off between mismatch and Ohmic losses should also be taken into account: while small arrays suffer more from edge effects, which cause mismatch at the edge elements, larger arrays are characterized by higher losses in the feeding network.

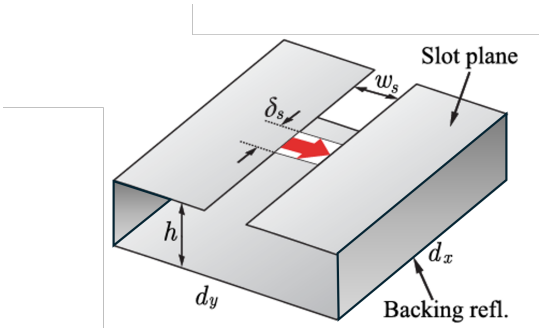

Figure 2.2: Geometry of the unit cell.

Based on these considerations, a 4 × 4 array appears to be a suitable choice for the size of the feed.

2.2.3 Array Unit Cell Concept

The geometry under consideration is shown in Fig. 2.2. It consists of a slot that is connected to the adjacent unit cells. To realize unidirectional radiation, a backing reflector is used. Furthermore, vertical metal walls are inserted to ensure that guided waves do not propagate inside the substrate. The array period is set at $d_x = d_y = 0.45\lambda_{@60GHz} = 2.25$ (mm). The height of the backing reflector ($h = 0.36$(mm)) is chosen to optimize the impedance matching and illumination quality. The slot feeding is modeled with an ideal delta gap generator. The length of the feed and width of the slots are chosen to optimize the impedance matching for the final design ($\delta_s = 0.77$(mm) and $w_s = 0.88$(mm)).

From the proposed unit cell, a finite 4×4 array is implemented. The analysis of the finite array in terms of active impedance and radiation patterns is based on the procedure described in Appendix A, which is a semi-analytical spectral method of moments. This analysis approach allows the efficient computation of the impedance matrix of the array needed for optimizing the geometrical parameters.

2.2.4 Uniform Excitation

We first consider a finite array as shown in Fig. 2.3, where all the elements are excited with the same amplitude and equal phase. The active impedances and radiation pattern for this configuration are shown in Fig. 2.4. Results from our method and CST are presented and shown to be in fair agreement. It can be noted that the patterns exhibit different beamwidth at different frequencies, due to the change of effective area with respect to the wavelength. It is clear that this variation is not suitable to illuminate the lens with a constant subtended angle over the desired octave bandwidth of operation.

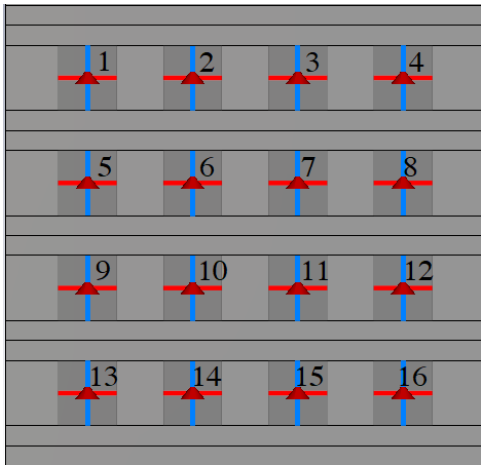

Figure 2.3: Finite array with all ports.

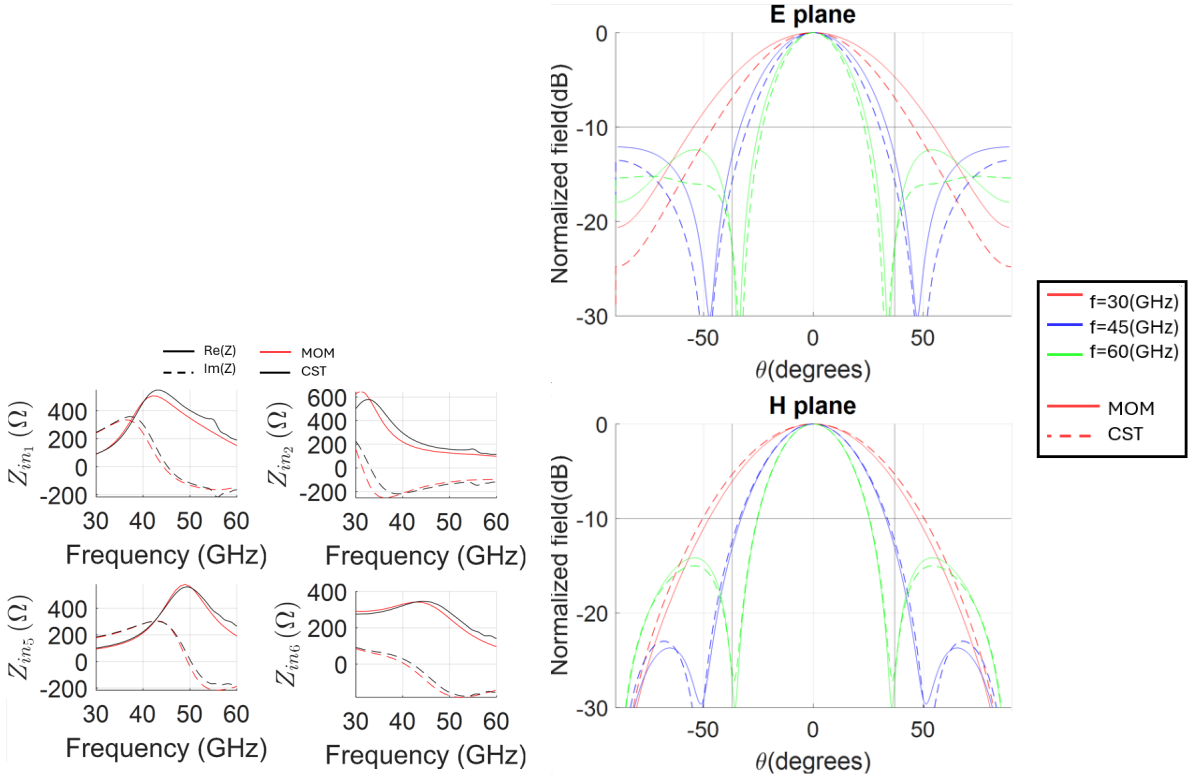

(a) Active impedance for uniform excitation

(b) Radiation patterns for uniform excitation

Figure 2.4: Far-field radiation patterns and active input impedance of 4×4 connected slot array with uniform excitation.

2.2.5 Gaussian Amplitude Taper

Instead of uniformly exciting the elements, one can apply a Gaussian amplitude taper to the array elements, as shown in Table 2.1. This results in the radiation patterns displayed in Fig. 2.5. By comparing the maximum edge taper between these patterns and those obtained with a uniform excitation (shown in Fig. 2.4), it is evident that the Gaussian taper significantly improves taper efficiency at the highest frequency, although at the expense of higher spillover loss at the lowest frequency. Moreover, the variation of beamwidth with frequency remains noticeable.

Elements	Amplitude
1, 4, 13, 16	0.36
2, 3, 5, 8, 9, 12, 14, 15	0.6
6, 7, 10, 11	1

Table 2.1: Amplitude values for different elements.

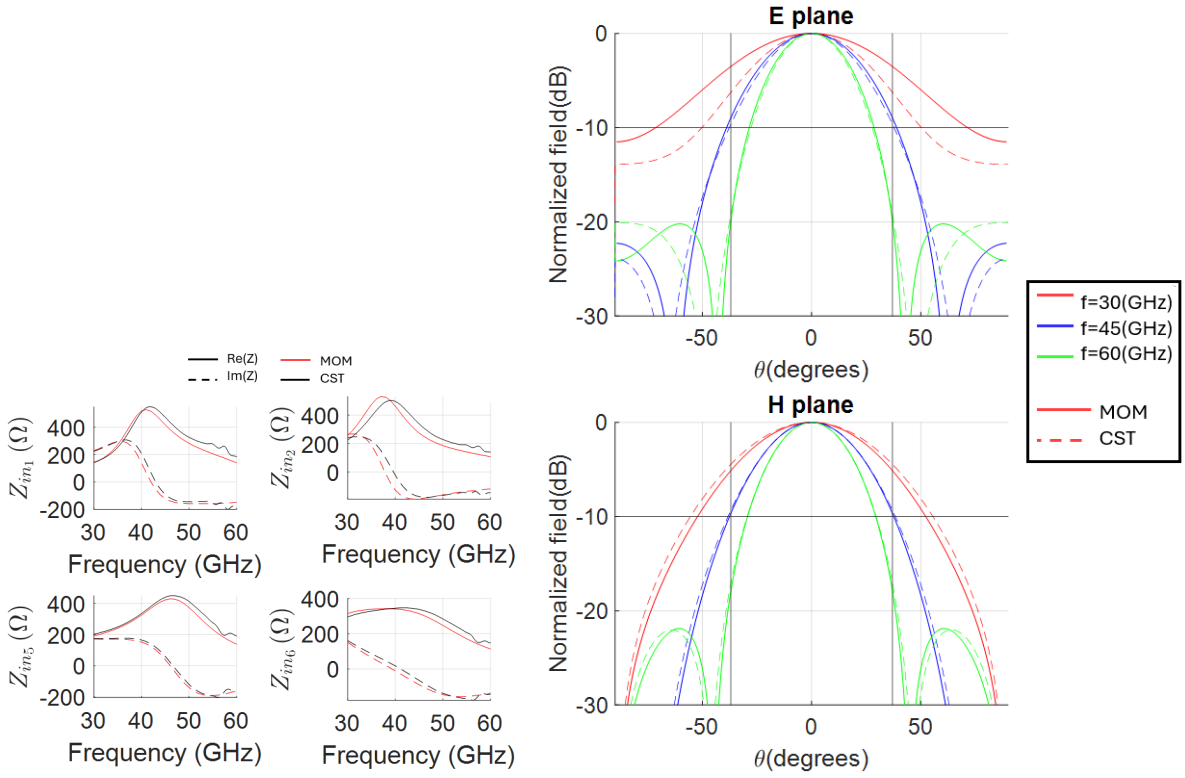

(a) Active impedance for amplitude taper

(b) Radiation patterns for amplitude tapered excitation

Figure 2.5: FF patterns and impedance of amplitude tapered connected array.

2.2.6 Quadratic Phase Taper (QPT)

A quadratic phase taper (QPT) can be applied over the aperture of the array, to create a virtual focus point, at distance F from the array. Fig. 2.6 provides an illustration of this principle. The phase shifts for each element are determined by applying the phase shift described in equation (2.1) for a two-dimensional array. The resulting tapered phase profile can then be obtained by using the outer product, as shown in equation (2.2). It is important to note that, in this work, the virtual focus is placed behind the array, to reduce the size of the quasi-optical system.

$$\boldsymbol{\beta}_{q_{2\times 2}} = k_0 \begin{bmatrix} 0 \\ \sqrt{P_1^2 + F^2} - \sqrt{P_2^2 + F^2} \\ \sqrt{P_1^2 + F^2} - \sqrt{P_2^2 + F^2} \\ 0 \end{bmatrix} \tag{2.1}$$

$$\boldsymbol{\beta}_q = \boldsymbol{\beta}_{q,y}\boldsymbol{\beta}_{q,x}^T = \boldsymbol{\beta}_{q_{2\times 2}}\boldsymbol{\beta}_{q_{2\times 2}}^T \tag{2.2}$$

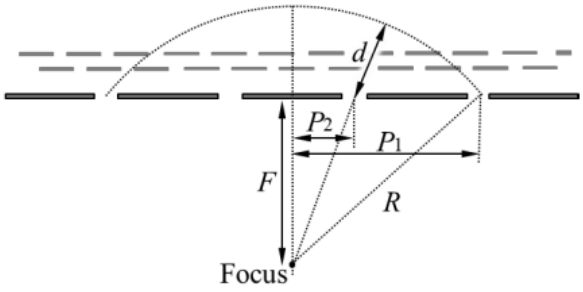

Figure 2.6: Figure to derive the quadratic phase shift

By incorporating the QPT (with a virtual focus point at F=7.75(mm)) into the slot excitations, the dispersion in the radiation patterns is significantly reduced, as demonstrated in Fig. 2.7b. However, a notable drawback of this approach is that some elements have a large phase shift compared to adjacent elements. Therefore, these elements behave as if they were scanning to large angles, which can substantially degrade their matching performance (2.7a). Therefore, while the QPT distribution can be beneficial in improving pattern performance, it should be optimized to balance both pattern enhancement and matching performance.

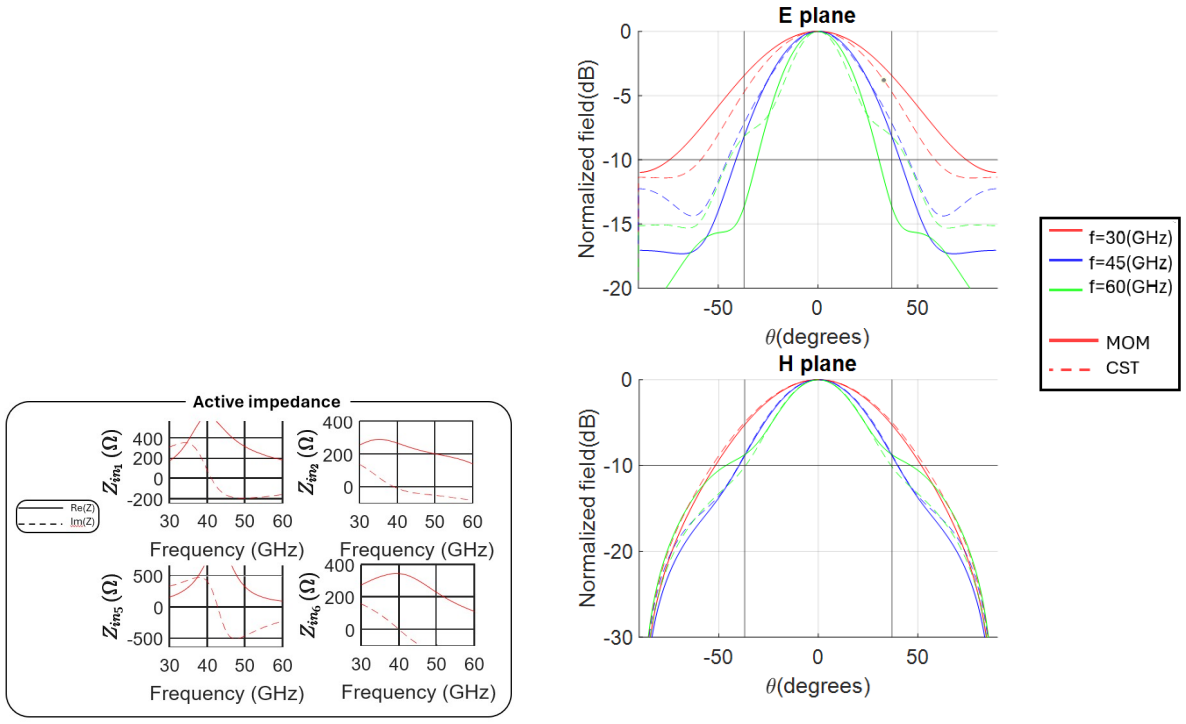

(a) Active impedance for amplitude and quadratic phase tapered excitation

(b) Radiation patterns for amplitude and quadratic phase tapered excitation

Figure 2.7: FF patterns and active impedance for amplitude and quadratic phase tapered connected array.

2.2.7 Adding an ADL and a Dielectric Slab

The unit cell described in Fig. 2.2 does not achieve good impedance matching performance. Adding an ADL and a dielectric slab above the connected array can significantly enhance the matching by acting as an impedance transformer and reducing the effects of the ground plane [25]. To illustrate this concept, an in-house optimizer tool was utilized to design the unit cell in Fig. 2.8a. No finiteness effects are included in this analysis. The geometrical parameters are $d_x = d_y = 2.25$ (mm), $h = 0.36$ (mm), $h_2 = 0.2$ (mm), $h_1 = 0.25$ (mm), $\delta_s = 0.77$ (mm), $w_s = 0.88$ (mm), $\epsilon_{br} = 2.2$, $\epsilon_c = 1.55$, $\epsilon_s = 3.55$. To compensate for the large inductance of the ground plane at low frequency, a series capacitance is assumed to be included in the feed with $C_s = 0.036$(pF). The ADL is characterized by $w = 0.62$ (mm) and $p = 0.505$ (mm), while the period is $d_x/2$.

The corresponding active reflection coefficients for the broad-side and scanning scenarios are presented in Fig. 2.8b. Scanning up to 45° results in a reflection coefficient reaching −10 dB. Consequently, any phase-taper distribution applied to the system must ensure that the virtual focus points do not require any antenna element to scan at angles exceeding $\theta = 45°$.

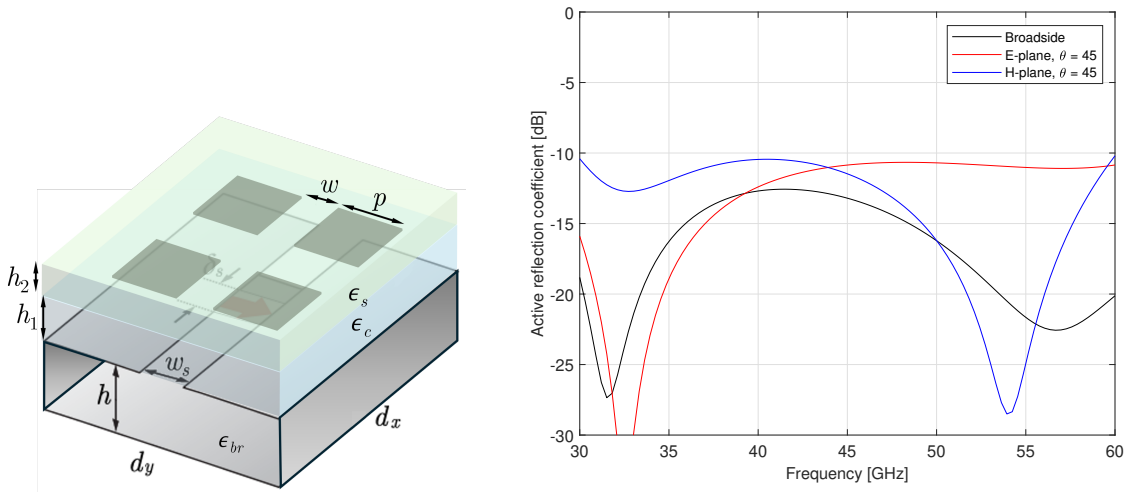

(a) Geometry of the unit cell with ADL superstrate

(b) Active Γ_∞ normalized to $Z_0 = 100(\Omega)$

Figure 2.8: Matching characteristics of infinite CA with ADL and dielectric slab

2.2.8 Conclusion

From this section, it can be concluded that a connected array with a Gaussian amplitude taper, a quadratic phase profile, and an ADL/dielectric loading offers a promising solution for achieving a wideband, efficient, and well-matched configuration. Applying a QPT to the elements of the feeding network can significantly reduce the dispersion in the far-field patterns of the feed. The ADL superstrate can be used to enhance the matching efficiency of the array.

The aperture efficiency on the lower part of the spectrum is limited by the small electrical size of the feed array that causes spillover losses. Moreover, the proposed array requires a feeding network that would be lossy and complex to manufacture at millimeter-wave (mmWave). Therefore, an alternative implementation of the connected array based on parallel plate waveguides will be proposed in the next chapter.

2.3 Proposed Designs

2.3.1 Connected Array

In Fig. 2.9, a finite 4×4 array based on the unit cell in Fig. 2.8a is illustrated. Vertical metallic walls are inserted between slots so that guided waves cannot propagate between the slot and the backing reflector in the direction orthogonal to the slots.

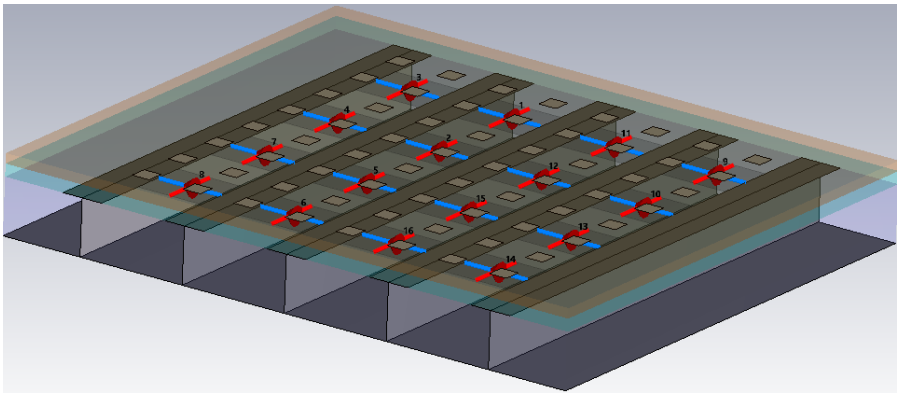

Figure 2.9: 4×4 CA design in CST, based on the unit cell in Fig. 2.8a.

A notable difference between this design and the model used for the Method of Moments (MoM) is the exclusion of the shorts at the slot terminations. In the CST model the slots are terminated with an open circuit instead. This adjustment results in better impedance matching (especially at the lower part of the band, since the metal terminations would nearly short circuit the edge elements at low frequencies).

The radiation patterns in the the E- and H-plane are reported in Fig. 2.10a. Active impedances can be found in Fig. 2.10b. To decrease the reactance of the active impedance, a series capacitor is added to the elements in post-processing. The active reflection coefficients are similar but higher than the one of the unit cell. In addition, the primary patterns can be used to calculate the spillover efficiency of this feed and this is given in Fig. 2.10d.

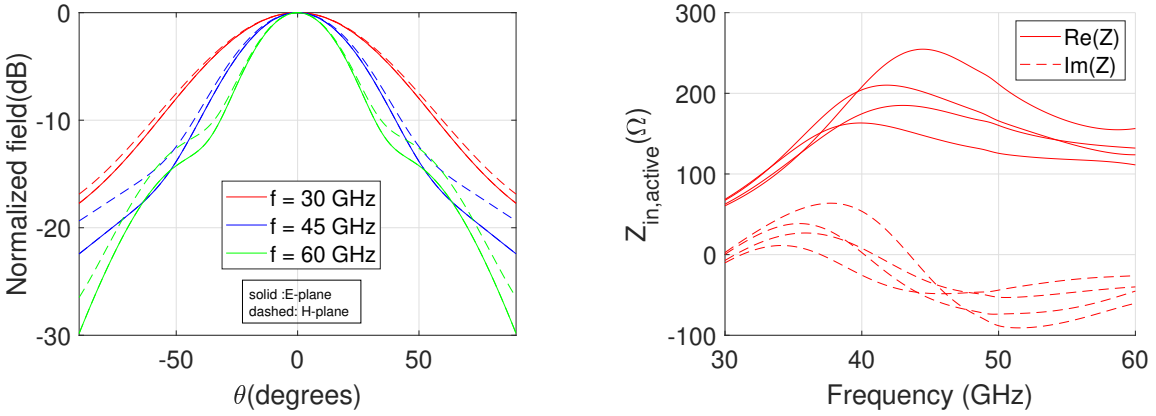

(a) Radiation patterns of the proposed design

(b) Active impedance of the proposed design

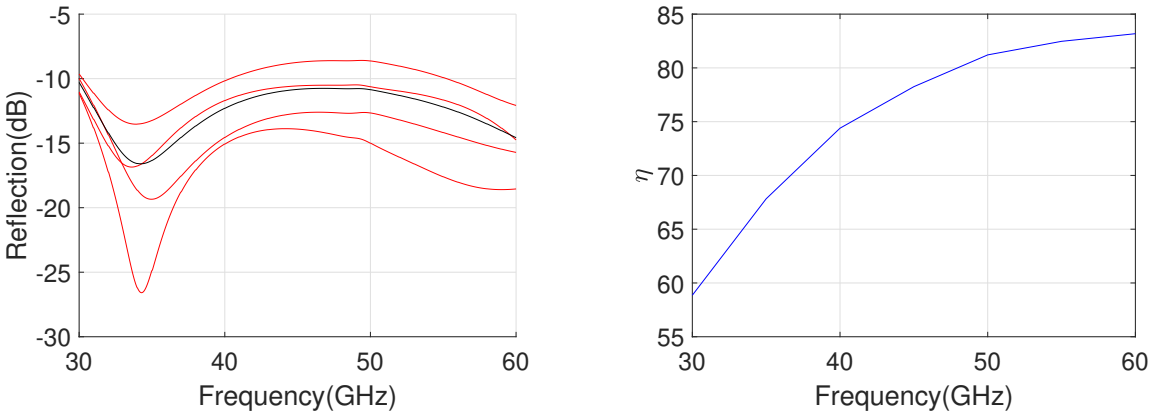

(c) Impedance matching of the proposed design.

(d) Spillover efficiency from the primary pattern

Figure 2.10: Main results from the simulations of the connected array

It can be seen that the spillover efficiency is higher than 60%, but limited at the lowest frequency by the small size of the feed array considered. Solutions to improve the spillover would be to increase the amount of elements, but this would cause increased insertion losses, or to increase the array spacing, which would come at the cost of impedance mismatch due to guided waves propagating along the array.

Moreover, the proposed array requires a feeding network that would be lossy and complex to manufacture at mmWave. Therefore, an alternative implementation of the connected array based on parallel plate waveguides is considered.

2.3.2 Continuous Transverse Stub (CTS)

To implement a low loss distribution network for the array, a CTS [22] feed can be used. It consists of a fully-metal array of parallel plate waveguides (PPWs), with no dielectrics, as shown in Fig. 2.11. A PPW corporate feeding network is designed to implement a quadratic phase taper in one plane, as well as an amplitude taper (see Fig. 2.12). The virtual focus for this plane is located about 5 mm behind the array. By placing the feeding port in the vicinity of this virtual focus, the phase center in the other plane is also at a similar location, thus the feed is illuminating the lens with proper phase in both E- and H-plane. The dimensions are reported in Table 2.2.

The feed network includes multiple impedance transformers for wideband matching, nonequal power splitters to obtain the desired amplitude taper at the aperture, and different length of the PPW sections to obtain the quadratic phase profile.

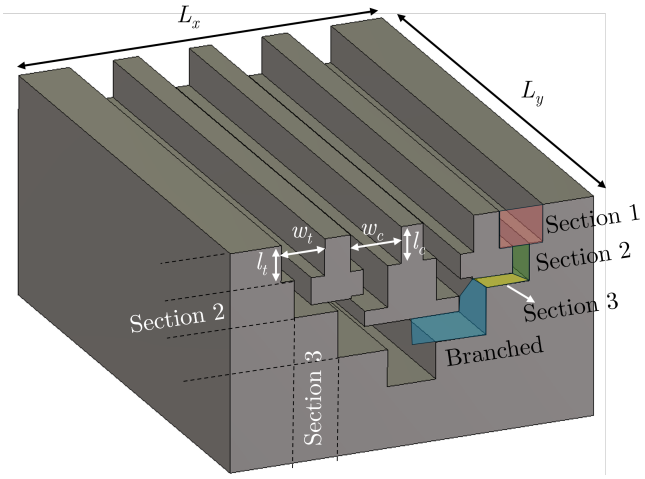

Figure 2.11: 3D view of the CTS design with characteristic parameters.

Fig. 2.13a shows the radiation patterns in both planes at different frequencies. The input impedance is shown in Fig. 2.13b. Since the feed has a large reactive part, a series capacitor is employed to compensate for the high input reactance and to improve the impedance matching. This can also be seen in Fig. 2.17c, where the reflection coefficient is shown to be below -14 dB from 30 to 60 GHz. Some oscillations are present both in the patterns and in the matching. These were observed to be caused by the reflection at the discrete steps of the PPWs. Considering this feed should feed a lens with a subtended angle of 37°, one can compute the spillover efficiency, shown in Fig. 2.13d. The spillover efficiency also oscillates, exhibiting some dips at certain frequencies. Changing the width of the PPW can influence this effect. These parameters can be used to make a tradeoff between performance and compactness of the feed.

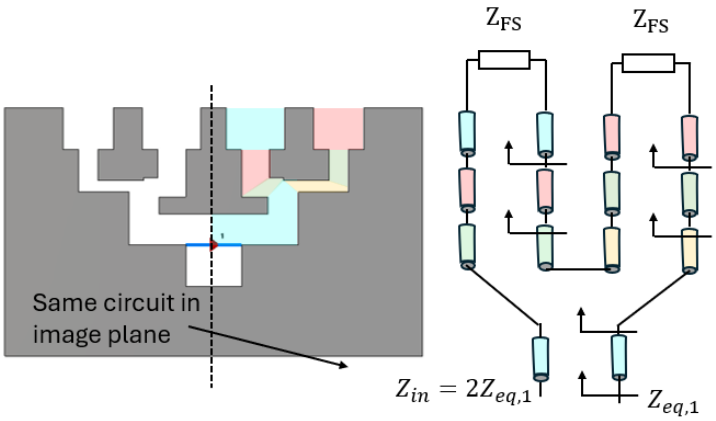

Figure 2.12: CTS design in E plane main sizes are: $L_x = 15(\text{mm})$, $L_y = 20(\text{mm})$, $\delta_{feed} = 2(mm)$ and $w_{feed} = 5(mm)$.

section	width:w_c, w_t(mm)	length:l_c, l_t(mm)
1	2.1, 1.8	1.5
2	1, 0.7	1.35, 1.31
3	0.7, 0.42	0.75, 1.35
branched	1.1	3.95

Table 2.2: Widths and lengths of center and tapered PPW lines.

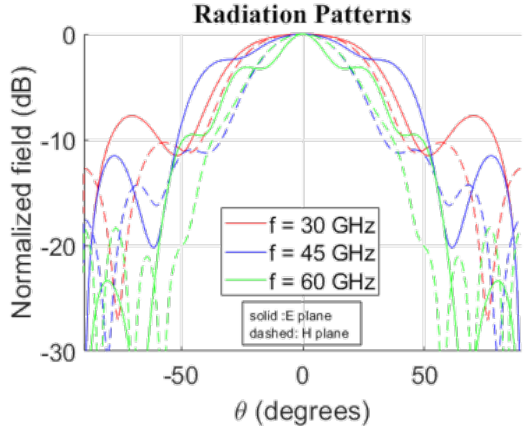

(a) Radiation patterns of the CTS

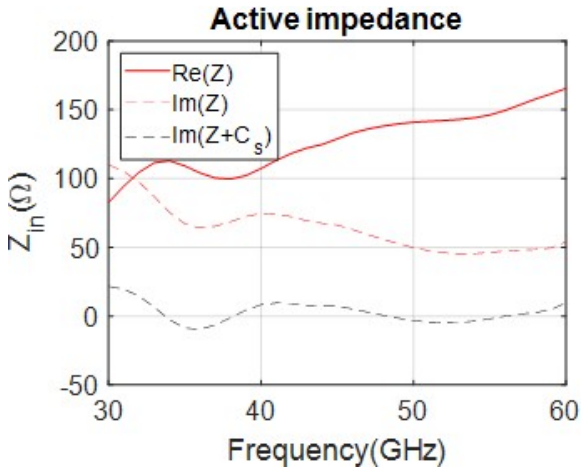

(b) Active impedance with and without a series capacitor

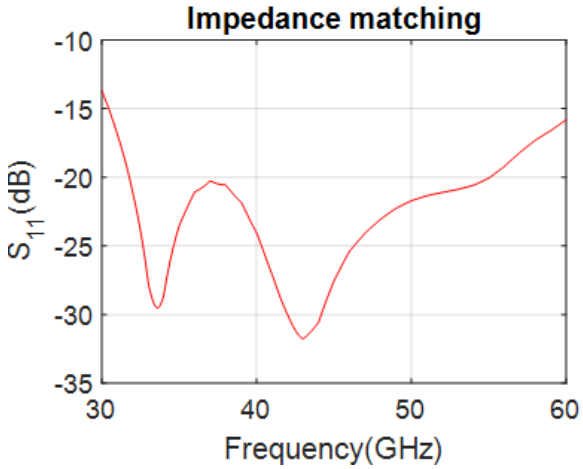

(c) Impedance matching normalized to $Z_0 = 125(\Omega)$ and $C_s = 0.14(\text{pF})$

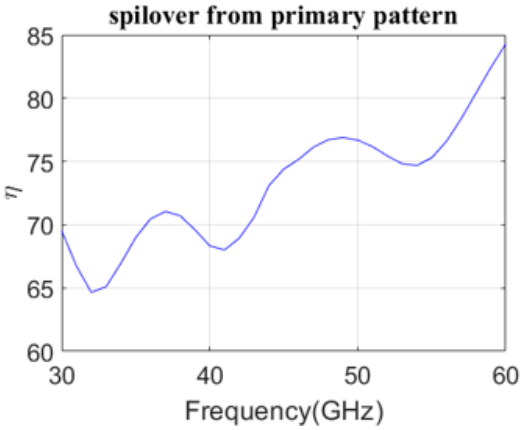

(d) Decreased spillover due to pattern dispersion caused by resonant effects of the finite structure.

Figure 2.13: Main results from the CTS simulations.

2.4 Full-Wave Simulations of the Lens/Feed System

This section focuses on the assessment of the performance of the feed when combined with the flat lens. Full-wave simulation of the entire structure in a solver such as CST can be computationally demanding, especially for the ADL lens, which is composed by a large number of small metal patches, with electrically small gaps between patches. Secondary radiation patterns can be simulated in a more efficient manner by employing an equivalent slab model for the GRIN lens. Moreover a generic view of the simulation setup of the configuration can be seen in figure 2.14

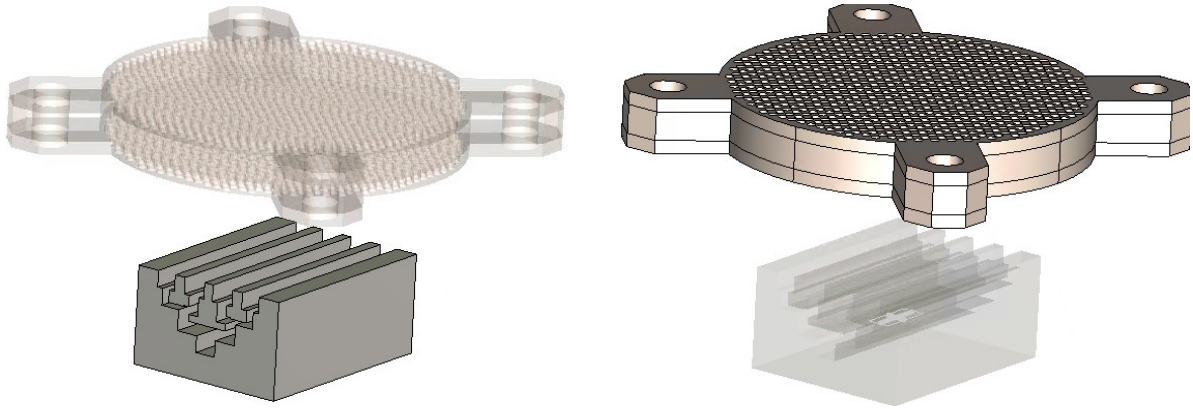

(a) Feed component can be either the CTS or the Connected Array

(b) Lens components can be either equivalent slab model or lens with patches and perforations

Figure 2.14: Simulation setup in CST Studio.

2.4.1 Homogenized GRIN Lens

The simplified model of the GRIN lens assumes that an ADL can be modeled as a slab with effective permittivity ϵ_{eff} that varies radially. Since the effective permittivity is known by design over the entire lens, for the core and matching layers, it can be modeled by equivalent slabs where the permittivity is varied according to a formula. The formula is generated by polynomial fitting of the permittivity profile in each unit cell of the artificial dielectric lens. The resulting distribution is shown in Fig. 2.15a). The radiation patterns in the main planes for the CTS and Connected Array designs are presented in Figures 2.15b and 2.15c, respectively.

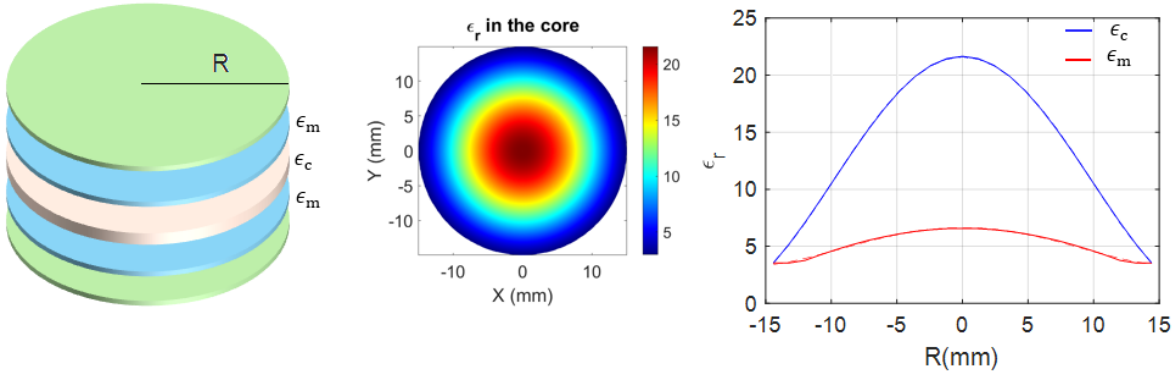

(a) Homogenized GRIN lens with permittivity profiles of the layers.

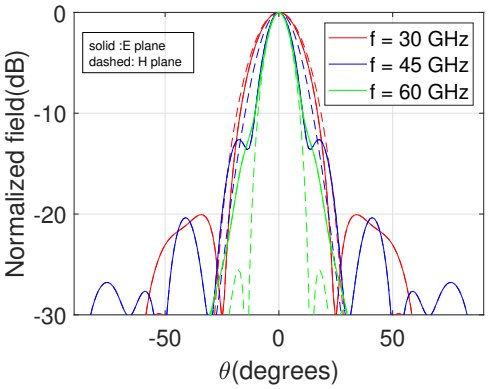

(b) Secondary patterns of the CTS design in both planes

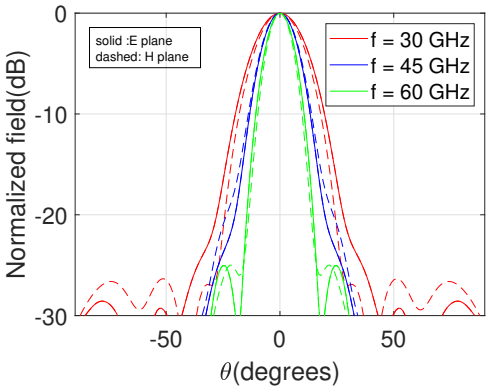

(c) Secondary patterns of the Connected Array design in both planes

Figure 2.15: Secondary patterns in both planes by using analytic formulas for the lens.

2.4.2 Simulations with Patches and Perforations

While the homogenized lens can be used to compare the efficiency of different designs, the final assessment is made by simulating the detailed lens, with patches and perforations. These simulations require large computational resources, but they provide the Ohmic and dielectric losses of the lens.

Such simulations are run on a desktop with 256(GB) Random Access Memory (RAM) and take ca. half a day, while the homogenized lens simulations take ca. half an hour on 18(GB) RAM laptop. An exploded view of the realistic lens model is depicted in Fig. 2.16a. The corresponding radiation patterns can be found in figures 2.16c and 2.16b. The patterns are qualitatively similar in terms of beamwidth to the simplified simulations.

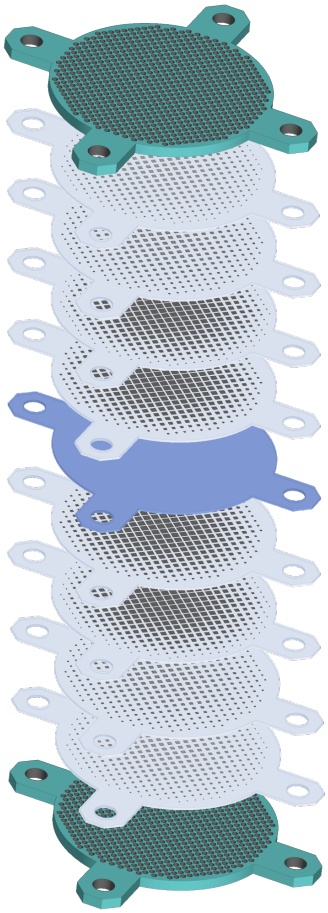

(a) Exploded view of the GRIN lens with patches and perforated dielectrics

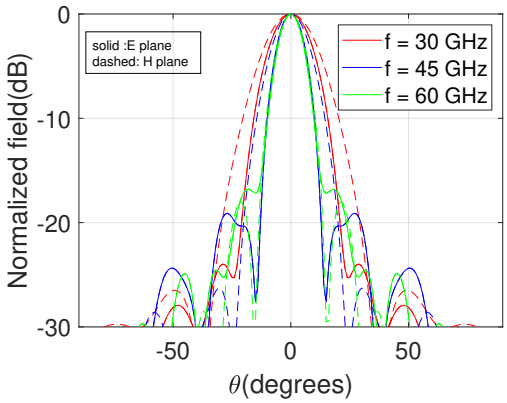

(b) Secondary radiation patterns of the CTS in both planes

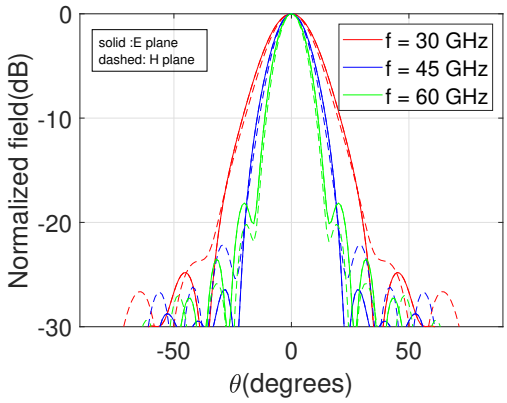

(c) Secondary patterns of the Connected Array in both planes

Figure 2.16: Left: Stackup for the GRIN lens; Right: Secondary patterns in both planes using the GRIN lens with patches and perforations.

2.5 Performance Comparison of the Feed Designs

Based on the simulations including the realistic lens model, with all patches and perforations, one can find the efficiency of the system. All the efficiencies (defined in Appendix B) and main performance characteristics for both designs, are reported in Fig. 2.17. From these figures, it can be observed that the CTS design achieves higher efficiency compared to the Connected Array with a gain varying in the range 18 to 23.5 dBi and total efficiency around 60%, as can be seen in Fig. 2.17(a). This simulated gain is 3 dB higher than previous measurements with an open-ended waveguide as feed [26]. This difference can be attributed to the better spillover efficiency of the proposed CTS feed. Slightly worse results are achieved with the Connected Array design, with the total efficiency reducing to around 40% at the higher frequencies. Compared to the measurements in [26], the Connected Array gives 1.5 dB higher simulated gain than an open-ended waveguide.

Because the fully-metal CTS can be manufactured without the need for complex multi-layer PCBs, and the simulate performance seems better, the CTS feed is selected for this project.

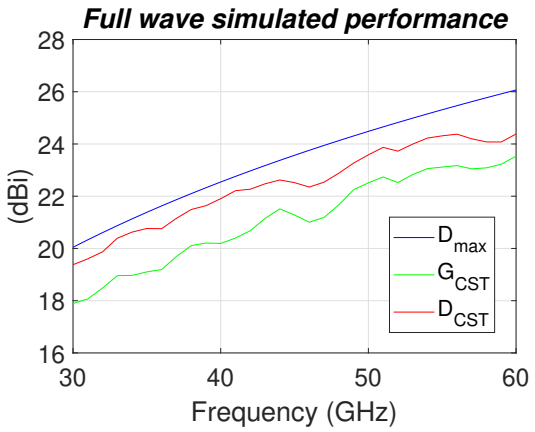

(a) Simulated directivity and gain of the lens with CTS feed.

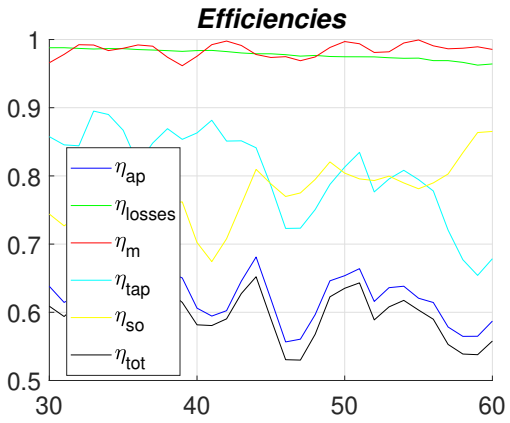

(b) Efficiencies of the lens with CTS feed.

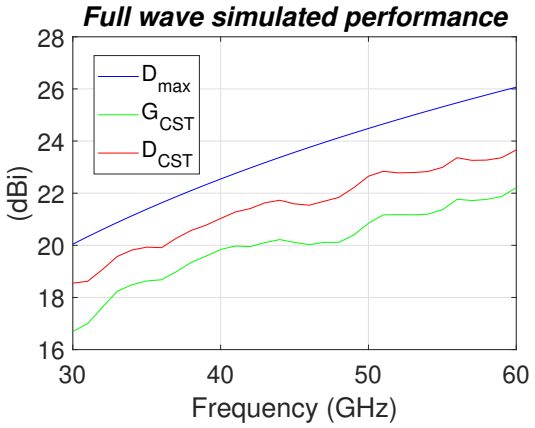

(c) Simulated directivity and gain of the lens with a Connected Array feed.

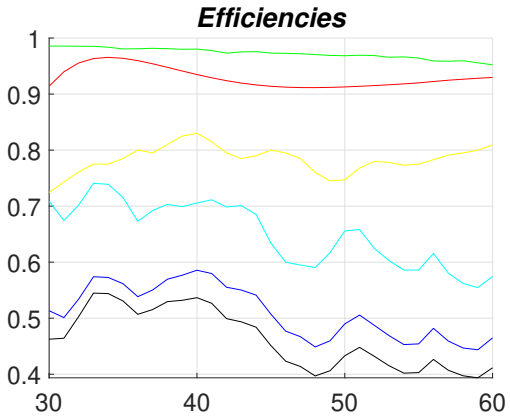

(d) Efficiencies of the lens with a Connected Array feed.

Figure 2.17: Performance comparison of the CTS and the Connected Array design.

2.6 Conclusion and Research Objectives

A feed design for GRIN lenses was presented, with the objective of achieving high aperture efficiency over a wide frequency range. A semi-analytical method for analyzing small connected arrays was employed and used to provide design considerations and trade-offs. The analysis method also allows to calculate the radiation patterns of the feed array, which in turn will illuminate the lens. It was shown that amplitude taper and quadratic phase distribution have beneficial effect in the frequency stability of the patterns.

Among the different possible solutions, we proposed a CTS implementation of the feed, since it exhibits a number of advantages: efficient illumination and good impedance matching over the target octave bandwidth 30-60 GHz. The performance of the proposed design was then evaluated in combination with the flat lens. For enhanced computation speed, time-domain simulations were performed, with a homogenized GRIN material composing the lens. Longer frequency-domain simulations, including the detailed of the lens (patches, dielectric spacers, and perforations), were also done for better estimation of the losses. An enhancement of 3 dB in gain was observed with respect to the open-ended waveguide feeds that were previously used.

Fabricating the CTS feed imposes a number of difficulties related to the transition to a coaxial connector, needed to the measurements. Firstly, there is the need for an impedance transformer that transforms the input impedance from $Z_{\text{in}} = 125\,\Omega$ to $Z_{in} = 50\,\Omega$. Secondly, this impedance transformer should not change the phase center of the feed in both planes, and finally there should be a series capacitance at the feed to compensate for the inductive nature of the input impedance.

During the remaining chapters of the thesis, a possible strategy for integrating the feed with a feeding network will be further investigated: a coaxial or a microstrip line with different sections to implement the impedance transformation or a launcher illuminating an elliptical reflector integrated in the PPW. In addition, the remainder of the thesis will focus on the fabrication and measurement of the design.

3

Implementation of Feeding Network for the CTS Feed

3.1 Introduction

In the previous chapter, a wideband feed for a flat lens was designed. The feed design, a continuous transverse stub (CTS) implementation, provided stable illumination for the lens ($\eta_{so} > 65\%$) and good impedance matching ($S_{11} < -15$[dB]) over an octave of bandwidth.

However, this design did not include a physical implementation of the feeding network for the CTS. In the previous chapter, a floating discrete edge port was used to feed the central parallel plate waveguide (PPW) in the CTS. Additionally, an ideal series lumped element capacitor was used to compensate for the inductance of the CTS. Therefore, this chapter empathizes on the design of a realistic feeding network for the CTS. This chapter is organized in the following way:

- In Section 3.2 a solution is proposed to feed the CTS with an array of two strips printed on a dielectric slab.
- In Section 3.3, a parametric study of the feed parameters is conducted to derive trade-offs and to design a CTS to feeding PCB transition.
- In Section 3.4, a feeding network design for the CTS is presented and the impedance matching of each sub design is validated.
- Section 3.5 focuses on performing FW simulations of the feeding network in combination with the CTS to re-evaluate the performance of the feed in terms of impedance matching and illumination quality. Additionally, the efficiency of the entire quasi-optical (QO) system is quantified.
- Section 3.6 provides concluding remarks and introduces the fabrication strategy for the experimental validation.

3.2 Proposed Feeding Solution

This work proposes a feeding network that consists of a transition from a single conductor on a dielectric substrate to an inhomogeneous stripline connected to a Grounded Coplanar Waveguide (GCPW). The advantages of this design are the fact that the transmission line is wideband and the feeding implementation is compact. Moreover, the GCPW line allows for a transition between the PCB and a coaxial connector.

To maintain the high efficiency of the proposed antenna system, the objective is to make a design with $S_{11} < -15$(dB) and provide efficient illumination of the lens ($\eta_{so} > 60\%$ without compromising the taper efficiency) over the full bandwidth.

3.3 Dependency Between Illumination and Feed Parameters

Consider the feed in Fig. 3.1. This represents a discrete feed port in the center of the CTS. It is defined by the distance between the plates d_{PPW}, the length of the feed δ_f and the width of the feed w_f. One can note that δ_f can be smaller than d_{PPW}, so that the feed is capacitively coupled to the PPW.

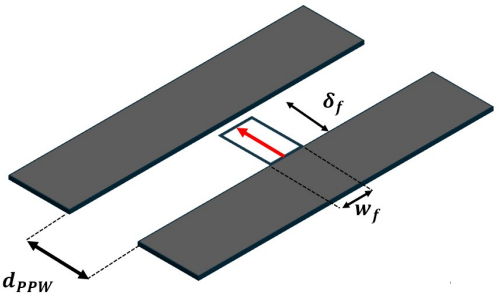

Figure 3.1: Simplistic view of the CTS design with emphasis on the discrete edge port parameters w_f and δ_f.

Depending on the dimensions w_f and δ_f, the illumination properties of the CTS change. The feed length δ_f affect the series capacitance in the feed, but also the symmetry of the excitation of the PPW. Small values of δ_f result in significant asymmetry of the pattern in the E-plane. On the other hand, the width w_f can be adjusted to control the beamwidth in the H-plane. However, a large value of w_f, although improving the illumination of the lens, is difficult to realize in practice, since it would require a taper to the feeding microstrip that is typically small compared to the wavelength.

In Fig. 3.2a, the spillover efficiency of the proposed CTS for different δ_f is shown. For this particular design, the spillover efficiency degrades as δ_f is reduced. The value $\delta_f = 2(\mathrm{mm})$, equal to the PPW plate spacing, is chosen. Figure 3.2b reports a similar sweep, but now for different values of w_f.

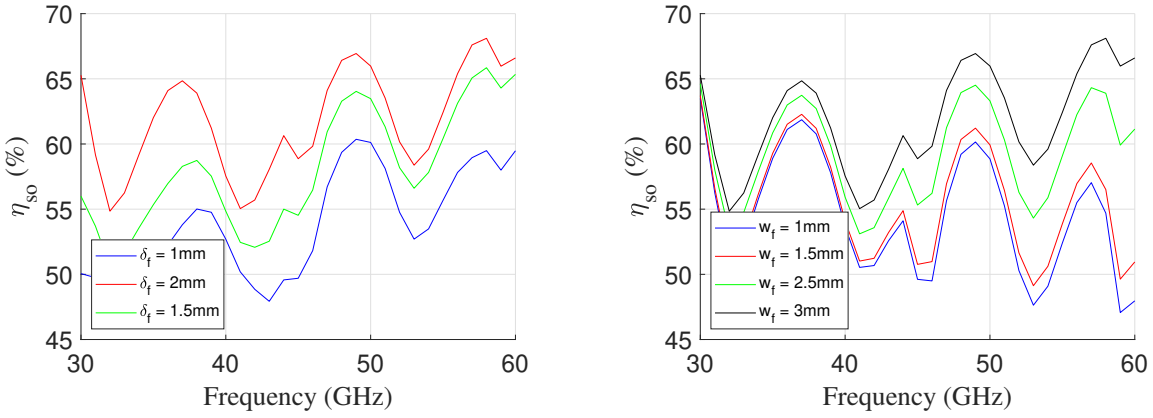

(a) Spillover efficiency over frequency for different δ_f.

(b) Spillover efficiency over frequency for different w_f.

Figure 3.2: Comparison between canonical feed parameters and illumination quality of the feed.

These results suggest a minimum required feed length and width for the port. Meeting this requirement is challenging while also maintaining a well-matched feeding solution, as a wider transition than $\lambda/2$ excites higher-order modes at the discontinuity between the feeding network and the CTS.

Instead of having a single large feed, multiple smaller feeds can be used to keep the well-matched feeding solution and at the same time have the high spillover efficiency. Therefore, a distributed feeding solution as shown in Fig. 3.3a is considered. This configuration consists of two feeds displaced by d, each with dimensions w_f and δ_f.

To choose the distance between the feeds d, a trade-off between illumination quality and impedance matching should be made. One can consider the two feeds as a two-element array. By doing so, it is

evident that the array spacing is large in terms of the wavelength (0.6λ @ 60 GHz) at higher frequencies, resulting in the presence of sidelobes. When d is small, the feed behaves as if it is one large feed. This typically results in a large beamwidth in the H-plane yielding spillover losses. However, if d is too large, high sidelobes occur in the H-plane pattern. As a trade-off, a value of $d = 3$mm is used. Upon defining the effective width $w_{\text{eff}} = 2w_f$, a sweep over w_{eff} can be done. In Fig. 3.3b, the results of this sweep are reported. It shows that a distributed source can achieve excellent illumination quality. Additionally, it is important to mention that there exists an optimum condition that maximizes the spillover efficiency, and it is at an effective width of 3 (mm).

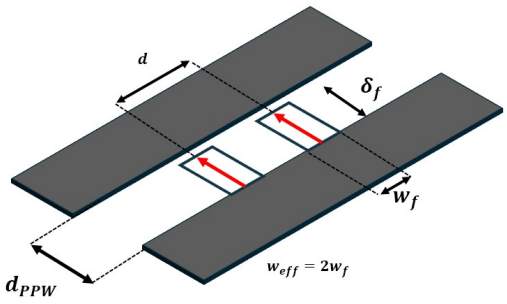

(a) Geometry for the distributed sources CTS feed

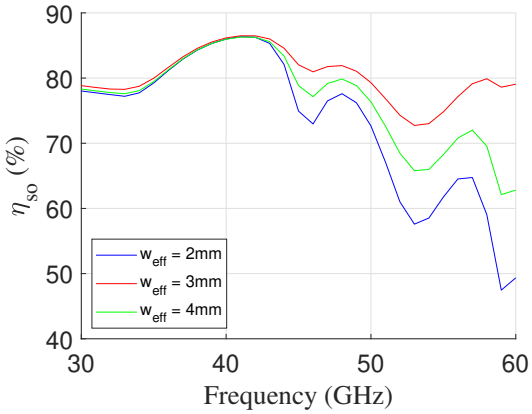

(b) sweep over w_{eff} shows resonant condition for effective width of the feed.

Figure 3.3: Illumination quality can be significantly improved when using a distributed feed.

3.3.1 Designing the CTS to Feeding Network Discontinuity

To implement such a feed in a way that can be realized, there should be an interface to a waveguide opening. In this subsection, a feeding solution for the CTS to distributed feed will be proposed, the feeding parameters related to the impedance matching of the feed will be defined, and these parameters will be optimized to ensure proper matching to a characteristic impedance Z_0. This derivation is performed under the assumption that the reactive part of the discontinuity can be compensated for in the feeding network. Moreover, the defined feed parameters should be based on the distributed source configuration mentioned in Subsection 3.3.

To choose the proper feeding solution, a configuration as close to the discrete edge port simulation is considered. For this design, a single conductor on dielectric was chosen as a suitable feed. This configuration has a dielectric thickness as small as possible ($t_{\text{RO}} = 0.254$(mm), $\epsilon_{r,\text{RO}} = 3.66$). In Fig. 3.4 the geometry of the proposed design is given.

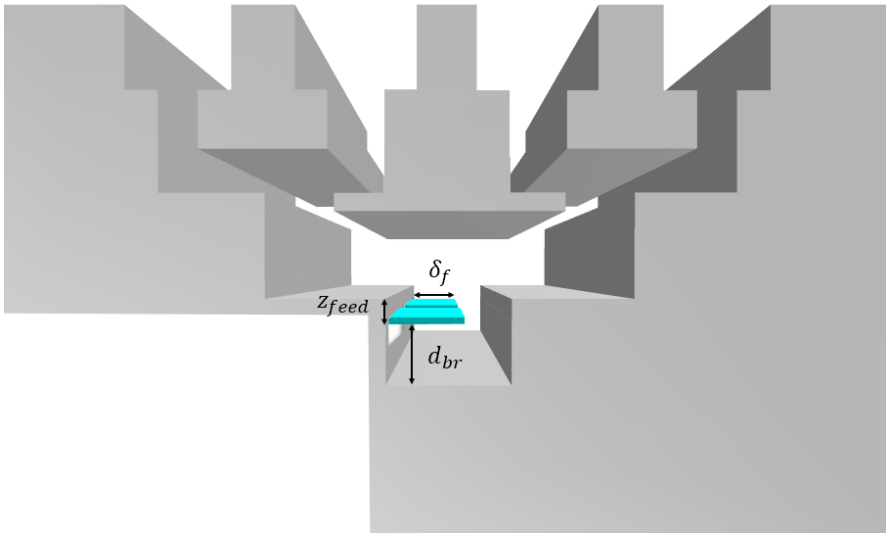

(a) 3D view 1: front view of the CTS to feeding network discontinuity ($\delta_f = 1.35$[mm], $d_{br} = 1.45$[mm], $z_{feed} = 0.6$[mm])

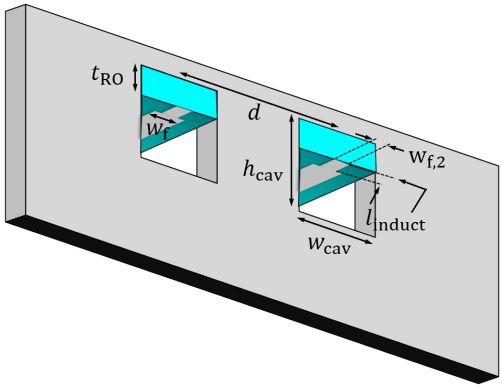

(b) 3D view 2: Detailed view of the cavity and feed parameters to implement the inductor and optimize the impedance matching ($t_{RO} = 0.254$[mm], $l_{\text{induct}} = 0.2$[mm], $w_{cav} = 1.6$[mm], $d = 3$[mm], $h_{cav} = 1$[mm], $w_f = 0.5$[mm], $w_{f,2} = 0.15$[mm])

Figure 3.4: 3D views of the CTS to feeding network discontinuity.

3.3.2 Feed Geometry Optimization

In this subsection, an optimal feed geometry for the proposed design is investigated. Two square openings in the sidewall of the PPW are considered to allow for the feeding. The assumption is made that the CTS is fed by an inhomogeneous stripline in which only the fundamental mode propagates. To simulate this structure in CST Microwave Studio, a waveguide port is placed in the cross section of the structure shown in Fig. 3.4b.

The feed is characterized by the following parameters: backing reflector distance d_{br}, feed width w_{f}, feed height z_{feed}, feed length δ_{f}, cavity height h_{cav}, and cavity width w_{cav} (see Fig. 3.5). A parametric sweep over these quantities was performed in CST to evaluate their influence on the input impedance of the feed, here denoted as the active impedance Z_a.

Representative impedance plots from the parametric sweeps are shown in Fig. 3.5. These illustrate how varying each parameter impacts the real and imaginary parts of Z_a. Finding direct relationships is in general complex, since a single geometric change can simultaneously affect multiple electromagnetic characteristics. The interpretation of these results in terms of equivalent circuit is given in Appendix C.

The results of the parametric study are summarized in Table 3.1, which reports the general relationships between each feed parameter and the active impedance. Based on these results, optimum feed parameters can be selected with respect to impedance matching normalized to $Z_0 = 75\ \Omega$. A more detailed discussion of the influence of each parameter, together with additional design considerations,

is given in Appendix C.

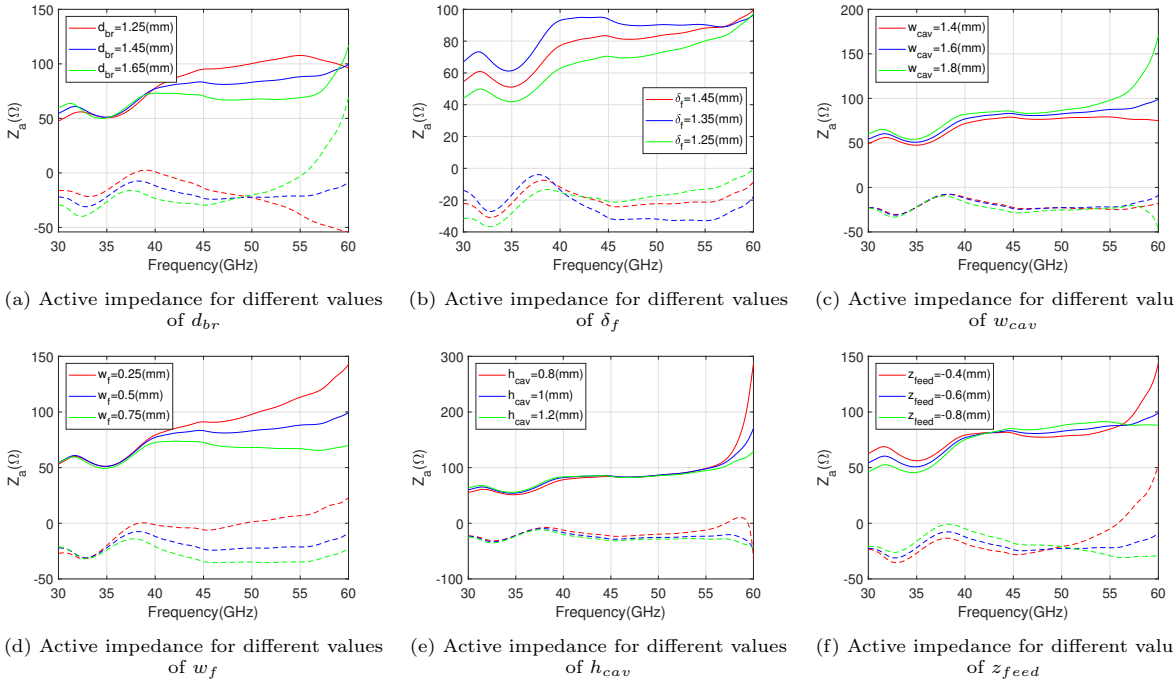

(a) Active impedance for different values of d_{br}

(b) Active impedance for different values of δ_f

(c) Active impedance for different values of w_{cav}

(d) Active impedance for different values of w_f

(e) Active impedance for different values of h_{cav}

(f) Active impedance for different values of z_{feed}

Figure 3.5: Comparison between feed parameters and impedance matching of the discontinuity.

Parameter	Re(Z_a) Low Freq	Re(Z_a) High Freq	Im(Z_a) Low Freq	Im(Z_a) High Freq
w_{cav}	→	↑	→	→
d_{br}	→	↓	↓	↑
w_{f}	→	↓	→	↓
h_{cav}	→	→	→	→
δ_{f}	↑	↑	→	→
z_{feed}	→	↓	↑	↓

Table 3.1: Effect of feed parameters on Z_a over frequency.

↑ value increases
↓ value decreases
→ no change

3.3.3 Design of Series Inductance

During the previous part of this subsection, a set of feed parameters was proposed that optimized the real part of the active impedance at the CTS to feeding discontinuity. However, the capacitive reactance of the input impedance still needs to be compensated for. This can be done by increasing the inductance per unit length of the transmission line over a very small length: $l_{induct} = 0.2$(mm) and width $w_{f,2} = 0.15$(mm) (for a more comprehensive explanation, the reader is referred to appendix C). After implementing this inductor in the CTS cavity, the active impedance can be given by Figure 3.6a and the impedance matching (given by Figure 3.6b) of the total transition is better than -15 (dB) over the entire band. It should be noted that the active impedance is significantly lower than before at high frequencies.

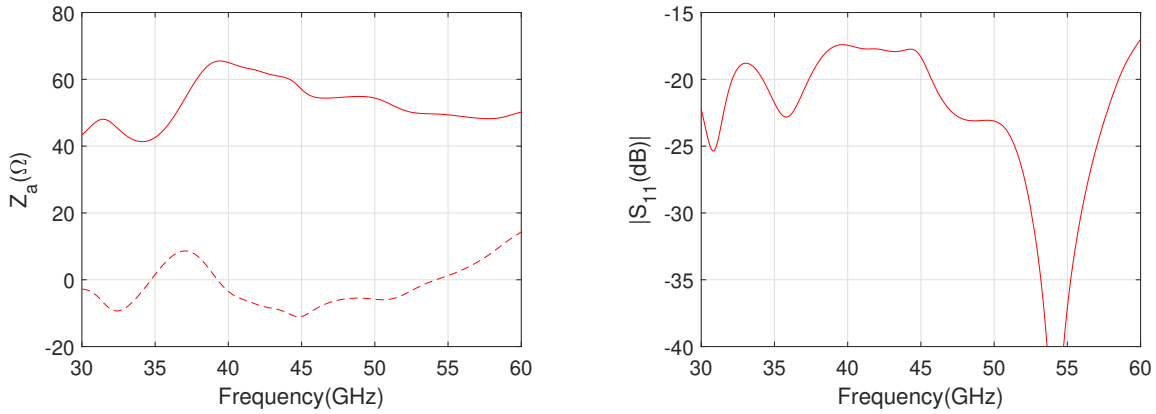

(a) Active impedance after compensating for the capacitance

(b) Impedance matching normalized to $Z_0 = 50(\Omega)$

Figure 3.6: Active impedance and impedance matching of the entire transition.

3.4 Design of the Feeding Network

In the previous section, a possible feeding transition was introduced to ensure that the CTS to feeding network discontinuity was well matched. In this section, the implementation of the feeding network connected to this transition is described. It consists of four parts:

- An inhomogeneous stripline to GCPW transition
- A taper that decreases the length between the two transmission lines
- A power combiner
- A GCPW to coaxial transition.

A schematic overview of the feed is given in Fig. 3.7.

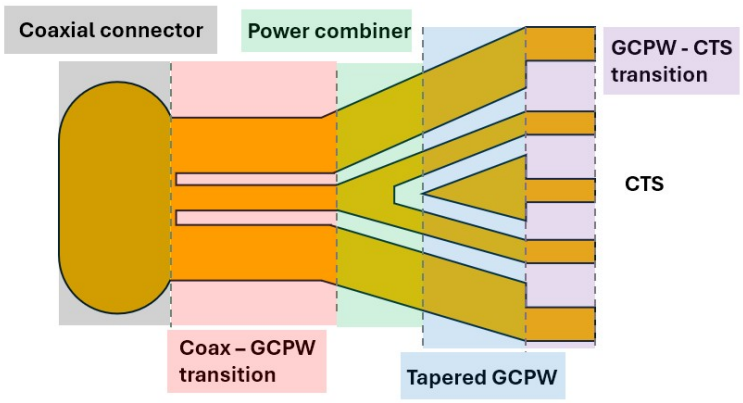

Figure 3.7: Schematic of the feeding network design.

3.4.1 Inhomogeneous Stripline to GCPW Transition

The feed is connected to the CTS through a stripline that is surrounded by a cavity. Then a GCPW with the same characteristic impedance is designed, and when these two transmission lines are added, the transition given by Figure 3.8a is implemented. From Fig. 3.8b it can be seen that the transition is well matched ($S_{11} < -29$[dB]).

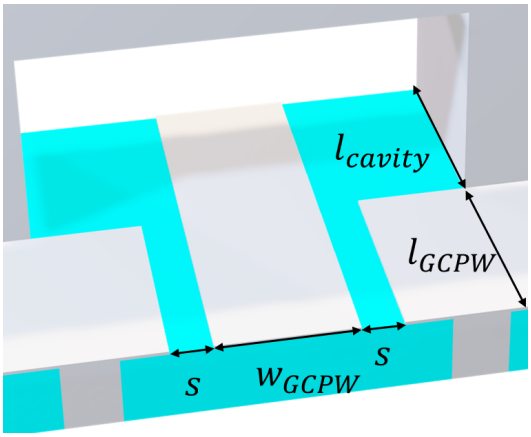

(a) 3D view of the stripline to GCPW transition with geometrical parameters:$s = 0.15$[mm], $w_{GCPW} = 0.5$[mm], $l_{cavity} = 0.75$[mm], $l_{GCPW} = 0.75$[mm]

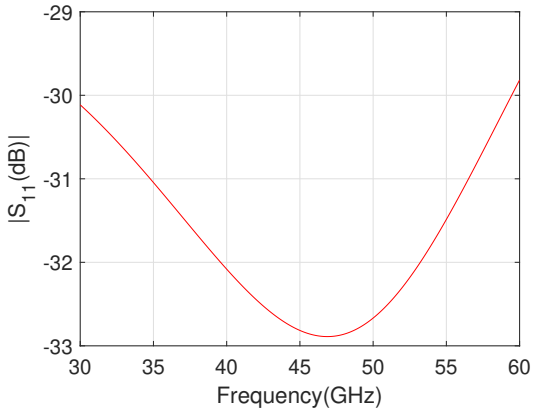

(b) Impedance matching of the transition normalized to the line impedance's $Z_0 = 50[\Omega]$

Figure 3.8: Inhomogeneous stripline to GCPW transition.

3.4.2 Taper

As described above, there are two lines feeding the CTS. These must be combined into a single feeding line. For this a power combiner is used. Combining lines with a small characteristic impedance can be difficult since the characteristic impedance of the combined line has to be half of the impedance before combining, resulting in a large microstrip width. Therefore, a tapered line is designed to transfer from 50Ω to 80Ω. A linear taper was used, and the total length of the taper was chosen as short as possible, while still providing the required bandwidth, using a parametric analysis.

This resulted in a tapered transformer with the geometry as shown in Figure 3.9a. Furthermore, from Fig. 3.9b it can be observed that the reflection coefficient of this transformer section is better than −25[dB] over the 30 to 60 GHz band.

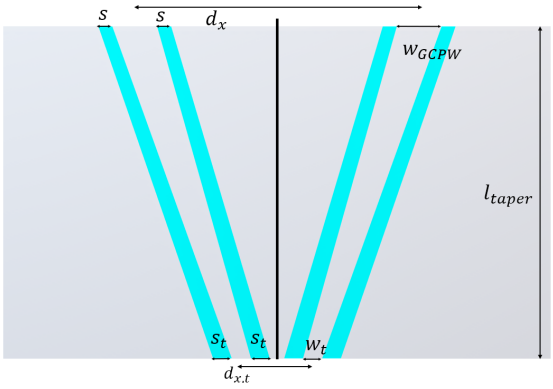

(a) top view of the tapered lines:$w_{GCPW} = 0.5$[mm], $s = 0.15$[mm], $w_t = 0.2$[mm], $s_t = 0.2$[mm], $l_{taper} = 3.5[mm]$, $d = 3.5$[mm], $d_t = 0.75$[mm]

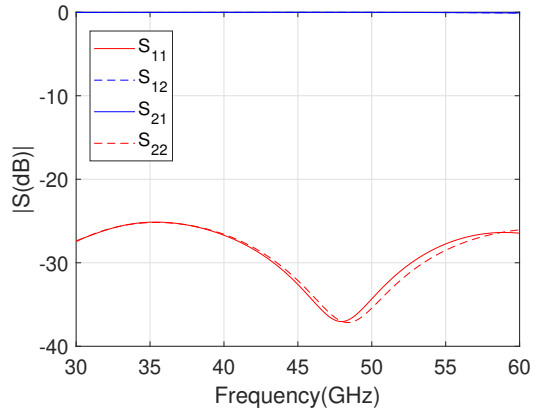

(b) Impedance matching normalized to the line impedance at the boundaries

Figure 3.9: Tapered transition.

3.4.3 Power Combiner

To properly combine the two tapered lines, that have a characteristic impedance of 80Ω, it is important to make sure the characteristic impedance of the line after power combining is equal to half the characteristic impedance of the lines before the power combiner: 40Ω. This sub design is visualized by figure 3.10a. The chosen geometry yields the reflection coefficient given in Fig. 3.10b.

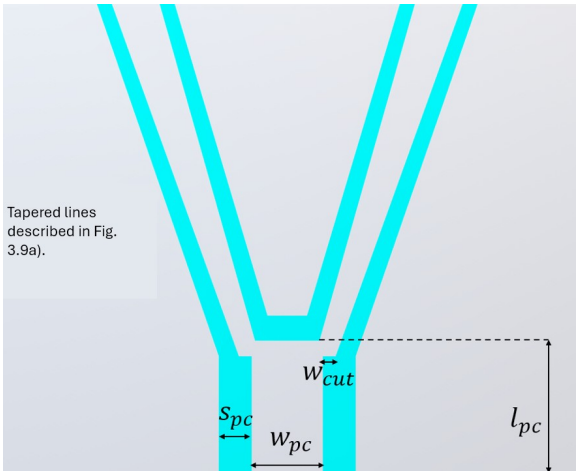

(a) top view of the taper and power combiner:$w_{cut} = 0.125[\text{mm}], w_{pc} = 0.7[\text{mm}], s_{pc} = 0.325[\text{mm}], l_{pc} = 1.3[mm]$

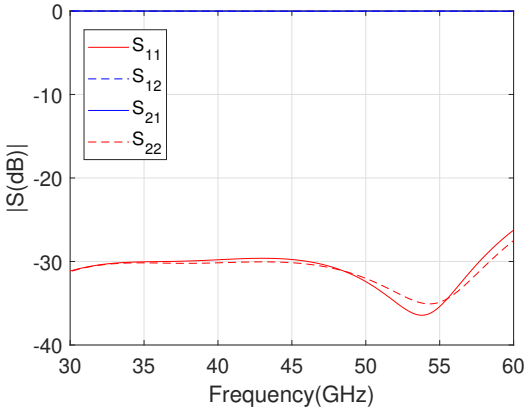

(b) Impedance matching normalized to the line impedance's at the boundaries

Figure 3.10: Power combiner design.

3.4.4 GCPW to Coaxial Transition

The last transition is from the PCB to an 1.82 mm coaxial cable. The Rosenberger 02K722-40MS3 solderless connector was selected. Because the connector introduces a reactive discontinuity, compensation was implemented by introducing a circular hole in the ground plane below the transition. A parametric analysis, shown in Figure 3.11c, indicates that a hole radius of $r_{\text{hole}} = 0.5\,[\text{mm}]$ provides optimal impedance matching. This is further supported by the S parameters in Figure 3.11d, where the reflection coefficient $S_{11} < -15\,\text{dB}$.

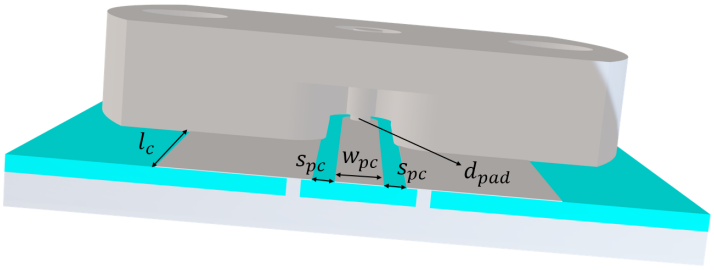

(a) 3D side view of the connector to GCPW transition:$d_{pad} = 0.7$[mm], $l_c = 3$[mm], $w_{pc} = 0.7$[mm], $s_{pc} = 0.325$[mm]

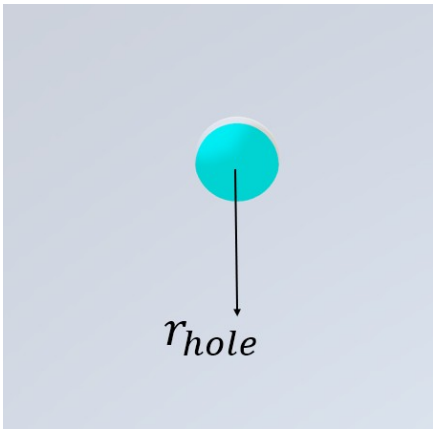

(b) 3D bottom view of the connector to GCPW transition:$r_{hole} = 0.5$[mm]

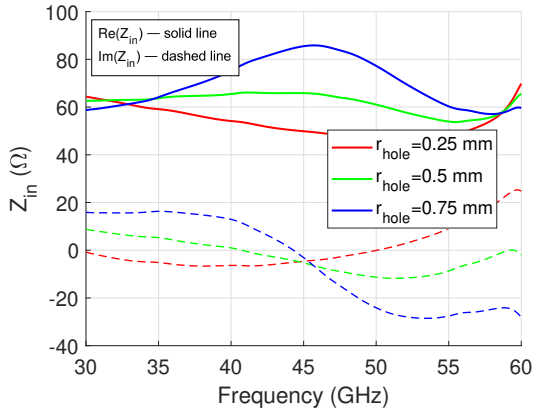

(c) Parametric analysis of the hole radius with respect to active impedance.

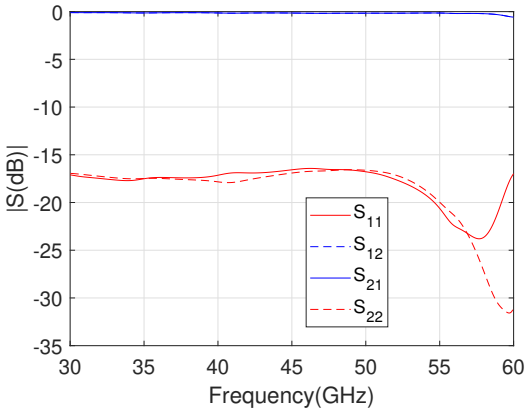

(d) Impedance matching of the coaxial to GCPW transition. Normalized to the line impedances of both transmission lines.

Figure 3.11: Connector to GCPW transition.

3.4.5 Validation of the Feeding Network

To evaluate the impedance matching characteristics of the feeding network, one can cascade all the separate components and evaluate the S-parameters of the entire transition. The result of this simulation is shown in figure 3.12a. Notable characteristics of the impedance matching response are that $S_{11} < -11$ dB over the entire band. Additionally, there is an oscillatory component in the impedance matching with a period of $\Delta f = 7.5$ GHz.

It is also useful to examine the impedance matching of the feed at a reference plane after the connector to determine whether calibrating out the connector provides benefits in terms of improved matching. This is shown in figure 3.12b. In this configuration, $S_{11} < -21$ dB, without strong oscillations in the amplitude. By comparing both simulations, one can observe that the frequency oscillations are caused by the connector, and the impedance matching is much better when the coaxial-to-GCPW transition is calibrated out.

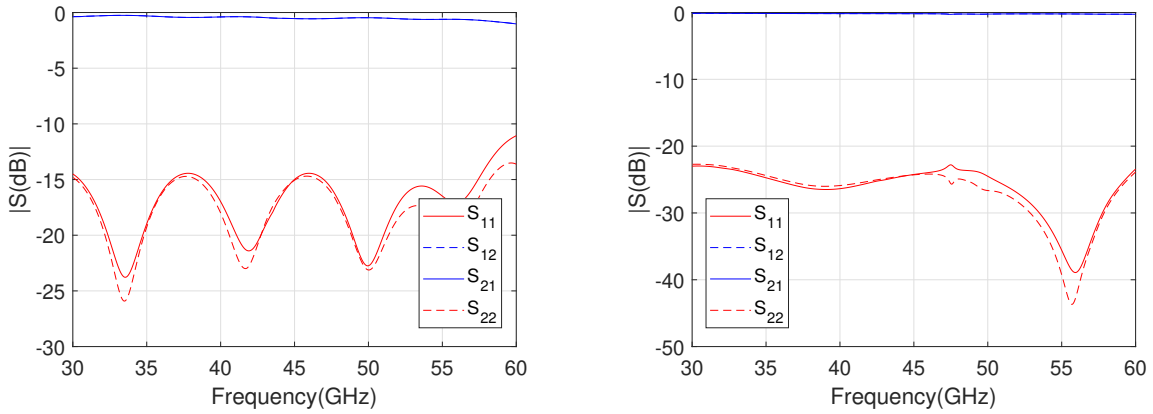

(a) Impedance matching of the entire feeding network with coaxial to GCPW transition

(b) Impedance matching of the entire feeding network without coaxial to GCPW transition

Figure 3.12: Impedance matching characteristics of the entire feeding network.

3.5 Integration of The Feeding Network

3.5.1 Simulation Setup

To ensure proper integration between the feeding network and the CTS feed, simulations were carried out for the network both before de-embedding (Fig. 3.13a) and after de-embedding (Fig. 3.13b). However, due to time constraints, only the complete quasi-optical system before de-embedding (Fig. 3.14) was simulated. An aluminum plate (component II) with a circular hole was placed beneath the lens (3.14b). This was done because the fabricated GRIN lens is mounted onto this plate to help reduce the side-lobe level.

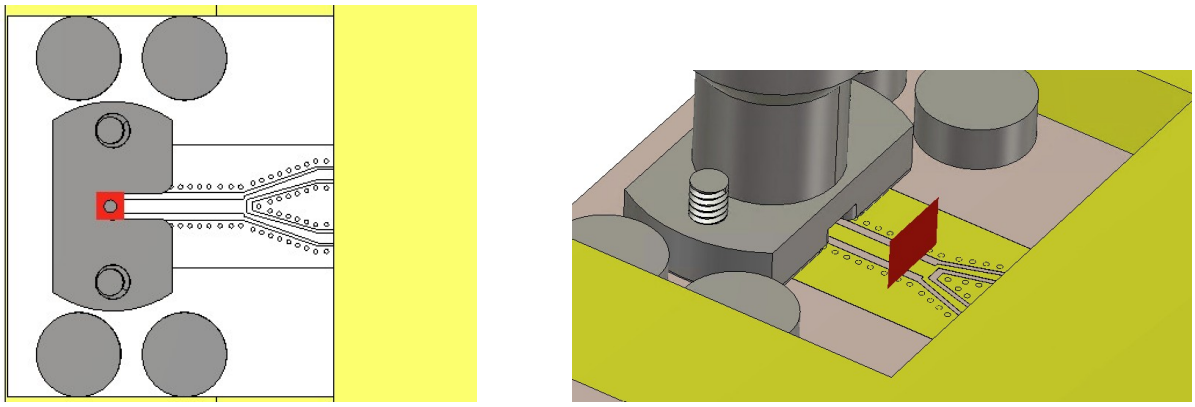

(a) CTS simulation setup I

(b) CTS simulation setup II

Figure 3.13: Simulation setup for the CTS feed before and after de-embedding.

3.5.2 Reevaluation of the CTS Feed

Since calibration of a passive element such as the coaxial to GCPW transition is possible, this subsection will report on the impedance matching of the entire feed without the transition (Figure 3.15a). It is not explicitly shown here, but it can be shown that for the cascaded system (in this case, the feeding network with the feed), there is a significant improvement in terms of impedance matching when calibrating the transition out. In addition, it should be noted that the spillover of the feed is comparable to the spillover reported in Section 3.2. The length of the entire CTS structure was slightly increased to recover a spillover larger than 60%, as shown in Figure 3.15b. This re-optimization of the CTS does not deteriorate the impedance matching since it does not depend greatly on the length of the PPW lines in the CTS, but more on the geometry of the CTS to feed discontinuity. Finally, notions about the

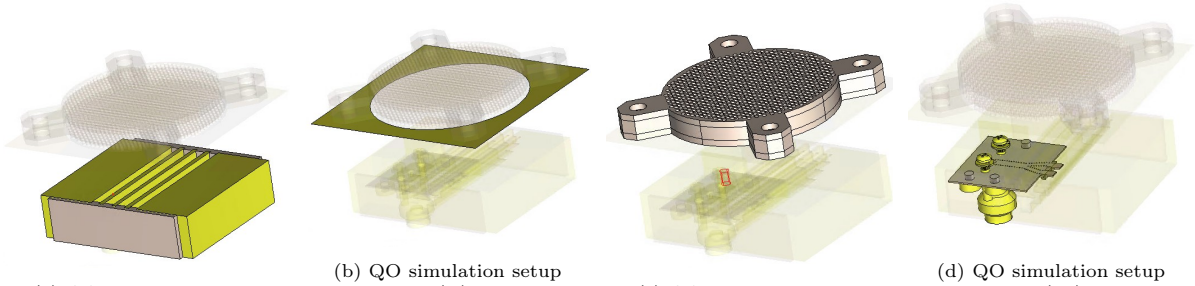

(a) QO simulation setup component (I):CTS Feed

(b) QO simulation setup component (II):aluminum plate

(c) QO simulation setup component (III):Flat Lens

(d) QO simulation setup component (IV): Feeding network

Figure 3.14: 3D overview of the QO simulation setup components.

primary patterns can be made: in the E-plane (given by Figure 3.15c), there is a slight shift of the main beam, this is due to the asymmetry in the E-plane caused by the decrease in feed length. However, this beamshift is partially compensated by the focusing of the lens. Then in the H-plane (given by Figure 3.15d) there are oscillations in the main beam. This is due to edge affects of the CTS in the H-plane.

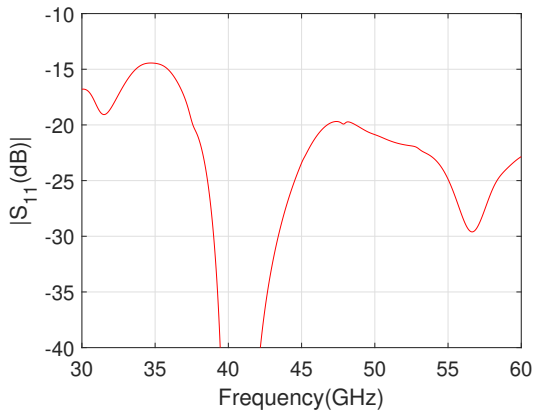

(a) Impedance matching of the CTS feed after calibration

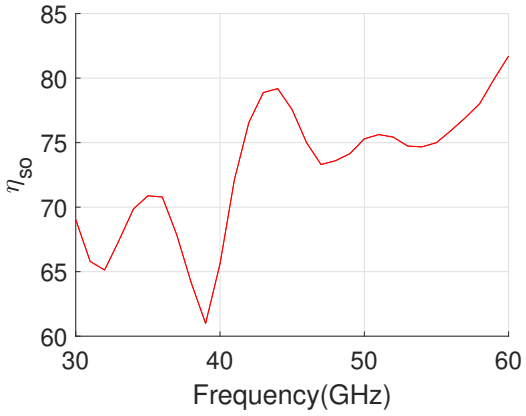

(b) Spillover of the final design

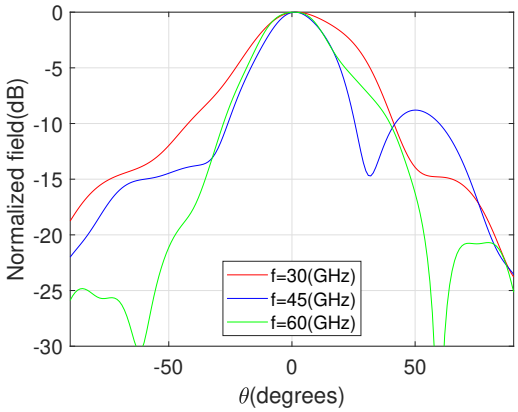

(c) Primary patterns in E-plane

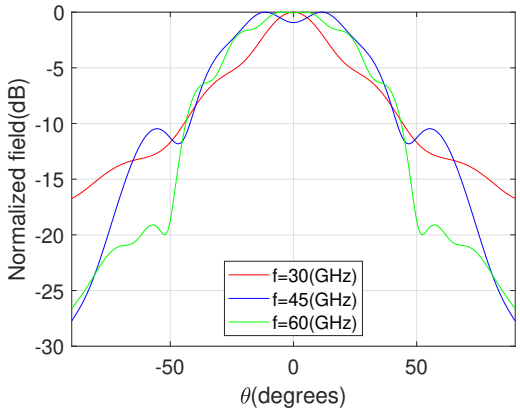

(d) Primary patterns in H-plane

Figure 3.15: Performance characteristics of the designed feed.

3.5.3 Reevaluation of Performance of Entire QO System

Similarly to Section 2.5 the entire QO system can be evaluated again, but now with the implementation of the feeding network. Furthermore, it is worth mentioning that dielectric holders made of PTFE

$\epsilon_r = 2.1$) were added to the simulation to more elaborately estimate the losses. This are placed at the sides of the CTS to keep the metal structure in place (see 3.14a). The resulting performance of the entire system in terms of efficiency, directivity, and gain can be found in figure 3.16. It should be noted that the reported matching efficiency has been calculated with the reflection coefficient before deembedding the connector to the GCPW transition, so the expected performance should be a bit above the performance reported here. Furthermore, the simulated performance shows a good match between this work and the expected improvement reported in [12].

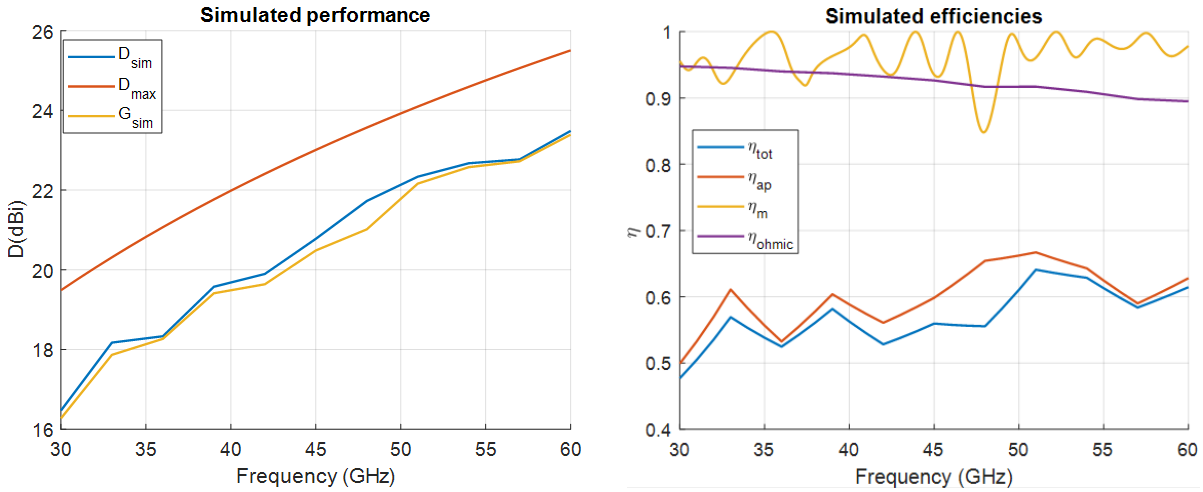

(a) (b)

Figure 3.16: Performance of the entire quasi optical system.

3.6 Conclusion and Research Objectives

A feeding solution was proposed for the CTS to PCB discontinuity, with a detailed parametric analysis. Based on these findings, the feeding network connected to the discontinuity was subsequently designed and validated. The chapter concluded with a performance evaluation of the CTS feed, both with and without calibration of the coaxial to GCPW transition. The CTS feed demonstrated good matching, with $S_{11} < -14\,\text{dB}$. Furthermore, the calculated spillover efficiency from the primary radiation patterns showed excellent agreement with previous simulations, yielding $\eta_{\text{so}} > 60\%$. Finally, the complete quasi-optical system was reevaluated and the simulations confirmed excellent overall performance with a total efficiency of approximately $\eta_{\text{tot}} \approx 50\%$.

The next chapter will focus on the experimental validation of the proposed concept. Initially, a suitable method for fabricating the aluminum CTS feeding block must be identified. This involves ensuring that the cavities can be accurately machined using a milling machine and that the floating pieces can be securely supported using two holders made of PTFE plastic. Then a practical PCB implementation of the designed feeding network must be developed, with particular attention given to the inclusion of via fences for proper grounding and isolation. Third, a TRL calibration kit should be designed and fabricated to allow accurate de-embedding of the coaxial-to-GCPW transition. Finally, experimental validation of the TRL kit, the CTS feed, and the complete QO system should be conducted through measurements.

4

Fabrication

4.1 Introduction

This chapter will focus on the following aspects:

- Section 4.2 describes the fabrication of the CTS feed. Additionally, several important considerations that were made to ease the fabrication of the CTS are highlighted.
- In Section 4.3, the Printed Circuit Board (PCB) implementation of the feeding network, the Trough Reflect Line (TRL) calibration structures, and additional PCB designs for the isolated feeding network impedance matching and loss characterization of the PCB are discussed.
- Then, in Section 4.4, the design and fabrication of a 3D printed holder to mount both the feed and lens on a measurement table is discussed.

4.2 Implementation of the CTS structure

The CTS structure was divided into a total of 8 parts and 6 unique components (including the spacers):

1. A large bulk aluminum piece (I),
2. A small bulk aluminum piece (II),
3. An aluminum plate, use as holder for the PCB (III),
4. One floating aluminum block (IV) for the center CTS,
5. Two floating aluminum blocks (V) for side PPWs,
6. Two PTFE holders (VI).

A 3D visualization of all components is provided in Figure 4.1. The bulk aluminum pieces (I & II) make up the outer part of the CTS waveguides. A metal plate was added underneath the PCB (III) - the PCB holder - has been added to ensure that the PCB does not bend or break when the coaxial connector is screwed onto the PCB. The floating aluminum blocks (IV & V) divide the CTS into multiple smaller waveguides. Since the components IV and V are ideally suspended in air, they are held in place using a PTFE holders (VI) on both sides of the CTS.

Several important considerations were made during the design and implementation of the CTS feed. In particular, the bulk aluminum body was split into two separate parts (I & II) to enable milling of the PPW openings. In addition, circular cutouts were added at the 90 degree corners of the holders to ensure compatibility with the milling paths of the tool. For a more detailed view of the mechanical implementation and drawings, the reader is referred to Appendix D.

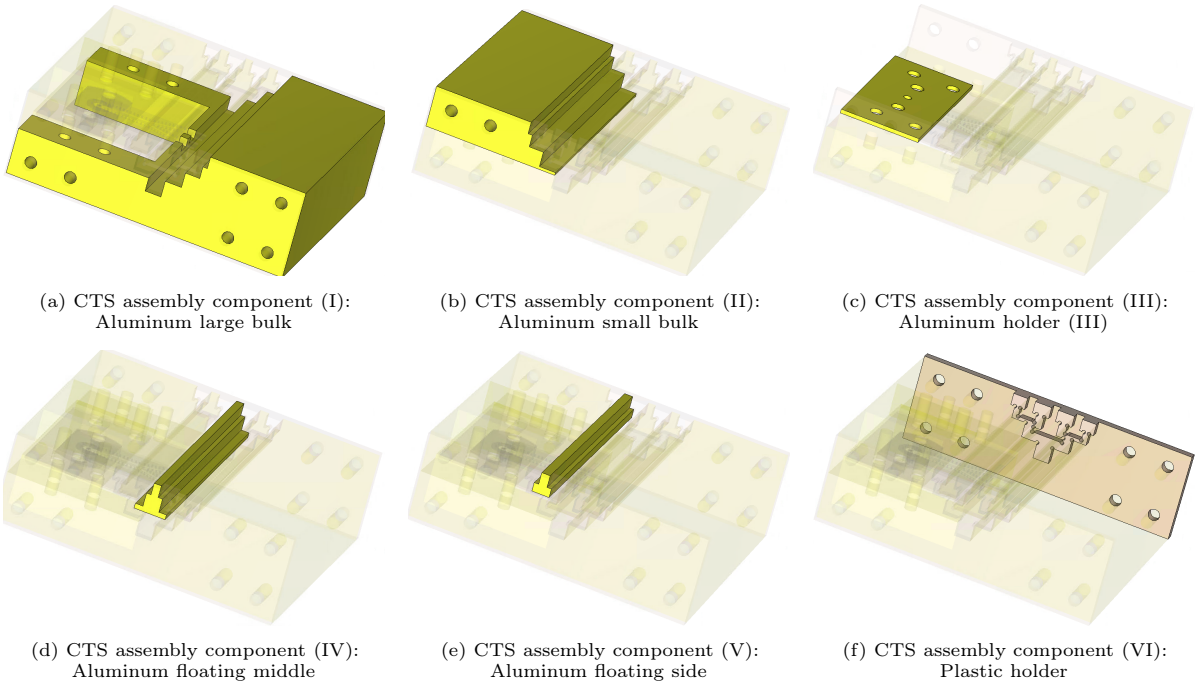

(a) CTS assembly component (I): Aluminum large bulk

(b) CTS assembly component (II): Aluminum small bulk

(c) CTS assembly component (III): Aluminum holder (III)

(d) CTS assembly component (IV): Aluminum floating middle

(e) CTS assembly component (V): Aluminum floating side

(f) CTS assembly component (VI): Plastic holder

Figure 4.1: 3D overview of all the CTS assembly components

4.3 PCB Implementation of the Proposed Feeding Network

To implement the proposed feeding in PCB, a two-metal layer PCB was used with a single dielectric layer of 254μm RO4350. In addition, all previously metallic side walls were replaced with via fences. These fences were designed with a via pitch of $p_{\text{vias}} = 0.45\,\text{mm}$ and a via diameter of $d_{\text{vias}} = 0.25\,\text{mm}$. This configuration ensured that the spacing between adjacent vias remained at 0.2 mm, which is below the standard guideline of $\lambda_{\text{sub}}/10 = 0.33\,\text{mm}$.

4.3.1 TRL Calibration Structures

As described in the previous chapter, the reflections caused by the coaxial to GCPW part of the feeding network are the highest among all the passive components. In an application where such an antenna is fed from an integrated RF chip, this transition is not present. Therefore, Trough Reflect Line (TRL) calibration structures were designed to de-embed the effect of this transition. Since TRL calibration of a 1- or 2-port passive device is a well-known technique, the details of the method are not repeated here. Additional information is provided in Appendix E.

From a design perspective, it is important to note that three transmission lines must be included on the PCB: one through connection (i.e. $\ell = 0$), one reflecting line, and one line (chosen as $\ell = \lambda_s/4$). By applying the TRL calibration procedure, the following objectives can be achieved:

- Verification of the de-embedded 1-port feed response against simulation results.
- Estimation of dielectric and conductor losses within the substrate (via a dedicated 2λ line structure on the panel).
- Validation of the performance of a back-to-back feeding PCB (dedicated design on the panel).

To confirm that the chosen TRL structures work, a CST simulation was made where the reference plane was set after the coaxial to PCB transition, and compared to a CST simulation where the reference plane was set to include the coaxial connector. The results of the de-embedding simulations are presented in Figure 4.3, and show excellent agreement with the previously reported simulation results.

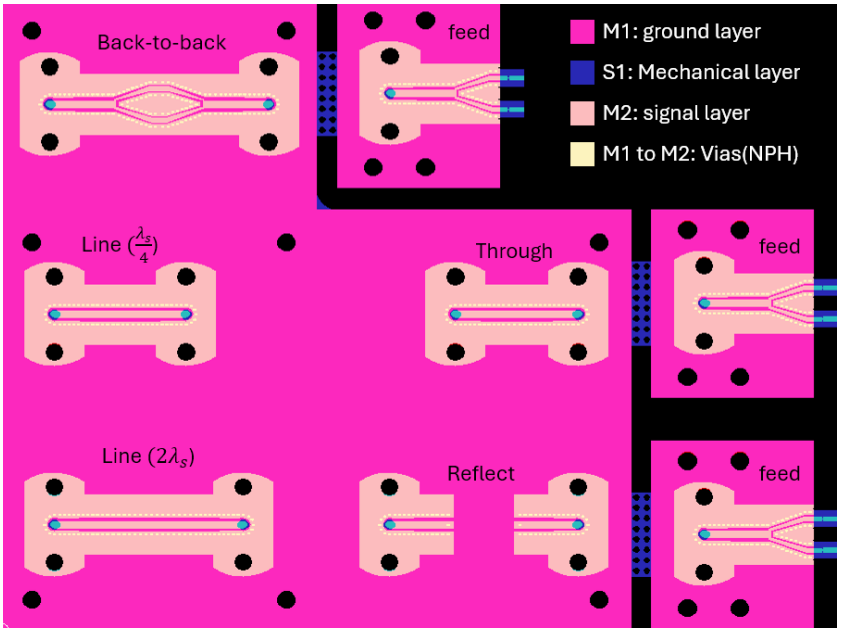

Figure 4.2: Top view of the PCB panel

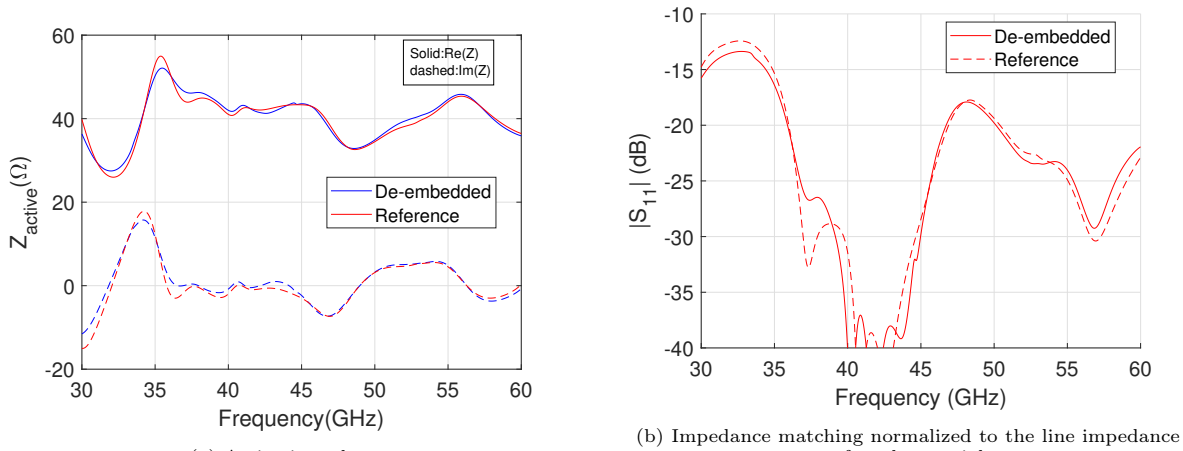

(a) Active impedance

(b) Impedance matching normalized to the line impedance after the coaxial

Figure 4.3: Active impedance and impedance matching of the de-embedded feed with both methods of simulation (Reference:simulated without the coaxial, and De-embedded: simulated with the coaxial but then de-embedded to without the coaxial).

The layout of the entire PCB panel is shown in Fig. 4.2. On a single panel, 3 feeds and the complete TRL calibration kit is printed. Furthermore, the back-to-back and 2λ line are included to assess the reflections of the power divider and the losses in the PCB, respectively. Mouse bites were added between the TRL calibration kit and three identical feeding PCBs to allow separation of the boards after fabrication.

4.4 Implementation of the PTFE Holder

To design the PTFE holder it is important to consider the following:

- The holder should ensure that the CTS can be mounted stably on a measurement table.
- The holder should allow for sufficient spacing below the CTS to ensure that a coaxial cable can be attached to the connector.

- The holder should support the flat lens and a square metal plate surrounding the lens.
- The holder should place the feed at the correct distance from the lens, as designed.

The holder is shown in figure 4.4. The design is flexible, since it can be used to measure the antenna with or without the lens. It was verified with simulation that the presence of the holder does not sensibly influence the performance of the antenna.

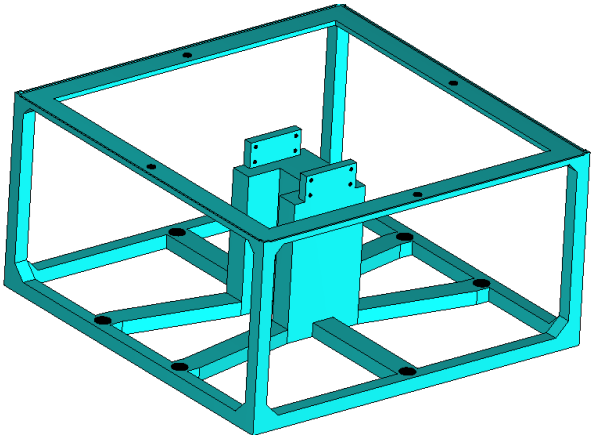

Figure 4.4: 3D view of the holder

5

Measurements

5.1 Introduction

In the previous chapters, the detailed design of the continuous transverse stub (CTS) antenna and the Printed Circuit Board (PCB) feeding structure were presented.

In this chapter, the measurements of the CTS feed and the entire quasi-optical (QO) system are discussed. The chapter is structured as follows:

- First, in Section 5.2, the choice of the connectors that are used is motivated.
- Then, in Section 5.3, the measurement setup and results of the Trough Reflect Line (TRL) deembedding are presented. Additionally, the losses of the PCB are estimated by making use of the transmission/reflection method [27].
- In Section 5.4, the measurements of the CTS feed are presented: the primary patterns from a near-field scan, the impedance matching, and the gain of the CTS feed.
- Then, Section 5.5 focuses on the measurement setup, impedance matching, patterns, and gain of the entire QO system, including the flat lens. The impact of process variation on the performance of the CTS feed is explained.

5.2 Simulations and Measurements of Broken Connector

For the measurements, Rosenberger 02K722-40MS3 solderless connectors that were used in other projects were initially employed. The measured S-parameters of a TRL structure appeared to reflect too much power, as illustrated in Fig. 5.1a. These high reflections could be explained by the fact that the used connectors were worn out, and the inner conductor of the coaxial did not make contact with the PCB.

This hypothesis was confirmed through simulations of the connector where a small gap between the inner conductor of the coaxial was included, as indicated in Fig. 5.1b. The S-parameters obtained from the simulation are comparable to the measurements, as can be seen in Fig. 5.1c. The differences in the frequency spacing of the oscillations can be explained by small details of the damage, for example the gap size and uniformity of the damage.

Furthermore, from the photo in Fig. 5.1d, a new connector (left) is compared to a used damaged connector (right). The tip of the inner conductor is pointy in the new connector, but seems flattened in the old connector (right). In the subsequent measurements, new connectors were used.

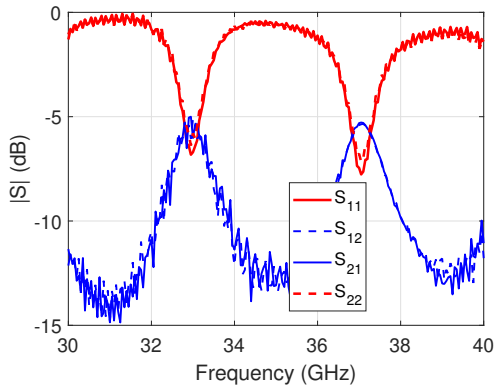

(a) Measured through circuit with the damaged connectors

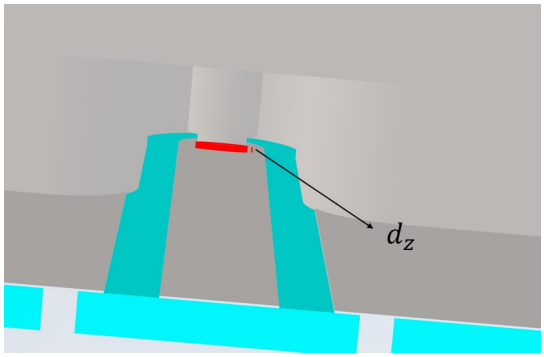

(b) simulation setup for the simulated connector without connector tip: $d_z = 0.1$[mm]

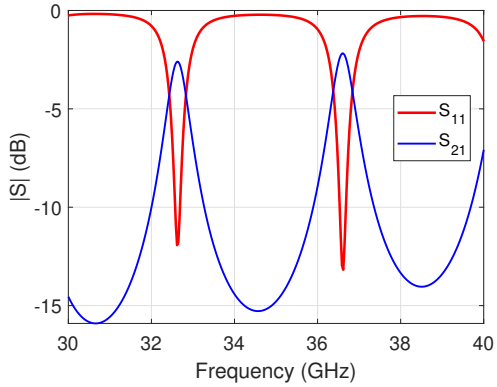

(c) S-parameters of simulation with a small gap between the PCB and inner conductor.

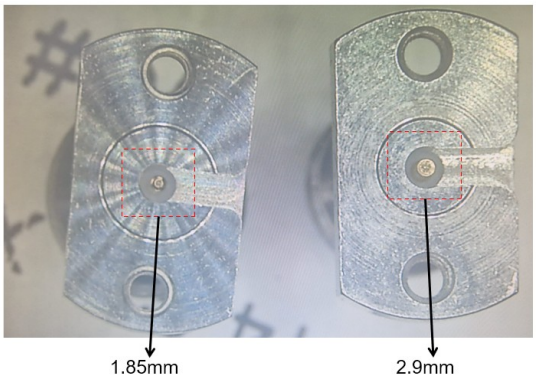

(d) Microscopic image of a new connector (left) and a worn out connector (right)

Figure 5.1: Measurement results and simulations that show that the previously used connectors are broken.

5.3 TRL Calibration Measurements

The PCB with the TRL structures was attached to a metal plate, to support the connectors, as shown in Fig. 5.2(a). The S-parameter measurements for the through, reflect and line standard are given in Fig. 5.2(b), (c) and (d), respectively. The measurements are comparable to the simulations. It should be mentioned that since the entire system is in theory symmetric, and therefore only S_{11} and S_{21} are plotted for the simulations, since $S_{11} = S_{22}$ and $S_{21} = S_{12}$. Although the results are comparable, there are some differences between the measurements and the simulations. These can be caused by manufacturing tolerances and by connector misalignment due to tolerances of the milling in the aluminum holder. Additionally, losses due to the copper surface roughness were not considered in the simulations and can explain the difference in S_{12} between simulations and measurements.

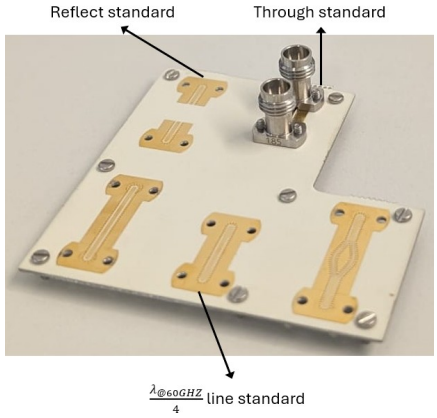

(a) Measurement setup for the TRL

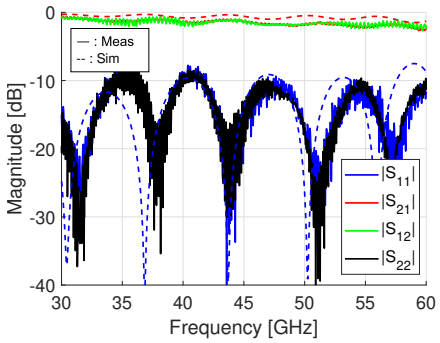

(b) Impedance matching of the through standard

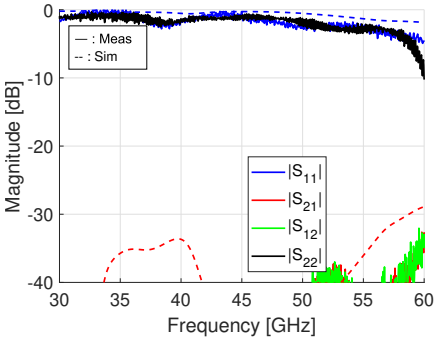

(c) Impedance matching of the reflect standard

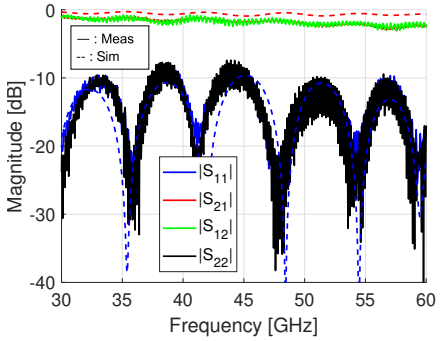

(d) Impedance matching of the $\lambda_{@60GHz}/4$ line standard

Figure 5.2: Measurement setup and measured impedance matching of the TRL structures.

5.3.1 Determining the Impedance Matching of the Feeding Network

By measuring the impedance matching of a back-to-back feeding network, given in Fig. 5.3a, and by using the previously measured TRL S-parameters, it is possible to obtain the impedance matching of the back-to-back feeding network without coaxial to Grounded Coplanar Waveguide (GCPW) transition. From the cascaded two port S-parameters given in Fig. 5.3c, the one port impedance matching given by Fig. 5.3d can be obtained. This is shown to be well matched with $S_{11} < -17$[dB].

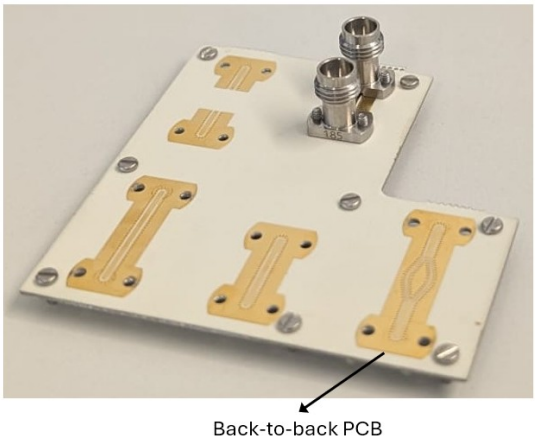

(a) Measurement setup for determining the impedance matching of the feeding network

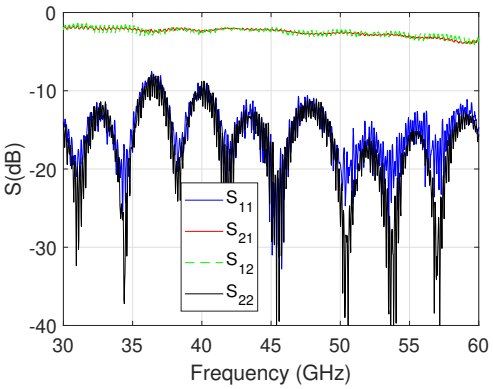

(b) Impedance matching of the back to back PCB

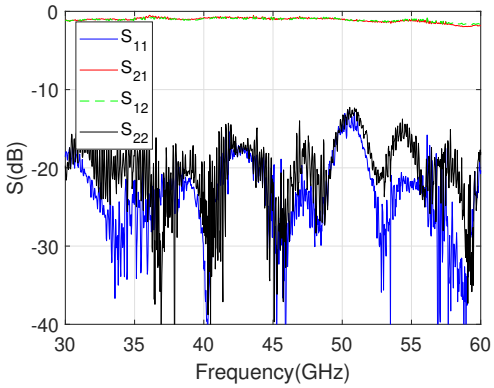

(c) Impedance matching of the back to back PCB without coaxial to GCPW transition

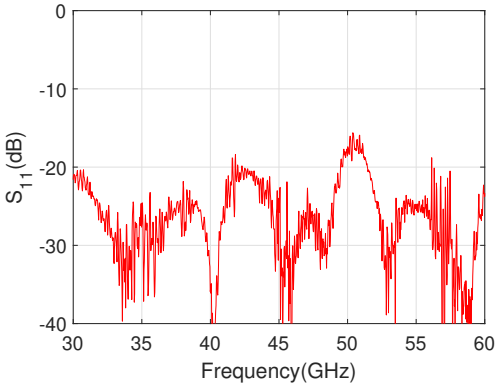

(d) Impedance matching of the feeding network

Figure 5.3: Measurement setup and results

5.3.2 Estimating the Losses in the Substrate

The measurement of the $2\lambda_s$-long line are presented in Fig. 5.4a and can be used to estimate the losses in the PCB.

Figure 5.4c shows the measured losses of the microstrip line after de-embedding the coaxial transitions. Dielectric losses with a loss tangent of the material is given as 0.0037 in the datasheet, a finite conductivity for copper and RMS surface roughness of 1.8m were accounted for in the simulation. However, the resulting losses did not show good agreement with the measured values. The influence of other factors should be investigated in more detail in future work.

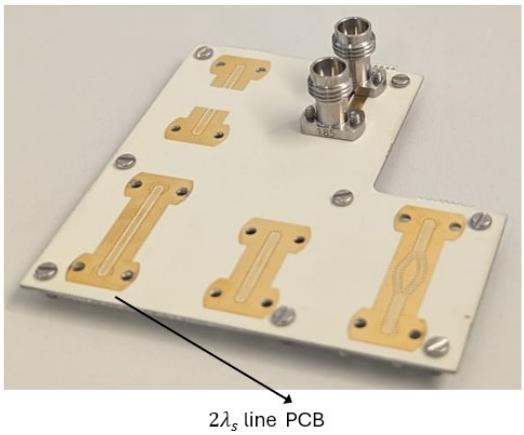

(a) Measurement setup for determining the impedance losses inside the dielectric

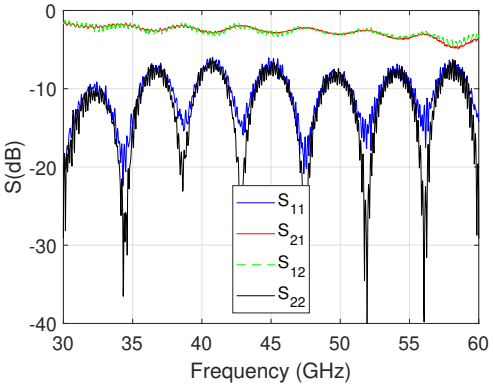

(b) Impedance matching of the $2\lambda_s$ line

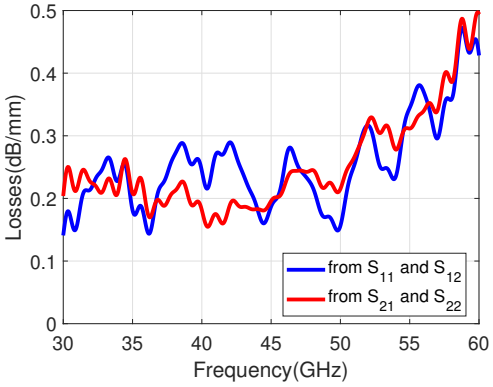

(c) Estimated losses inside the feeding network from measurements (losses from measurements also contain copper losses)

Figure 5.4: Measurement setup and results.

5.4 CTS Feed

5.4.1 Measurement Setup

To measure the impedance matching and patterns of the CTS feed, the PCB was mounted onto the CTS, as shown in Fig. 5.5a. The S_{11} was measured directly, but to measure the patterns, a planar near field scan was done. The setup is shown in Fig. 5.5b: the CTS was mounted onto a holder. A WR-28 and WR-15 open ended waveguides were used as probes to measure the near field, for the lower part of the band and the higher part of the band, respectively. These probes were mounted on a Computer Numerical Control (CNC) machine to scan over a rectangular aperture in the radiative near field of the antenna. Absorbers were used to reduce reflections.

5.4.2 Results: Impedance Matching

Figure 5.6a gives the impedance matching of the CTS feed without (blue) and with (red) applying the TRL calibration of the coaxial to GCPW transition. Although some difference can be observed with simulations, the measured reflection coefficient without the connector transition is mostly below -10dB over the entire frequency band. Some difference can be explained by the tolerance on the position of the PCB. In fact, the aluminum plate on which the PCB in mounted was measured under the microscope, as shown in Fig. 5.6c. A 100 μm difference in desired and fabricated screw positions of the PCB holder can be observed.

Other factors that can contribute to differences between simulated impedance matching and measured

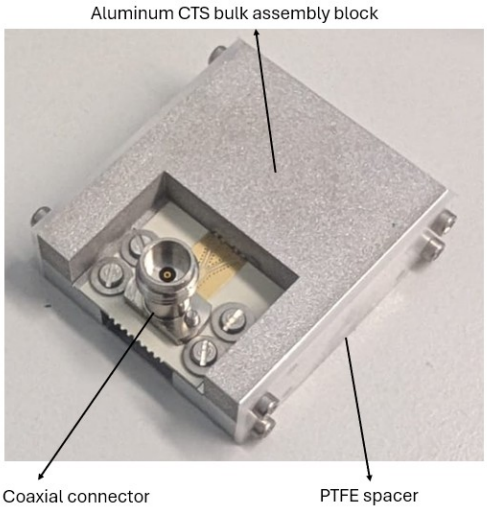

(a) Bottom view of the assembled CTS feed

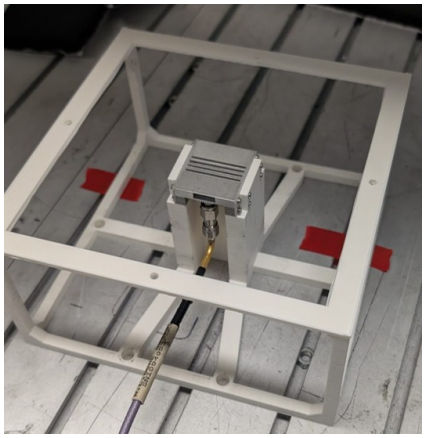

(b) Top view of the CTS feed inside the holder

Figure 5.5: Measurement setup for the CTS measurements.

impedance matching are the impact of process variation of the CTS components (for a more detail explenation see subsec 5.5.5).

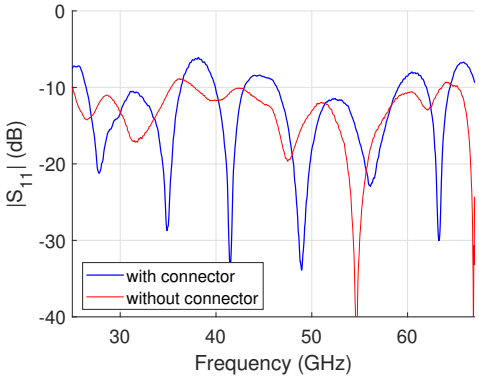

(a) Impedance matching of the CTS feed with and without coaxial to GCPW transition

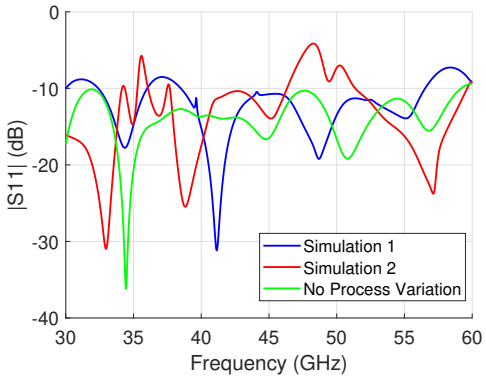

(b) The impedance matching of both simulations is compared to that of the simulation without process variations.

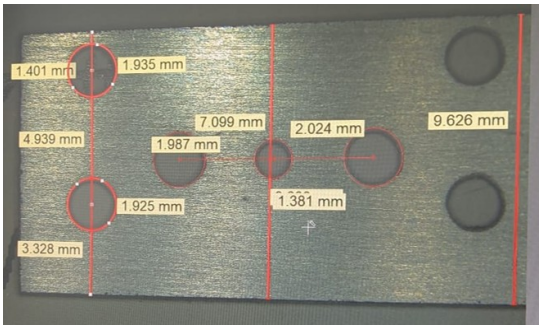

(c) Microscopic view of the PCB holder, with measured dimensions being up 100 μm different from nominal design values

Figure 5.6: Impedance matching and microscopic image of the holder.

5.4.3 Results: Primary Patterns

From the near field scan, one can obtain the far-field radiation pattern of the feed, by applying the equivalence theorem and radiating the equivalent currents on the aperture over which was measured. In Fig. 5.7, the far field radiation patterns of the CTS feed are plotted, in both the E- and H-plane, at 30, 45 and 60 GHz respectively. Overall, there is a good correspondence between the simulated and measured patterns. The main beam width is similar at the different frequencies. The side lobe level is underestimated by the measurements, especially at low frequencies.

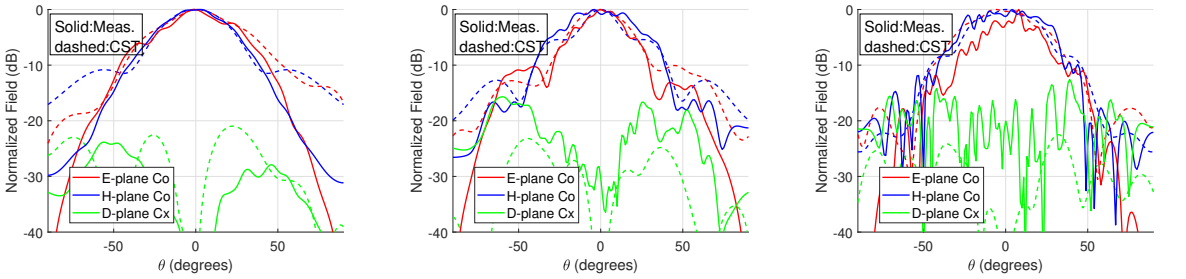

(a) Patterns in main planes of the CTS feed at 30[GHz]

(b) Patterns in main planes of the CTS feed at 45[GHz]

(c) Patterns in main planes of the CTS feed at 60[GHz]

Figure 5.7: Comparison of measured and simulated patterns of the CTS feed.

5.5 Performance of the Entire QO system

5.5.1 Measurement Setup

To measure the performence of the total quasi-optical system, a similar measurement procedure as for the feed alone was used, but now the lens was mounted on top of the holder. A photo of the measurement setup is given in Fig. 5.8. Again, a near field scan was done.

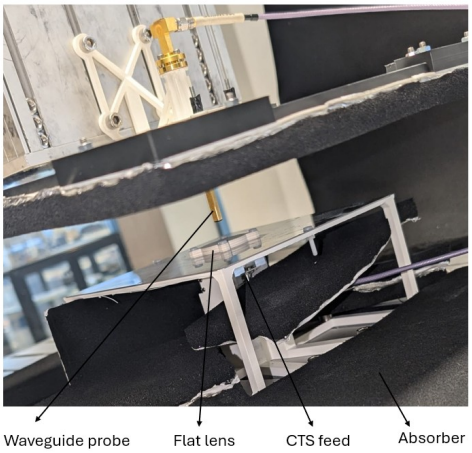

Figure 5.8: Measurement setup for the entire QO system.

5.5.2 Results: Impedance Matching

Figure 5.9a gives the impedance matching of the QO system with and without the de-embedding of the coaxial to GCPW transition. There is a significant difference between previous simulations of the impedance matching of the feed and the measured feed because of process variation as will be explained in subsection 5.5.5. Fig. 5.9b quantifies the difference in matching efficiency compared to the simulation and it can be seen that a loss in 1.5[dB] is observed for some of the measurements.

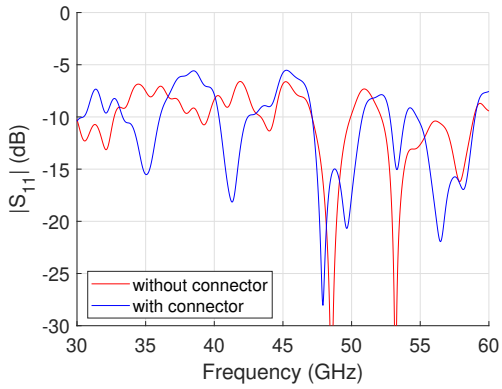

(a) Impedance matching of the QO system with and without the coaxial to GCPW transition

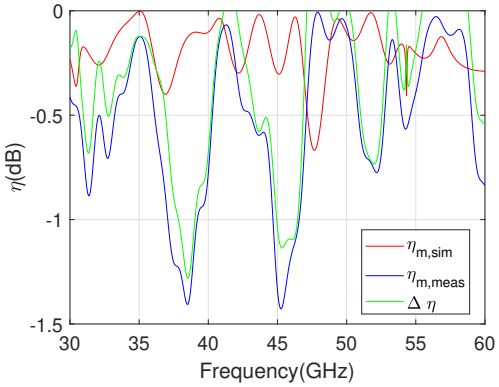

(b) η_{m} for simulation and measurement

Figure 5.9: Impedance matching and comparison of η_m for simulation and measurements.

5.5.3 Results: Secondary Patterns

Fig. 5.10 gives measured patterns in the dominant planes at 30[GHz], 45[GHz], and 60[GHz]. The observation can be made that at the lower part of the band the measured pattern is more directive that the simulated pattern. This is probably due to the fact that the aperture of the rectangular scan did not include all the radiated power.

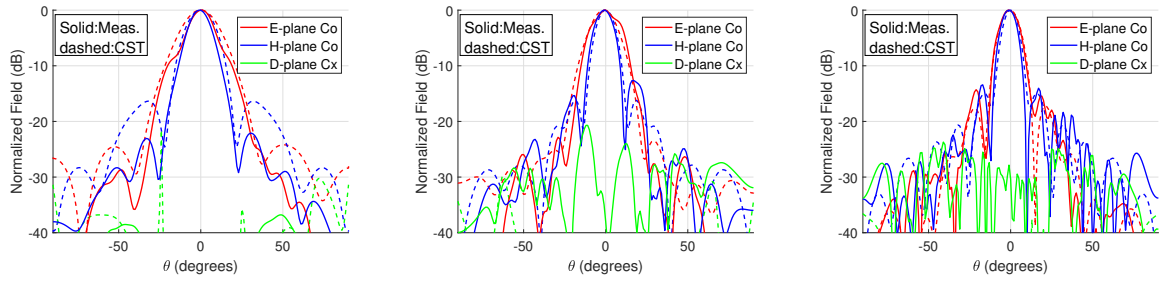

(a) Secondary patterns at 30[GHz] (b) Secondary patterns at 45[GHz] (c) Secondary patterns at 60[GHz]

Figure 5.10: Comparison of measured and simulated patterns of the far field patterns of the QO system.

5.5.4 Measurement Results: Gain of the QO system

By placing the probe in the far field of the QO system, the gain of the antenna can be measured accurately. Considering the maximum distance between the two antennas on the CNC machine is 340 mm and applying the standard far-field criterion from [28], it can be concluded that the probe operates in the far field of this antenna up to 50 GHz.

Measurements conducted above this frequency may experience slight gain degradation due to non-ideal measurement conditions. Additionally, the gain of the waveguide probe can be determined using the two-antenna method described in [29].

Figure 5.11 shows the measured and simulated gain compared to the maximum theoretical directivity of an antenna with the same aperture, with de-embedding applied for the coaxial-to-PCB transition. One could compare the results with the measured gain of the waveguide-fed feed[12], showing that the overall performance is comparable to measurement setups employing different waveguide feeds.

The measured gain is lower than expected from simulations, which can be attributed to four main factors:

(i) copper surface roughness losses were not accurately known and therefore not correctly modeled in the simulations;

(ii) The estimation of the waveguide probe gain may be inaccurate because it was determined using a two-antenna measurement method. This approach assumes that both probes have identical gain, which might not be the case in practice. Any mismatch between the gains of the two probes directly introduces error into the measurement. A more accurate method would have been to use a calibrated standard gain horn antenna as a reference; however, such antennas were not available in the lab.

(iii) process variations affecting the feed performance, as discussed in subsection 5.5.5, particularly the presence of a cavity between CTS components I and II. A possible way to mitigate the effects of process variation is to use Electromagnetic Band Gap (EBG) structures to suppress higher-order modes [30], or to apply conductive foil or paste inside the cavity.

(iv) Inaccuracies in de-embedding of the adapter in the WR-28 waveguide measurements: for the gain measurements in this frequency band, a 2.92 mm to 1.85 mm adapter had to be used. Since only one such adapter was available, the TRL calibration was performed with non identical adapters, introducing potential inaccuracies in the de-embedding.

To validate these observations regarding process variation, microscopic images were captured of both the top and side of the feed, as shown in Figure 5.11b. These images confirm the placement of the components and verify the spacing between them.

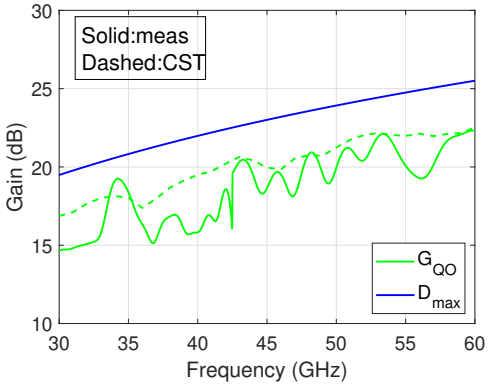

(a) Gain of the flat lens fed by the CTS measured with the WR-28 until 42.5GHz and the WR-15 waveguide probe from 42.5GHz

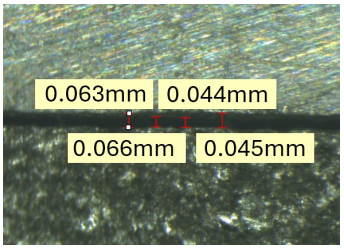

(b) Observed distance between the CTS components I and II is 50[μm]

Figure 5.11: Figures related to the gain measurement of the entire QO system.

5.5.5 Impact of Process Variation

In the fabrication of the CTS feed, there is an uncertainty in the feature size accuracy of approximately 100 μm. The effect of this uncertainty on impedance matching and pattern quality is examined for the following two cases:

- The positioning of the PCB in the aluminum CTS structure: due to process variations in the positioning of holes in the aluminum PCB holder, the feeding PCB could be displaced by 100 μm, causing the feed lines not to enter the desired distance into the CTS. This concept is illustrated in Figure 5.12a.
- A gap of up to 100 μm between parts (I) and (II) of the CTS, due to the components not being completely flat or not being held in place tight enough, as shown in Figure 5.12b.

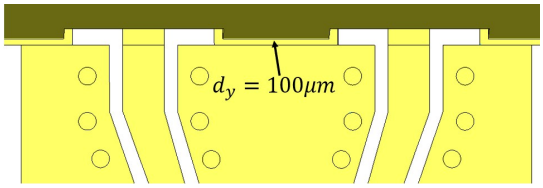

(a) Simulation 1: top view of the by d_y displaced feeding PCB

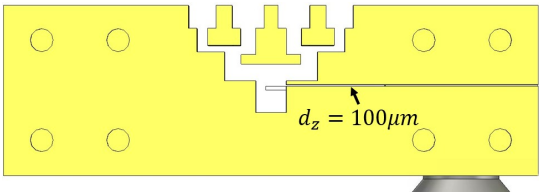

(b) Simulation 2: Side view of the CTS simulation with a 100[μm] gap between CTS assembly components (I) and (II)

Figure 5.12: Simulation setup to quantify the effects of process variation.

Figure 5.13a shows the impedance matching for the feed both without process variations (green) and with the two different cases of variation. Furthermore, as illustrated in Figure 5.13b, a difference in gain can be observed when a small gap exists between the CTS assembly components. At some frequencies, this can significantly limit the performance of the QO system.

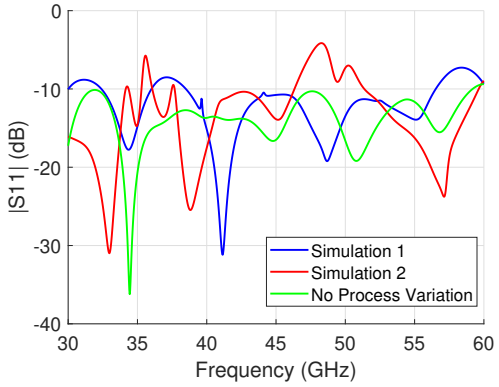

(a) The impedance matching of both simulations is compared to that of the simulation without process variations.

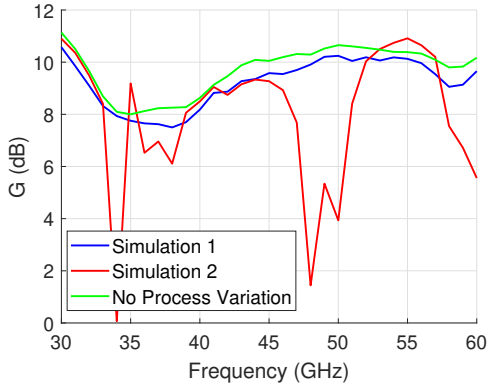

(b) Resulting broadside gain in simulation

Figure 5.13: Simulation results that show process variation influences the performance of the QO system

6

Conclusion & Future Work

6.1 Conclusion

In this thesis, a compact wideband continuous transverse stub (CTS) feed design for a gradient index (GRIN) lens operating at millimeter-wave (mmWave) frequencies was presented. A complete feeding implementation for the proposed design was developed, and the fabrication process was discussed in detail. Subsequently, measurements of both the fabricated feed, its feeding network and the complete quasi-optical (QO) system were conducted and analyzed. Furthermore, the impact of process variations on system performance was investigated, with particular emphasis on their influence on the measurement results.

The main conclusions drawn from this work are as follows:

1. A compact wideband feed can be successfully designed using a CTS antenna array excited by two strips.
2. The feed can be used to illuminate a flat lens over an octave bandwidth from 30 to 60 GHz with stable efficiency.
3. Process variations significantly affect the performance of the QO system, with the primary contributor being the formation of unintended cavities between assembly components.

6.2 Future Work

To further improve the performance and robustness of the proposed system, future work should focus on mitigating the effects of assembly-induced losses. The main cause of undesired losses could be attributed to the gap between the two aluminum blocks that compose the antenna. A few potential approaches are recommended:

- The integration of Electromagnetic Band Gap (EBG) pin beds as introduced in [30], which can reduce undesired leakage and improve overall system integrity. However, this solution can potentially reduce the bandwidth of the antenna.
- The inclusion of additional screws to tighten the connection between the two blocks to avoid air gaps.
- The application of conductive paste of metal foils between the CTS assembly components to enhance electrical continuity and minimize losses caused by assembly gaps.

In addition, exploring advanced manufacturing techniques and tighter fabrication tolerances could further reduce process variations, leading to improved measurement consistency and overall system efficiency.

To further advance the state-of-the-art in QO systems using flat lenses, several important challenges remain:

- Scanning capability: This can be addressed by integrating an array of wideband feeds in the focal plane array of the lens to generate multiple beams. Alternatively, a two-lens system, following the approach in [31], can be realized. A key trade-off in this design is between scan range and polarization purity.
- Polarization control: Achieving dual or circular polarization is particularly relevant in communication applications. The current CTS antenna is not compatible with dual-polarization operation. However, connected arrays with dual polarized elements could be used in these cases.
- High directivity: Designing flat lenses with higher directivity can be desired in some applications, to compensate for the high free-space loss at mmWave frequencies. A larger and thus more directive lens could be made by increasing the overall thickness of the lens or an alternative approach would be to use an array of the already designed GRIN lenses.

A

Appendix A: Analysis Method

This appendix outlines the model used to address key design considerations for the system. The analysis begins with the application of the Method of Moments (MoM) to study a finite-by-finite connected array. This array includes a backing reflector, metallic sidewalls, a substrate beneath it, and an intermediate slab situated between the array and an artificial dielectric layer (ADL) structure above.

The chapter then explores various taper distributions for the feeding gaps within the array, with the aim of obtaining critical insights to guide design decisions. The role of the dielectric slab and the ADL is thoroughly investigated, focusing on their potential to enhance impedance matching without compromising the radiation patterns.

A.1 Model Definition

Problem Definition

As described in [23], we consider a grid of connected slots, as shown in Fig. A.1. The array consists of M parallel x-oriented slots, with indexes $m \in \{1, \ldots, M\}$ and centered at periodic locations $y = md_y$. Each slot is fed by delta gap generators at N locations spaced by d_x and is interrupted by metal terminations. The method assumes that the metal terminations are of finite length such that the spectral solution for infinite slots can be used as in [32]. The array plane can be embedded within a general stratified medium along z that can, for instance, include dielectric substrates or superstates, a backing reflector, or artificial dielectric layers(ADLs).

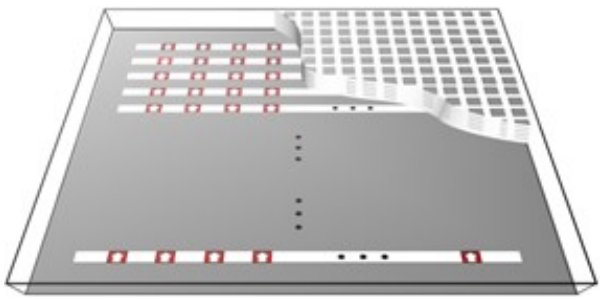

Figure A.1: Finite connected slot array with artificial dielectric superstrate

A.1.1 Space Domain Integral Equation

According to the procedure outlined in [33], an integral equation can be formulated by enforcing the continuity of the x-component of the magnetic field across the slots. By applying this method, Equation A.1 can be derived. In this equation, the left-hand side (LHS) represents the scattered magnetic field

(H field) resulting from all the slots, as observed along the axis of the m-th slot.

The scattered field is expressed as a convolution of the equivalent magnetic current density on the slots (m_x) with the xx component of the dyadic spectral Green function (g_{xx}). This formulation relates the magnetic field to the magnetic currents while accounting for the stratified medium situated above and below the slots.

The right-hand side (RHS) of A.1 represents the sum of all surface electric currents in the slot, flowing through the feeding gaps and metal terminations. This current is expressed using equation A.2. For this analysis, it is assumed that the current generator basis functions $f_{n'}$ are constant over each gap defined on the feeds and terminations, and are centered at x_n with unknown coefficients. Furthermore, these basis functions are constant or exhibit edge singularities at the metal terminations, as described in [32], and are known in both the spatial and spectral domains. A critical assumption in this analysis is that the slot is uniformly equipped with a rectangular delta-gap feed.

$$\iint m_x(x',y')g_{xx}(x-x',md_y-y')dx'dy' = -j_{y,gaps}(x,md_y) \tag{A.1}$$

$$j_{y,gaps}(x,md_y) = \sum_{n'=0}^{N+1}(i_{n'm} - Y_L v_{n'm})f_{n'}(x-x_{n'}) \tag{A.2}$$

By definition, the imposed currents are zero for the passive metal terminations. Additionally, the integral equation can be solved by assuming that the magnetic current is a separable function for each slot. Therefore, the magnetic current can be expressed as shown in equation A.3.

$$m_x(x',y') = \sum_{m'=1}^{M} v_{m'}(x')m_t(y'-m'd_y) \tag{A.3}$$

In this equation $v_{m'}$ are the unknown voltage distributions and $m_t(y)$ is an edge singular distribution. This comes from the assumption that the slot has a small width compared to the wavelength. By plugging the equations introduced before into the integral equation one can write equation A.1 as A.4 (in this equation d'_{mm} is the green function of the connected array [34]).

$$\sum_{m'=1}^{M}\int_{-\infty}^{\infty} d_{mm'}(x-x')v_{m'}(x')dx' = \sum_{n'=0}^{N+1}(Y_L v_{n'm} - i_{n'm})f_{n'}(x-x_{n'}) \tag{A.4}$$

A.1.2 Spectral Domain Integral Equation and Solution

By transforming equation A.4 into the spectral domain, we obtain equation A.5. In this equation, $V_{m'}(k_x)$ represents the unknown voltage spectrum along each slot, and $F_{n'}$ is the Fourier transform (FT) of the basis function $f_{n'}$. The term $D_{mm'}$ denotes the spectral Green function (SGF) of the connected array. This function can be written as the sum of the upper part and the lower part of the configuration. During this work, the lower part of the configuration has side walls and therefore the SGF of the upper part of the slots and the lower part of the slots are entirely decoupled, as was discussed in [25]. Because of this the matrix of the SGF of the slots looks like equation A.6

$$\sum_{m'=1}^{M} D_{mm'}(k_x)V_{m'}(k_x)dx' = \sum_{n'=0}^{N+1}(Y_L v_{n'm} - i_{n'm})f_{n'}F_{n'}(k_x)e^{jk_x x_{n'}} \tag{A.5}$$

$$\mathbf{D} = \mathbf{I}D_{down}(k_x) + \mathbf{D}_{up}(k_x) \tag{A.6}$$

It can be shown that matrix entries mm' are expressed as equation A.8. For configurations involving slots (i.e., magnetic sources), the SGF in this integral equation is given by

$$G_{xx} = -\frac{i_{TE}k_x^2 + i_{TM}k_y^2}{k_\rho^2}\,. \tag{A.7}$$

In this expression, the TE and TM currents are solutions to the equivalent transmission (TX) line problem for the stratified medium above.

Additionally, the SGF of the part below is equal to a Floquet sum given by equationA.9. This Floquet sum comes from the fact that if the image theorem is applied to the side walls each slot sees an infinite amount of slots from below. For a more elaborate discussion on this formula the reader is referred to [25]. The $G_{xx,down}$ function is the previously mentioned GF but now with the TE and TM currents corresponding to the solution of the TX-line problem of the backing reflector.

$$D_{mm',up}(k_x) = \frac{1}{2\pi}\int_{-\infty}^{\infty} G_{xx,upp}(k_x,k_y)J_0\left(\frac{w_s k_y}{2}\right)e^{-jk_y(y_m-y_{m'})}dk_y \tag{A.8}$$

$$D_{down}(k_x) = \frac{1}{d_y}\sum_{m_y=-\infty}^{m_y=\infty} G_{xx,down}\left(k_x,-\frac{-2\pi m_y}{d_y}\right)J_0\left(-\frac{2\pi m_y}{d_y}\frac{w_s}{2}\right) \tag{A.9}$$

By considering each axis of the slot as an observation point, equation A.5 can be compactly rewritten in matrix form as equation A.10. By then inverting the matrix of the SGF of the connected array and applying the Galerkin projection method, the equation A.10 can be reformulated as the equation A.11. In this equation, each entry of the impedance matrix can be calculated using equation A.12. Additionally, Z_L is a matrix representing the load impedance's of the connected array, defined as $\frac{1}{Y_L}$ for active feeds and zero for terminations. The active current into each port is given by $\mathbf{i}_A = \mathbf{Z}^{-1}\mathbf{v}$, and the impedance at each of the feeds can be found using equation $Z_{A,nm} = \frac{v_{nm}}{i_{A,nm}}$.

$$\mathbf{D}(k_x)\mathbf{V}(k_x) = \sum_{n'=0}^{N+1}(\mathbf{Y}_L\mathbf{v}_{n'm} - \mathbf{i}_{n'm})f_{n'}F_{n'}(k_x)e^{jk_x x_{n'}} \tag{A.10}$$

$$\mathbf{v} = (\mathbf{Z_L} + \mathbf{Z})^{-1}\mathbf{Z}_L\mathbf{Z}\mathbf{i} \tag{A.11}$$

$$Z_{nn'mm'} = \frac{-1}{2\pi}\int_{-\infty}^{\infty} D^{-1}(k_x)_{mm'}F_{n'}(-k_x)F_{n'}(k_x)e^{-jk_x(x_n-x_{n'})}dk_x \tag{A.12}$$

Important notions concerning the functions in integral equation (A.12) include the basis functions. These are either the sinc function (resulting from the rectangular current distribution on the slot) or the Fourier transform of the edge singular distribution [32] for the shorts on the edges.

A.2 Efficient Implementation

A.2.1 Implementation Aspects

The integral represented in (A.12) is a double integral that can be solved numerically. To make the model as time efficient as possible, a couple of important considerations need to be properly addressed.

1. Integration Domains: Choosing an appropriate method for the integration in k_x by making use of asymptotic extraction. Doing this can lead to faster convergence of the integral, thereby reducing computational time significantly.
2. Exploiting Symmetry: The symmetry in the Slot Spectral Green's Function (SGF) and the impedance matrix should be leveraged. Recognizing and utilizing these symmetries can significantly reduce the number of calculations required.
3. Caching Basis Functions: Frequently used basis functions should be saved in the cache to avoid redundant computations.

While the last two points are mainly about proper bookkeeping and will not be discussed in detail here, efficiently solving the integrals is crucial. This relies on the asymptotic extraction method, which should be explained for the reader's understanding.

A.2.2 Acceleration of the asymptotic part

For large transverse wave numbers, the SGF is dominated by the near field surrounding the slot. By making use of this assumption, one can add and subtract the semiinfinite Green functions to the integral equation A.8 and write equation A.8 as A.13. In this equation, the analytic expression of the greens function of the homogeneous greens function is known and is given by A.14[35]. In this equation $\kappa = \sqrt{k_{up}^2 - k_x^2}$ and ζ_0 and k_0 are the free space wave number and impedance.

$$D_{mm',up}(k_x) = D^{diff}_{mm',up}(k_x) + D^{\infty}_{mm',up}(k_x) \tag{A.13}$$

$$D_{mm'}(k_x) = \frac{-1}{2k_0\zeta_0}\kappa^2 \times \begin{cases} J_0\left(\frac{w_s}{4}\kappa\right) H_0^{(2)}\left(\frac{w_s}{4}\kappa\right), & \text{for } m = m' \\ H_0^{(2)}\left((d_y(m'-m)\kappa\right), & \text{for } m \neq m' \end{cases} \tag{A.14}$$

A.2.3 Radiation Patterns

Since the active currents on the slots are known, the voltage on the slots can be easily calculated in the spectral domain using equation A.15. The next step is to transform the voltages back to the spatial domain and apply a window to the equivalent spatial voltages. This windowing process is performed to exclude fictitious waves traveling to $\pm\infty$ at the edges of the array. Figure A.2 illustrates this process effectively.

After windowing in the spatial domain, the voltages on the slots are transformed back to the spectral domain. These voltages can then be used in equation A.16 to calculate the magnetic currents on the slots in the spectral domain. From these magnetic currents, the far field can be calculated using the stationary phase point method. The far field of the feed is thus given by A.17. In this equation, the spectral wave numbers $k_{x0} = k_0\cos(\phi)\sin(\theta)$, $k_{y0} = k_0\sin(\phi)\sin(\theta)$, and $k_{z0} = k_0\cos(\theta)$ are defined by the observation point (r, ϕ, θ).

$$\mathbf{V}(k_x) = -\sum_{n'=0}^{N+1} \mathbf{D}^{-1}(k_x)\mathbf{i_A}F_{n'}(k_x)e^{jk_x x_{n'} d_x} \tag{A.15}$$

$$M(k_x, k_y) = \sum_{m=1}^{M} V_m(k_x) J_0\left(\frac{k_y w}{2}\right) e^{jk_y m d_y} \tag{A.16}$$

$$H_{x,y,z}(\theta_o, \phi_o, r) \approx jk_{z0}G^{HM}_{(x,y,z)x}(k_{x0}, k_{y0})M(k_{x0}, k_{y0})\frac{e^{-jk_0 r}}{2\pi r} \tag{A.17}$$

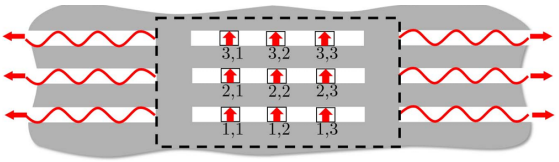

Figure A.2: spatial domain windowing approach for a 3x3

A.2.4 Model Extensions

To truly have a comprehensive model of the configuration, one could also consider the flat lens placed above the Artificial Dielectric Layer (ADL). This can be modeled by adding all the ADL layers of the lens in the transmission line above. However, this will not be done since it can be assumed that the Gradient Refractive Index (GRIN) lens is assumed to be in the far field of the feed.

However, the model will incorporate 4 additional functionalities to test proposed more comprehensive designs. These functionalities are: applying a quadratic phase taper distribution on the feed and applying a leaky wave substrate to create top hat patterns, allowing for higher efficiencies. These two

concepts can be explored because they have been shown to work for different designs across ±10% of fractional bandwidths as discussed in [36] and [37]. Finally the inclusion of thicker sidewalls can be incorporated. This can be useful since it can cut of surface wave modes when the cavity is to long in the longitudinal direction.

The leaky wave configuration A cavity and a slab are used to ensure a leaky wave configuration instead of free space above the array. The relative permittivity of the cavity and the slab, as well as the height of the cavity and the thickness of the slab (ϵ_c, ϵ_s, h_{cavity}, and h_{slab}), are optimization parameters that can be used to shape the pattern. Additionally, these parameters also affect the active input impedance of the array.

In terms of the analysis, this effectively changes both the TE and TM currents that need to be calculated to find the SGF above the slots, as well as the TE and TM currents in the far field. The different implementation for the SGF of the slot can be determined by calculating the input impedance above the slot, where $i_{TE/TM} = \frac{1}{Z_{in_{TE/TM}}}$. The currents in the far field can be found using the concept of a two-port network, with the ABCD matrix providing a convenient representation to find the far field TE and TM currents from the TE and TM currents at the input of the two-port network.

The inclusion of smaller sidewalls Surface waves and guided waves can pose significant challenges in connected arrays (CAs) for both active impedance and the profile of the equivalent currents on the slots. To ensure the absence of transverse magnetic (TM) surface waves, the original model incorporated sidewalls between each slot. However, TE surface waves can still propagate within the rectangular structure within the cavity. To suppress these transverse electric (TE) surface waves, the distance between the sidewalls, d'_y, must satisfy $d'_y < \frac{c}{2\sqrt{\epsilon_{br}} f_{max}}$. In terms of the Method of Moments (MoM), this adjustment involves modifying the d_y term in the Floquet sum for the spectral Green's function (SGF) below the slots.

B

Definition of Efficiency Terms

B.1 Criteria for Feed Design

Before conducting a comparative analysis, it is essential to define the efficiency terms considered to assess the performance. In this appendix, the performance criteria will be outlined and explained in detail. Additionally, the significance of each criterion will be discussed in relation to the overall design from a high-level perspective. Finally, we will explore the conceptual trade-offs between different criteria, providing insights into how these trade-offs can impact the overall design.

$\boldsymbol{\eta_{so}}$: Spillover efficiency refers to the proportion of the total electromagnetic field intensity that is effectively captured by the antenna.

This efficiency can be quantitatively defined using Equation (B.1). It is important to note that the current lens has been designed with a subtended angle θ_0 defined as $\theta_0 = \arctan[D/(2F)] = 37°$. This implies that the feed should ideally have a radiation pattern that does not extend beyond the angle θ_0.

$$\eta_{so} = \frac{\int_0^{2\pi}\int_0^{\theta_0} U_{\text{feed}}(\theta,\phi) sin(\theta)\, d\theta\, d\phi}{\int_0^{2\pi}\int_0^{\pi} U_{\text{feed}}(\theta,\phi) sin(\theta)\, d\theta\, d\phi} \tag{B.1}$$

$\boldsymbol{\eta_{ohmic}}$: The ohmic efficiency, of a lens quantifies the proportion of accepted power that is not lost due to resistive losses within the lens materials.

It is calculated by considering the power losses in both the dielectric material ($P_{\text{loss,diel}}$) and the metal components ($P_{\text{loss,metal}}$) relative to the total power accepted by the lens (P_{acc}). The ohmic efficiency is defined by equation (B.2).

$\boldsymbol{\eta_{feed}}$: The feed efficiency is quantified by the ratio of power radiated by the feed and the power at the input of the feed.

$$\eta_{\text{ohmic}} = 1 - \frac{P_{\text{loss,diel}} + P_{\text{loss,metal}}}{P_{\text{acc}} \cdot \eta_{so}} \tag{B.2}$$

$\boldsymbol{\eta_f}$: is the ratio of power radiated by the feed and the power at the input of the feed.

There can be many causes of feed inefficiency, all of which are grouped together into the feed efficiency, η_f. For this study, we are mainly interested in the feed inefficiency caused by the specific feeding

network used for the feeding antenna. The feed efficiency is defined by equation B.3

$$\eta_f = \frac{P_{rad}^{feed}}{P_{in}} \tag{B.3}$$

$\boldsymbol{\eta_t}$: the tapper efficiency is a measure of how much the reflector area is effectively used with respect to the physical area projected on the equivalent aperture

Taper efficiency is a versatile parameter that depends on the distribution of phase, amplitude, and polarization of the aperture field on the feed. The design implemented in [12] achieved a simulated aperture efficiency of over 90%. It is noteworthy that the objective of this work is not to improve the taper efficiency further, but to ensure a design that integrates well with the existing graded-index (GRIN) lens. For instance, the feed must be maintained at the phase center of the GRIN lens across the entire bandwidth.

The taper efficiency can be quantitatively described by equation B.4. In this equation, the electric field is the field calculated at the projected aperture, and because this is the case, measuring taper efficiency is usually done by measuring the maximum directivity of the lens. This can be done because there is an alternative definition for the taper efficiency given by equation B.5.

$$\eta_t = \frac{|\iint_A \vec{E}_a dA|^2}{A \iint_A |\vec{E}_a|^2 dA} \tag{B.4}$$

$$\eta_t = \frac{D}{D_{max}} \tag{B.5}$$

It is noteworthy that D in this function represents the measured directivity, while D_{max} is the maximum directivity possible for a given size, which is given by $D_{max} = \frac{4\pi A}{\lambda^2}$. Additionally, it is important to mention that the taper efficiency can be decomposed into two components: amplitude taper loss(ATL) and phase error loss(PEL). These components are given by equations B.6 and B.7.

$$ATL = \frac{(\iint_A |\vec{E}_a| dA)^2}{A \iint_A |\vec{E}_a|^2 dA} \tag{B.6}$$

$$PEL = \frac{|\iint_A \vec{E}_a dA|^2}{(\iint_A |\vec{E}_a| dA)^2} \tag{B.7}$$

C

Appendix C: Detailed design considerations for optimizing the spillover and impedance matching of the CTS feed

To derive the optimal parameters for the CTS-to-Printed Circuit Board (PCB) discontinuity, it is essential to develop a deeper understanding of all feed parameters, their constraints, and their influence on impedance matching as well as illumination quality. Additionally this appendix explains the implementation of an inductive feed element by means of introducing a sub wavelength discontinuity inside the feeding transmission line.

C.1 feed length(δ_f)

The length of the feed significantly affects the illumination quality: increasing the feed length leads to a more uniform excitation of the field inside the parallel plate waveguide (PPW) line. However, this comes at the cost of impedance matching, as a longer feed introduces a stronger capacitive coupling between the conductor on the dielectric and the PPW line.

C.2 feed width(w_f)

The width of the feed has a large influence on the illumination quality in particular in the H plane since the effective width of the feed depends a lot on the width of the slots. Again there is a trade-off from a matching perspective since the width cannot be larger then $\lambda_{sub}/2$ due to the fact that excites higher order modes inside the PPW lines of the CTS feed.

C.3 backing reflector distance(d_{br})

The reactance due to the backing reflector depends on two effects. First, there is a capacitive coupling between the conductor of the feeding transmission line. Second, a series inductance is induced by the PPW lines. Additionally, the distance of the backing reflector somewhat influences the real part of the impedance. This is because the conductor on the dielectric does not radiate fully upward, and therefore, the distance of the backing reflector also affects the illumination quality of the lens.

C.4 Cavity Height and Width (h_{cav}, w_{cav})

Both parameters do not significantly affect impedance matching or the illumination quality of the lens. However, several design considerations should be carefully addressed:

1. Both w_{cav} and h_{cav} should be smaller than $\lambda_{eff@60\text{GHz}}/2$ to ensure that higher-order modes are

not excited in the PPW lines of the CTS.

2. Both w_{cav} and h_{cav} should be selected to yield a reasonable line impedance.

C.5 height of the feeding network (z_{feed})

Changing the height of the feeding network introduces an inductive effect on the input impedance, particularly at high frequencies, due to the addition of a series PPW line.

C.6 Applying an Inductive Gap in the Feeding Network

Since the addition of an inductive gap in the feeding network plays a crucial role in optimizing impedance matching, the electromagnetic context of a step in transmission line width is considered following [28] (see Fig. C.1 for a visualization). The design approach is elaborated in detail here.

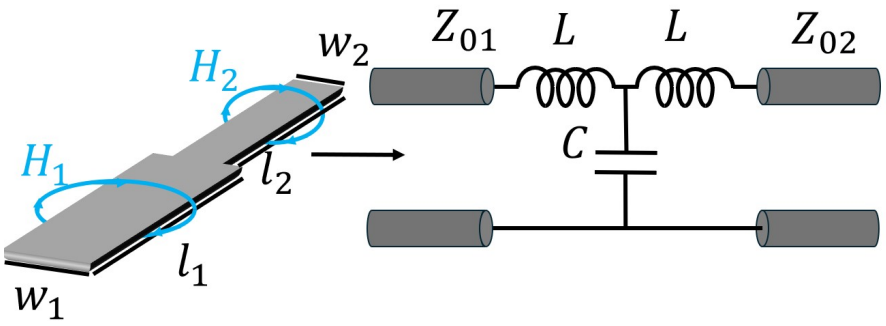

Figure C.1: Visualization of the equivalent field lines of two transmission lines with different widths.

To understand the behavior of a subwavelength discontinuity, one can in principle solve Maxwells equations at the discontinuity and apply modal analysis to fully characterize its response [38]. However, in practice a more convenient method is to perform parametric sweeps over the possible realizations of the discontinuitys length and width. The results of such a sweep are shown in Fig. C.2, and this procedure was used to design the discontinuity in the present work.

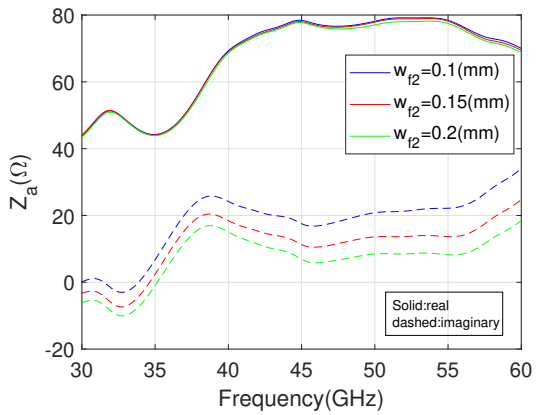

(a) Sweep over line width shows that a width of 100[μm] optimizes the active impedance

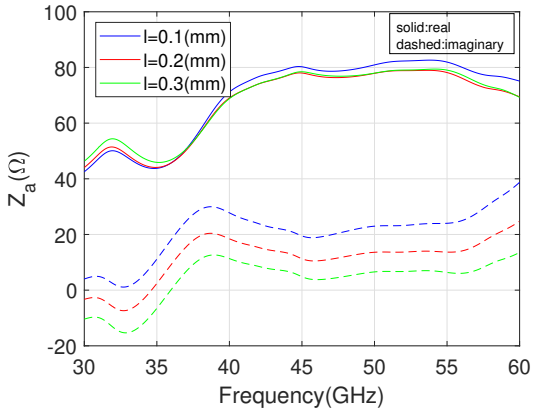

(b) Sweep over line length shows that a length of 100 or 200[μm] can both be used. However 200[μm] was chosen since it is less dependent on process variation.

Figure C.2: Impedance matching characteristics of the entire feeding network

D

Appendix D: Technical drawings of the CTS components

This appendix shows all technical drawings for the fabricated CTS feed.

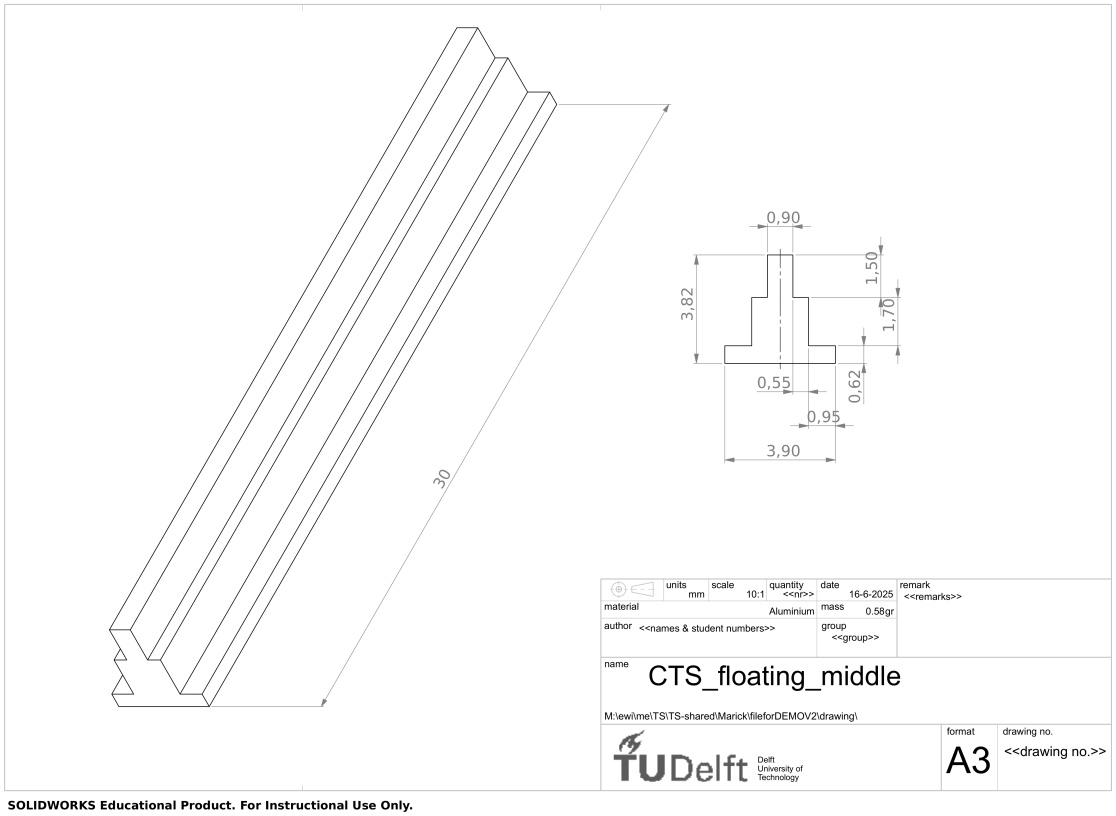

Figure D.1: Floating CTS middle piece

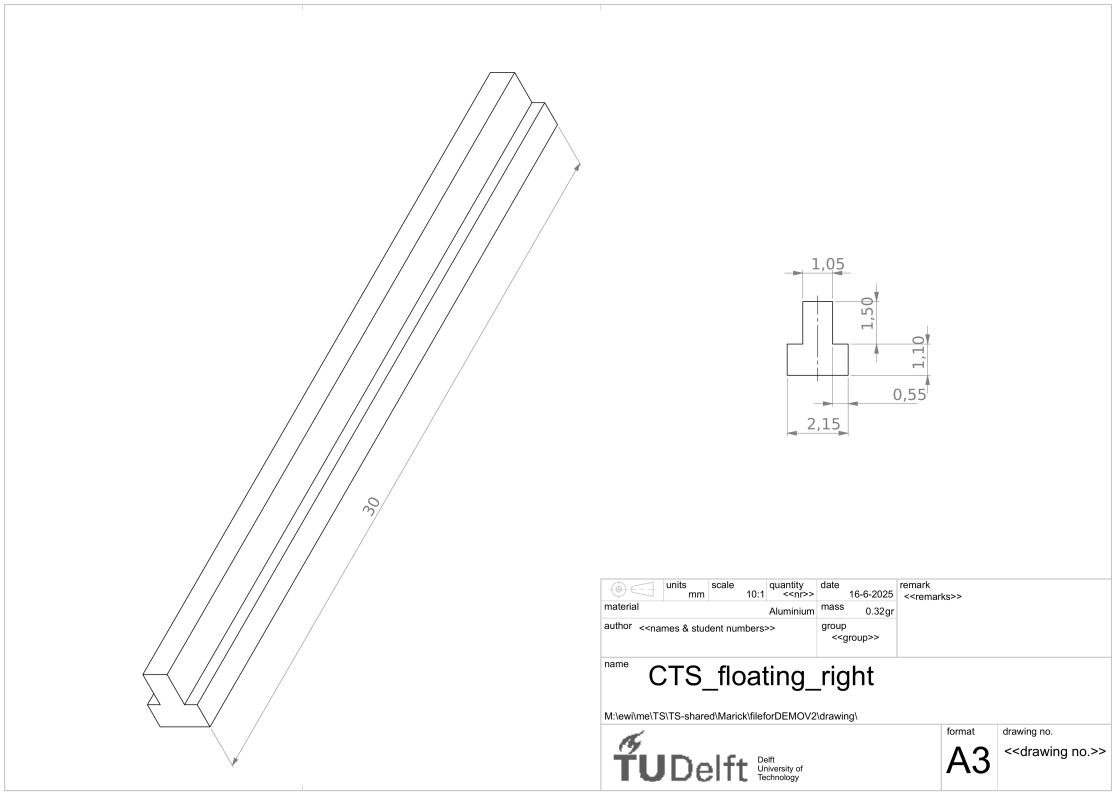

Figure D.2: Floating CTS right side

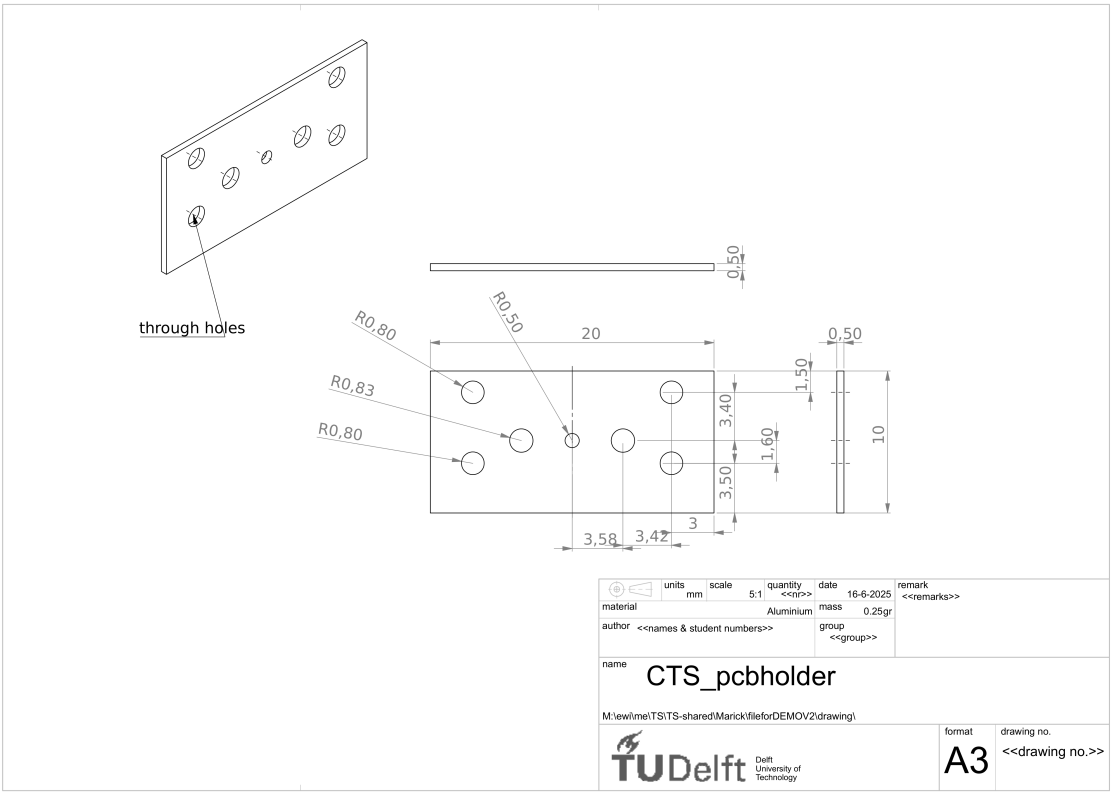

Figure D.3: CTS PCB holder

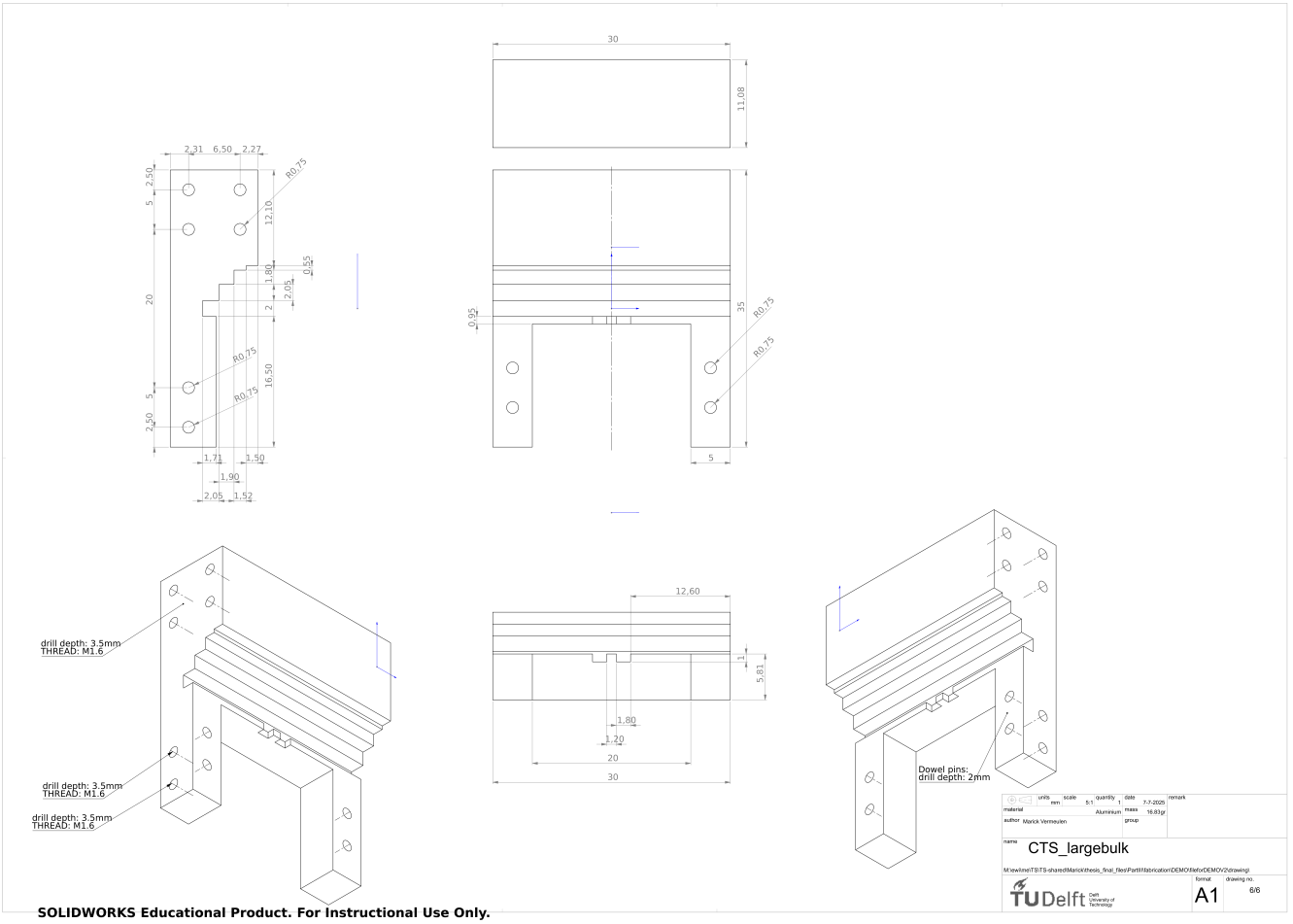

Figure D.4: CTS large bulk assembly

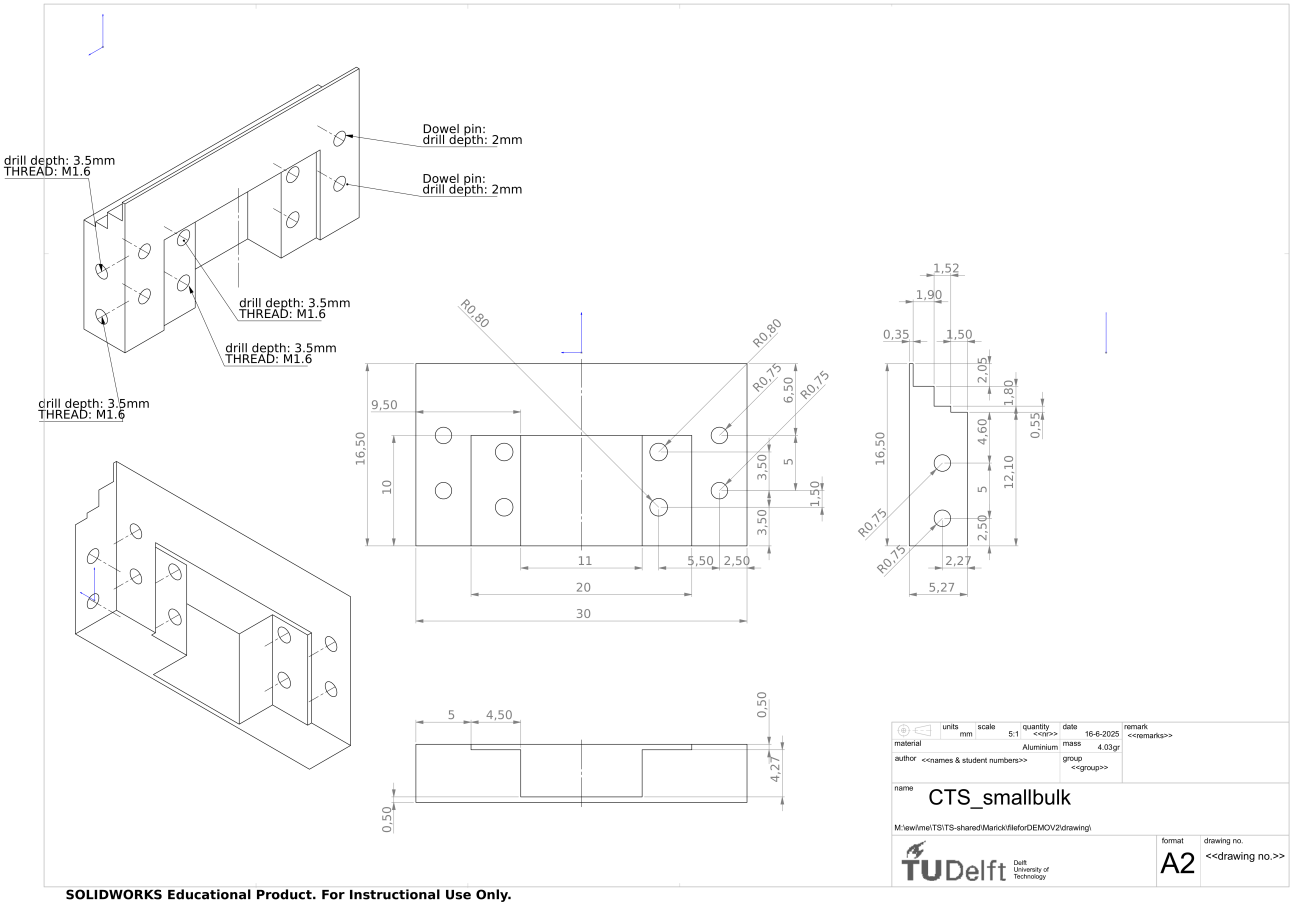

Figure D.5: CTS small bulk assembly

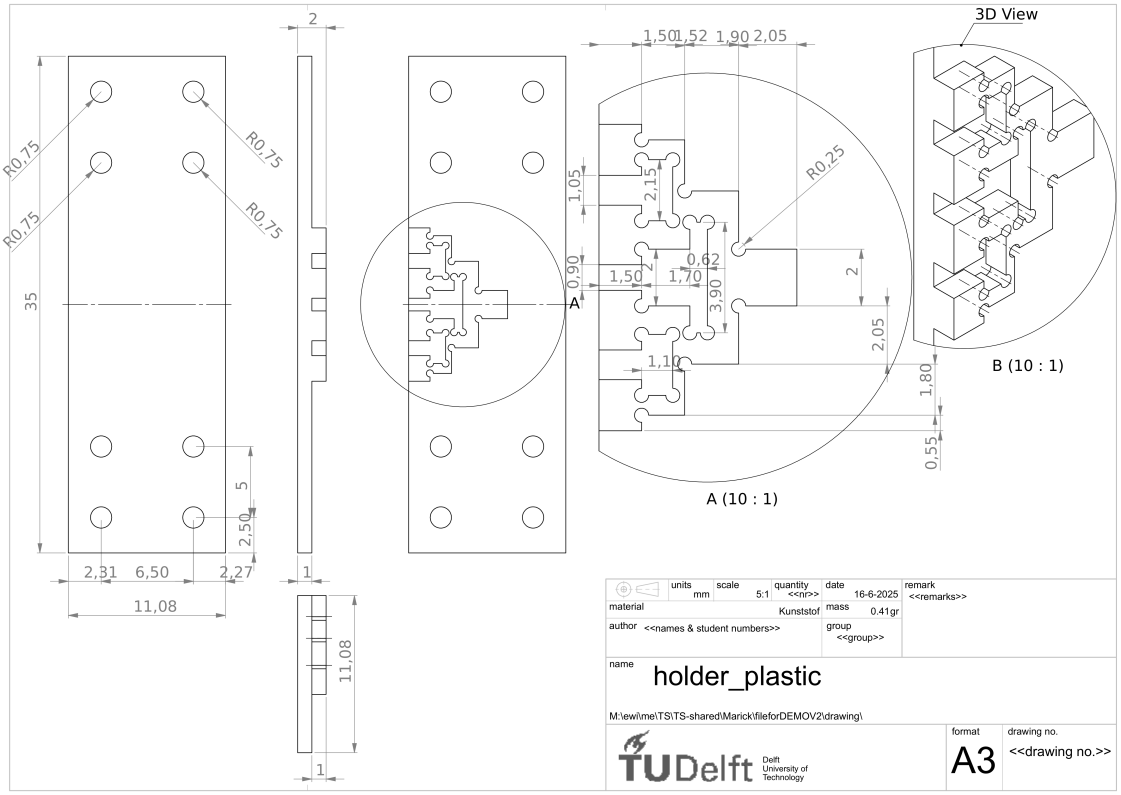

Figure D.6: Plastic holder design

E

Appendix E: De-embedding of a Two-/One-Port Network

The main objective during the de-embedding of a two-port network is to move the reference plane and calibrate out the Device Under Test (DUT) by using TRL (Thru-Reflect-Line) measurements and their corresponding T, R, and L matrices. This process is well illustrated in Figure E.1.

The de-embedding can be performed by calculating the inverse ABCD matrix of the DUT. This is achieved using equations E.1 through E.4. These equations can be derived by analyzing the relationship between the S-parameters of the DUT and the T, R, and L matrices, as described in [28].

It is important to note that the reflect measurement is not used directly in these equations; instead, it is employed to determine the sign of the square root in Equation E.1. Additionally, when converting from S-parameters to the ABCD matrix, it is crucial to account for different line impedances on both sides of the DUT, following the approach reported in frickey1992sparams.

The de-embedding of a one-port network follows a similar methodology, with the main difference being that the analysis targets obtaining the scalar de-embedded S_{11} from the S_{11} before moving the reference plane.

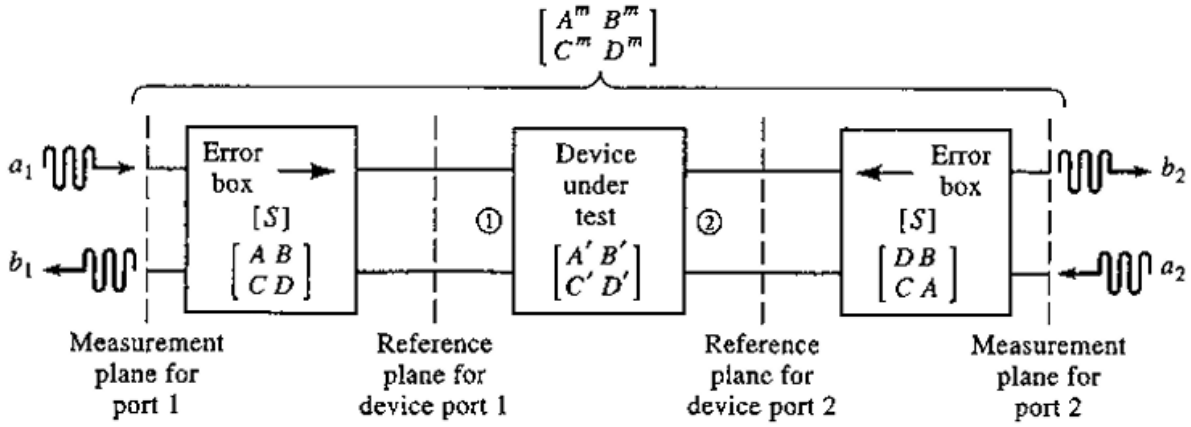

Figure E.1: De-embedding process from [28]

$$e^{\nu\ell} = \frac{L_{12}^2 + T_{12}^2 - (T_{11} - L_{11})^2 \pm \sqrt{\left[L_{12}^2 + T_{12}^2 - (T_{11} - L_{11})^2\right]^2 - 4L_{12}^2 T_{12}^2}}{2L_{12}T_{12}}, \tag{E.1}$$

$$S_{22} = \frac{T_{11} - L_{11}}{T_{12} - L_{12}e^{-\nu\ell}}, \tag{E.2}$$

$$S_{11} = T_{11} - S_{22}T_{12}, \tag{E.3}$$

$$S_{12} = S_{21} = \sqrt{T_{12}(1 - S_{22}^2)}. \tag{E.4}$$

References

[1] W. Hong, Z. H. Jiang, C. Yu, et al., "Multibeam antenna technologies for 5g wireless communications," IEEE Transactions on Antennas and Propagation, vol. 65, no. 12, pp. 6231–6249, Dec. 2017.

[2] Y. J. Guo, M. Ansari, R. W. Ziolkowski, and N. J. G. Fonseca, "Quasi-optical multi-beam antenna technologies for b5g and 6g mmwave and thz networks: A review," IEEE Open Journal of Antennas and Propagation, vol. 2, pp. 807–830, Jun. 2021.

[3] A. Jouade, M. Himdi, and O. Lafond, "Fresnel lens at millimeter-wave: Enhancement of efficiency and radiation frequency bandwidth," IEEE Transactions on Antennas and Propagation, vol. 65, no. 11, pp. 5776–5786, Nov. 2017.

[4] G. Liu, M. R. D. Kodnoeih, K. T. Pham, E. M. Cruz, D. González-Ovejero, and R. Sauleau, "A millimeter-wave multibeam transparent transmitarray antenna at Ka-band," IEEE Antennas and Wireless Propagation Letters, vol. 18, pp. 631–635, 2019.

[5] M. Jiang, Z. N. Chen, Y. Zhang, W. Hong, and X. Xuan, "Metamaterial-based thin planar lens antenna for spatial beamforming and multibeam massive MIMO," IEEE Transactions on Antennas and Propagation, vol. 65, no. 2, pp. 464–472, Feb. 2017.

[6] A. Paraskevopoulos, F. Maggiorelli, M. Albani, and S. Maci, "Radial GRIN lenses based on the solution of a regularized ray congruence equation," IEEE Transactions on Antennas and Propagation, vol. 70, no. 2, pp. 888–899, Feb. 2022.

[7] F. Maggiorelli, A. Paraskevopoulos, J. C. Vardaxoglou, M. Albani, and S. Maci, "Profile inversion and closed form formulation of compact GRIN lenses," IEEE Open Journal of Antennas and Propagation, vol. 2, pp. 315–325, 2021.

[8] N. C. Garcia and J. D. Chisum, "High-efficiency, wideband GRIN lenses with intrinsically matched unit cells," IEEE Transactions on Antennas and Propagation, vol. 68, no. 8, pp. 5965–5977, Aug. 2020.

[9] S. Jones and J. Brown, "Metallic delay lenses," Nature, vol. 163, no. 4139, pp. 324–325, Feb. 1949.

[10] M. Li and N. Behdad, "Wideband true-time-delay microwave lenses based on metallo-dielectric and all-dielectric lowpass frequency selective surfaces," IEEE Transactions on Antennas and Propagation, vol. 61, no. 8, pp. 4109–4119, Aug. 2013.

[11] C. M. Coco Martin and D. Cavallo, "Analysis and design of wideband artificial dielectric flat lenses," in Proceedings of the European Conference on Antennas and Propagation, Florence, Italy, Mar. 2023, pp. 1–5.

[12] W. Hu, "Artificial dielectric flat lenses: Analysis, design, simulations and measurements," M.S. thesis, Delft University of Technology, Delft, The Netherlands, 2023.

[13] C. M. Coco Martin, W. Hu, and D. Cavallo, "Design of wideband flat artificial dielectric lenses at mmwave frequencies," IEEE Transactions on Antennas and Propagation, vol. 72, no. 2, pp. 1418–1428, Feb. 2024.

[14] D. Cavallo and R. M. van Schelven, "Closed-form analysis of artificial dielectric layers with non-periodic characteristics," in Proceedings of the European Conference on Antennas and Propagation, Florence, Italy, Mar. 2023, pp. 1–5.

[15] P.-S. Kildal, "Factorization of the feed efficiency of paraboloids and Cassegrain antennas," IEEE Transactions on Antennas and Propagation, vol. AP-33, no. 8, pp. 903–908, Aug. 1985.

[16] S. Manshari, S. Koziel, and L. Leifsson, "A wideband corrugated ridged horn antenna with enhanced gain and stable phase center for X- and Ku-band applications," IEEE Antennas and Wireless Propagation Letters, vol. 18, no. 5, pp. 1031–1035, 2019.

[17] M. Abbas-Azimi, F. Mazlumi, and F. Behnia, "Design of broadband constant-beamwidth conical corrugated-horn antennas [antenna designers notebook]," IEEE Antennas and Propagation Magazine, vol. 51, no. 5, pp. 109–114, 2009.

[18] A. Pascual Laguna, D. Cavallo, J. J. A. Baselmans, and N. Llombart, "Focused connected array antenna as a broadband beam-steering feed for quasi-optical system," IEEE Transactions on Antennas and Propagation, vol. 70, no. 7, pp. 5995–6000, Jul. 2022.

[19] O. Yurduseven, D. Cavallo, and A. Neto, "Wideband dielectric lens antenna with stable radiation patterns fed by coherent array of connected leaky slots," IEEE Transactions on Antennas and Propagation, vol. 62, no. 4, pp. 1895–1902, Apr. 2014.

[20] M. Alonso-delPino, N. van Rooijen, S. Bosma, and N. Llombart, "A wideband corrugated leaky-wave feed with low cross-pol for high efficiency lens illumination," in 15th European Conference on Antennas and Propagation, Düsseldorf, Germany, Mar. 2021.

[21] M. Ettorre, F. Foglia Manzillo, M. Casaletti, R. Sauleau, L. Le Coq, and N. Capet, "Continuous transverse stub array for Ka-band applications," IEEE Transactions on Antennas and Propagation, vol. 63, no. 11, pp. 4792–4800, Nov. 2015.

[22] M. del Mastro, A. Mahmoud, T. Potelon, et al., "Ultra-low-profile continuous transverse stub array for satcom applications," IEEE Transactions on Antennas and Propagation, vol. 70, no. 6, pp. 4459–4471, Jun. 2022.

[23] A. J. van Katwijk, A. Neto, G. Toso, and D. Cavallo, "Efficient semi-analytical method for the analysis of large finite connected slot arrays," IEEE Transactions on Antennas and Propagation, vol. 71, no. 1, pp. 402–410, Jan. 2023.

[24] K. H. Yeap and C. Y. Tham, "Optimization of an offset receiver optics for radio telescopes," Journal of Infrared, Millimeter and Terahertz Waves, vol. 39, no. 8, 2018.

[25] W. H. Syed, D. Cavallo, H. Thippur Shivamurthy, and A. Neto, "Wideband, wide-scan planar array of connected slots loaded with artificial dielectric superstrates," IEEE Transactions on Antennas and Propagation, vol. 64, no. 2, pp. 543–553, Feb. 2016.

[26] C. M. Coco Martin, "Wideband flat lenses based on artificial dielectric layers," M.S. thesis, Delft University of Technology, Delft, The Netherlands, 2022.

[27] J. Baker-Jarvis, M. D. Janezic, J. H. G. Jr., and R. G. Geyer, "Transmission/reflection and short-circuit line methods for measuring permittivity and permeability," National Institute of Standards and Technology, Boulder, CO, USA, NIST Technical Note 1355, Dec. 1993. DOI: 10.6028/NIST.TN.1355. [Online]. Available: https://doi.org/10.6028/NIST.TN.1355.

[28] D. M. Pozar, Microwave Engineering, 4th. New York, USA: John Wiley & Sons, 2011.

[29] C. A. Balanis, Antenna Theory: Analysis and Design, 4th ed. Hoboken, NJ: Wiley, 2016.

[30] D. Sun, X. Chen, J.-Y. Deng, et al., "Gap waveguide with interdigital-pin bed of nails for high-frequency applications," IEEE Transactions on Microwave Theory and Techniques, vol. 67, no. 5, pp. 2640–2648, 2019. DOI: 10.1109/TMTT.2019.2908724. [Online]. Available: https://ieeexplore.ieee.org/document/8684682.

[31] X.-Y. Zhang, G.-B. Wu, Y.-X. Xie, G.-L. Huang, and S.-Y. Zhu, "A risley-prism-based achromatic beam-steering metalens antenna with wide bandwidth," IEEE Antennas and Wireless Propagation Letters, vol. 24, no. 6, pp. 1478–1482, 2025. DOI: 10.1109/LAWP.2025.3540795.

[32] R. M. van Schelven, D. Cavallo, and A. Neto, "Equivalent circuit models of finite slot antennas," IEEE Transactions on Antennas and Propagation, vol. 67, no. 7, pp. 4367–4376, Jul. 2019.

[33] D. Cavallo and A. Neto, "A connected array of slots supporting broadband leaky waves," IEEE Transactions on Antennas and Propagation, vol. 61, no. 4, pp. 1986–1994, Apr. 2013.

[34] D. Cavallo, "Connected array antennas: Analysis and design," PhD Thesis, Eindhoven University of Technology, Eindhoven, 2011.

[35] A. Neto and S. Maci, "Greens function for an infinite slot printed between two homogeneous dielectrics. part i: Magnetic currents," IEEE Transactions on Antennas and Propagation, vol. 51, no. 7, pp. 1572–1581, Jul. 2003.

[36] A. Neto, N. Llombart, G. Gerini, M. Bonnedal, and P. D. Maagt, "EBG enhanced feeds for the improvement of the aperture efficiency of reflector antennas," IEEE Transactions on Antennas and Propagation, vol. 55, no. 8, pp. 2185–2193, Aug. 2007.

[37] R. M. van Schelven, W. H. Syed, G. Carluccio, et al., "Phased array with pattern shaping and scan loss reduction for millimeter waves," IEEE Transactions on Antennas and Propagation, vol. 71, no. 1, pp. 159–168, Jan. 2023.

[38] N. Marcuvitz, Ed., Waveguide Handbook (MIT Radiation Laboratory Series). New York: McGraw-Hill, 1948, vol. 10.